COMPUTATIONAL MODELING OF A MICRO-SWIMMER: FLUID-STRUCTURE INTERACTION

QUEK YEONG LOONG RAYMOND
(B.Eng (Hons.), NTU)

A THESIS SUBMITTED

FOR THE DEGREE OF DOCTOR OF PHILOSOPHY
DEPARTMENT OF MECHANICAL ENGINEERING
NATIONAL UNIVERSITY OF SINGAPORE

2015

DECLARATION

I hereby declare that the thesis is my original work and it has been written by me in its entirety. I have duly acknowledged all the sources of information which have been used in the thesis.

This thesis has also not been submitted for any degree in any university previously.

Quek Yeong Loong Raymond
23 July 2015

Acknowledgements

I would like to express my sincere appreciation to my research advisors, Associate Professor Lim Kian Meng and Dr Le Duc Vinh.

Associate Professor Lim has generously spent countless hours sharing his knowledge with me during our weekly meetings.

Dr Le has graciously taught me the implementation of the immersed boundary method.

I would also like to thank our collaborator Dr Chiam Keng Hwee for his valuable insights into our cilia problem.

In addition, I would like to thank fellow Ph.D. student Ahmad Ali Tahmasebi Moradi for his valuable input during our regular discussions.

Finally, I would like to thank the Agency for Science, Technology and Research (A*STAR) for supporting my studies under the Scientific Staff Development Award (SSDA) program.

Abstract

Fluid propulsion on the micro-scale is often accomplished through the presence of actively beating cilia. It is well-known that cilia arranged in arrays can spontaneously coordinate their beat patterns to form metachronal waves; however, while it is generally agreed upon that metachronal waves arise largely due to hydrodynamic interactions, their effects on fluid propulsion are still not thoroughly explored. There are at present complex, non-linear models where cilia motion is modelled as a function of their internal biological mechanisms; however these models are often computationally challenging and expensive to perform.

We therefore present a simplified computational model of a cilia array that has the ability to spontaneously produce metachronal waves. Our cilia array mimics the cilia on multi-ciliated micro-swimmers such as *Paramecium* and *Opalina*, or multi-flagellated micro-swimmers such as *Volvox*. Our model is based on the immersed boundary method. Each individual cilium is modelled as a 1-dimensional elastic structure immersed in a Newtonian fluid. Model variables such as fluid velocities, pressure and cilia positions are solved using parallel computing methods. Our computational model enables us to study various aspects of spontaneously occurring metachronal waves. We are able to systematically study the effects of cilia number density and stiffness on metachronal wave patterns. We are also able to study fluid transport along the cilia array. We show the existence of an optimal cilia number density giving rise to maximum fluid velocity at the cilia tips.

After establishment of our basic cilia model, we progress to a stratified two-fluid configuration. Such a configuration corresponds to physiological conditions similar to that on our respiratory epithelium, where the cilia reside in a periciliary layer (PCL) below a mucus layer. Our model treats the mucus as a highly viscous Newtonian fluid. Our model shows that the presence of a second fluid layer has the ability to affect metachronal wave propagation and

fluid velocity profiles along the cilia array. Most notably, our model shows that the presence of surface tension between the PCL and mucus layer drastically modifies the vortices produced by cilia motion.

Thesis advisors:

Associate Professor Lim Kian Meng, NUS, Department of Mechanical Engineering, Singapore

Dr Le Duc Vinh, Institute of High Performance Computing, A*STAR, Singapore

Table of contents

List of Figures

Validation of the centerline velocity along $\vec{X} = \vec{X}(0.5, 0.5, z)$ is shown. We obtain good agreement with simulation results from Sahin [119] and Jiang et al [120]. A 80^3 grid is used in our simulation.

4.2 **(**a) The final steady deformation of the simulated cantilever beams are shown. As the number of points M making up the cantilever beam is increased, the solution approaches the analytical Euler-Bernoulli solution. (b) The percentage error in tip deflection is shown. As the number control points M is increased, the error is reduced. At $M = 39$, the error is 2%. 78

4.3 (a) Our benchmark case consists of an array of 21×21 cilia. The cilia are angled at $45°$ to the substrate and tip loadings are imposed. Each cilium is spaced a distance of L in the $x-$direction and a distance of $0.5L$ in the $y-$direction. The chamber height is $1.5L$. Boundary conditions for the fluid are $\vec{u} = 0$ and $\vec{\nabla} p \cdot \vec{n} = 0$ for the substrate and chamber ceiling, and $\vec{\nabla}(\vec{u} \cdot \vec{n}) = 0$ and $p = 0$ for the surrounding side faces. In this figure, $Sp = 3$. (b) The oscillations of the cilia at $(0,0)$ for the case of $Sp = 3$ is shown. The cilium exhibits deformations large enough such that the cilia tip contacts the substrate. (c) The oscillations of the cilium at $(0,0)$ for the case of $Sp = 5$ are shown. Compared to the case where $Sp = 3$, the oscillations here are of smaller amplitude. The ciliuim shapes in (b) and (c) are similar to that obtained by Alexeev et al. [44]. 81

4.4 Fluid flow rates obtained in our simulations are shown. Our model is able to produce similar flow magnitudes and flow reversals as obtained by Alexeev et al. [44]. 82

4.5 (a) The problem of a lid-driven cavity with a single vertical beam is used to test the efficiency of our code. (b) Results of a speed-up test for our code is shown. 84

5.1 (a) The regular arrangement of basal bodies on *Paramecium* is shown. Image is reproduced from [121]. (b) The irregular arrangement of mouse oviduct cilia is shown. Image is reproduced from [122]. 86

5.2 (a) We use the immersed boundary method to simulate an array of 21 by 21 cilia. (b) By tracking the cilia tip heights above the substrate, we obtain contour plots indicating cilia beat motion. The colorbar indicates the heights of cilia tips above the substrate. Since cilia tips are higher during the forward stroke and are lower during the reverse stroke, light 88

contours therefore represent cilia in the forward stroke while dark contours represent cilia in the reverse stroke. (c) By extracting a cross section at $y = 0$ at each time, we are able to obtain a kymograph. (d) By performing fast Fourier transforms (FFTs) on the kymographs, we obtain the wave numbers and frequencies of the metachronal waves. (e) The dominant frequencies in our simulations can then be extracted. This dominant frequency corresponds to the red triangle in (d). Consequently, dominant wave numbers can also be obtained.

5.3 This figure shows contours of metachronal waves passing over a 3×3 array where the cilia has been perturbed by reversal of the cilia beat stroke. A chosen wave front (solid black line) is marked and tracked. The wave front forms (a) and travels to the perturbed region (b), The wave front breaks over the perturbed region in (c) and (d), then reforms after it in (e). The wave front then travels to the edge of the array (f). 90

5.4 This figure shows contours of metachronal waves passing over a 21×3 array where the cilia has been perturbed by reversal of the cilia beat stroke. A chosen wave front (solid black line) is marked. The wave front forms (a) and travels to the perturbed region (b). The wave front vanishes at the edge of the perturbed region (c). Another wave front is formed after the perturbed region (d), and travels to the edge of the array (e), (f). There is no evidence the wave front after the perturbed region in (d)-(f) is associated with the wave front before the perturbed region in (a)-(b). 91

5.5 This figure shows contours of metachronal waves passing over an 21×7 array where cilia stroke has been perturbed by having the cilia beat stroke reversed. The perturbed region is now large enough to form its own metachronal waves. Two chosen wave fronts (solid black and blue lines) are marked. The black line represents a wave front in the unperturbed region while the blue line represents a wave front in the perturbed region. The wave fronts form in (a), (b) and (c). The wave front marked in black travels rightward while the wave front marked in blue travels leftward. Both wave fronts vanish at the boundary between the perturbed and unperturbed regions. New wave fronts are formed after the perturbed regions in (d). The new wave front marked in blue travels leftward while the new wave front marked in black travels rightward in (e)-(f). 92

5.6 This figure shows kymographs taken at the cross section $y = 0$. (a) Kymograph of a 3×3 cilia array subjected to perturbation is shown. Wave fronts across the perturbed region are not continuous. (b) Kymograph of a 21×3 cilia 93

array subjected to perturbation is shown. Wave fronts across the perturbed region are observed to be continuous. (c) Kymograph of a 21×7 cilia array subjected to perturbation is shown. In this case, the perturbed region is large enough such that it can form its own metachronal waves. Wave fronts across the perturbed region are observed to be only somewhat continuous.

5.7 This figure shows the paths of passive tracer particles over perturbed regions of the cilia array. The particles are seeded at a height of $1.07L$ above the substrate. (a) In the case where no cilia is perturbed, the particles flow smoothly over the cilia array. (b) In the case where the perturbed region is a small 3×3 array, particles flow around the perturbed region. (c) In the case where the perturbed region is an 21×3 array, particles flow over the perturbed region. (d) In the case where the perturbed region is an 21×7 array, a vortex is formed above the perturbed region. Some particles flow over the perturbed region while others are entrained within the vortex. 96

5.8 This figure shows the progression of a wave front on a cilia substrate subjected to cyclic stretching. A representative wave front is indicated by the solid black line. The cyclic stretching takes place in the direction parallel to the forward stroke. The natural frequency of the cilia is $\hat{f}_0 = 47.2Hz$ while the cyclic stretching frequency is $\hat{f}_{substrate} = 35Hz$. The stretching strain is $\varepsilon = 0.06$. One cycle of the imposed cyclic stretching is shown. 98

5.9 Spectra amplitudes at varying magnitudes of stretching strain ε are shown. In (a), a cyclic stretching frequency of $\hat{f}_{substrate} = 35Hz$ is imposed, while in (b), a cyclic stretching frequency of $\hat{f}_{substrate} = 40.2Hz$ is imposed. In both cases, the dominant frequency at low stretching strains is $\hat{f} / \hat{f}_0 = 1$, which corresponds to the natural frequency of the beating cilia. At high stretching strains where $\varepsilon > 0.1$, the dominant frequencies correspond to the cyclic stretching frequencies of $\hat{f} / \hat{f}_0 = 0.74$ in the case of (a) and $\hat{f} / \hat{f}_0 = 0.85$ in the case of (b), i.e. $\hat{f} / \hat{f}_{substrate} = 1$ in both cases. 99

5.10 This figure shows the effect of α on metachronal waves. As α is increased through (a) $\alpha = 0$, (b) $\alpha = 1$, (c) $\alpha = 2$ and (d) $\alpha = 4$, metachronal waves form and become robust. 101

5.11 The kymograph of a case where $\beta = 0$ is imposed at $t = 0.15s$ is shown. It is observed that when $\beta = 0$, the metachronal wave fronts are disrupted. 101

5.12 (a) This figure shows an irregular cilia array. The cilia are located at vertices of an unstructured mesh generated by a Delaunay triangulation algorithm. The mesh is shown on the substrate. (b) The kymograph from the unstructured cilia array is shown. Despite the unstructured arrangement of cilia, metachronal waves are observed. 103

5.13 (a) A schematic of a two-fluid configuration is shown. The fluids are separated by a horizontal interface colour-coded by interface height above the substrate. H_Ω is the height of the channel. We isolate a square column in the center of our cilia array. The fluxes through the walls of the centre column are used to calculate the average bulk flow velocities, and the cross-sectional area of the column at the height of cilia tips (grey square of side Δl) is used to calculate average slip velocities. (b) Velocity contours of (i) $\vec{u}\cdot\vec{n}_{x^-}$ and (ii) $\vec{u}\cdot\vec{n}_{x^+}$ are shown. The contours are similar, indicating that flow profiles through the faces denoted x^- and x^+ are highly similar. Likewise, velocity contours of (iii) $\vec{u}\cdot\vec{n}_{y^-}$ and (iv) $\vec{u}\cdot\vec{n}_{y^+}$ are highly similar. 105

6.1 **(**a) Variation of metachronal wave frequency $\hat{f}$ with cilia bending stiffness EI is shown. (b) Variation of metachronal wave vector magnitude $|k|$ with cilia bending stiffness EI is shown. 110

6.2 This figure shows variations of cilia tip heights in time for the following scenarios: (a) $EI = 6.90\times10^{-21}\,Nm^2$ and $d^{-2} = 4.06\times10^{9}\,m^{-2}$, (b) $EI = 8.27\times10^{-19}\,Nm^2$ and $d^{-2} = 4.06\times10^{9}\,m^{-2}$, (c) $EI = 1.38\times10^{-18}\,Nm^2$ and $d^{-2} = 2.60\times10^{9}\,m^{-2}$ and (d) $EI = 6.90\times10^{-21}\,Nm^2$ and $d^{-2} = 1.15\times10^{9}\,m^{-2}$. (a), (b), (c) and (d) are correspondingly marked as (i), (ii). (iii) and (iv) in Figures 6.1(a) and (b). In all four scenarios, slices at mid plane $y = 0$ are shown. 111

6.3 (a) Profile of $\langle u \rangle$, the component of velocity in the forward stroke as defined in equation 6.1, for different cilia stiffness at fixed number density $d^{-2} = 2.60\times10^{9}\,m^{-2}$**.** (b) Slip velocity at cilia tip, as defined in equation 6.2, vs. cilia number density for various EI. 115

6.4 (a) A vector plot of the averaged fluid velocity field from our simulation is shown. (b) The velocity displacement field of the fluid generated by cilia undergoing symplectic metachrony is shown. (b) is reproduced from Ding et al. 118

In cases where two fluids are present, the fluid interface is indicated by a horizontal dashed line.

7.6 A schematic of the interaction between the fluid and cilia is shown. Metachronal wave fronts are formed by rows of cilia alternating between forward and reverse strokes (horizontal gray arrows). The metachronal wave front interfaces are indicated by vertical gray dotted lines. As cilia movement push fluid toward or away from the interfaces, opposing vortex pairs are set up in the fluid. Vortex directions are indicated counter-clockwise (ccw) or clockwise (cw). 136

7.7 This figure shows particle trajectories seeded at various heights for (a) $\sigma = 0 Nm^{-1}$ and $\mu_2 / \mu_1 = 1$, (b) $\sigma = 0.01 Nm^{-1}$ and $\mu_2 / \mu_1 = 1$, (c) $\sigma = 0 Nm^{-1}$ and $\mu_2 / \mu_1 = 6$, and (d) $\sigma = 0.01 Nm^{-1}$ and $\mu_2 / \mu_1 = 6$. The particle traces for all cases are shown up to $t = 0.3s$. 137

7.8 The interface deformation is shown in the cases of (a) $\sigma = 0 Nm^{-1}$ and $\mu_2 / \mu_1 = 1$, (b) $\sigma = 0.01 Nm^{-1}$ and $\mu_2 / \mu_1 = 1$, (c) $\sigma = 0 Nm^{-1}$ and $\mu_2 / \mu_1 = 6$, and (d) $\sigma = 0.01 Nm^{-1}$ and $\mu_2 / \mu_1 = 6$. Significant interface deformation is observed for all cases of μ_2 / μ_1 where $\sigma = 0 Nm^{-1}$ while negligible interface deformation is observed for all cases of μ_2 / μ_1 where $\sigma = 0.01 Nm^{-1}$. In all cases the interface deformations are shown at $t = 0.3s$. 138

7.9 This figure shows the root mean square (RMS) interface heights of the interface between the upper and lower fluids at $t = 0.3s$. 139

7.10 This figure shows a phase space diagram depicting our simulated findings. We note a region of enhanced mixing, a region of enhanced transport, and a region where no significant enhancement to either mixing or transport was observed. The blue contours are contours of $\left(\text{RMS Interface Height}\right)/L$ while the red contours are contours of $U_{||} / U_{||0}$. 140

List of Tables

Nomenclature

PCL	Periciliary layer
IBM	Immersed boundary method
L	Cilia length
EI	Cilia bending stiffness
T_θ	Torsion spring constant
k	Cilia stretching stiffness
E_0	Total energy expanded by cilia per stroke
E	Energy expanded by cilia
P_0	Active force magnitude per unit area acting on cilium
f_0	Active force magnitude per unit length acting on cilium
d	Distance between cilia
d^{-2}	Cilia number density
ρ_1	Density of lower fluid
ρ_2	Density of upper fluid
μ_1	Dynamic viscosity of lower fluid
μ_2	Dynamic viscosity of upper fluid
υ_1	Kinematic viscosity of lower fluid
υ_2	Kinematic viscosity of upper fluid
σ	Surface tension at fluid interface
L_Ω	Chamber length
W_Ω	Chamber width
H_Ω	Chamber height
N_c	Number of cilium control points
t	Time
Δt	Time step size
s	Lagrangian coordinate along cilium
Δs	Spacing between control points on cilium
Δs_0	Rest spacing between control points on cilium
h	Fluid grid size
ε_0	Parameter specifying level set interface thickness
$\vec{F}$	Body force acted on fluid by cilium control points
$\vec{F}_\sigma$	Body force acted on fluid by surface tension
$\vec{f}$	Point force acted on fluid by cilium control points
$\vec{u}$	Fluid velocity
u	Fluid velocity in $x-$direction
v	Fluid velocity in $y-$direction

w	Fluid velocity in $z-$direction
$\vec{u}^*$	Intermediate fluid velocity
$\vec{X}$	Coordinate of cilium
p	Pressure
φ	Pressure correction
Φ	Level set function
$\vec{f}_{active}$	Active force on cilium control point
$\vec{f}_{elastic}$	Elastic force on cilium control point
$\vec{f}_{moment}$	Moment force on cilium control point
$\vec{M}$	Moment on cilium control point
$\vec{\theta}$	Angle between adjacent cilium control points
$\vec{\theta}_0$	Rest angle between adjacent cilium control points
$\vec{f}_{forward}$	Forces exerted on cilium control point during forward stroke
$\vec{f}_{reverse}$	Forces exerted on cilium control point during reverse stroke
α	Magnitude of active force component imposed to enforce planar beating during cilia forward stroke
β	Magnitude of active force component imposed to enforce sideways sweep during cilia reverse stroke
$\hat{f}$	Frequency of cilia beat
$\hat{f}_0$	Frequency of cilia beat without stretching perturbations
$\hat{f}_{substrate}$	Frequency of substrate stretching
A_c	Amplitude of substrate stretching
L_c	Length of cilia bed
ε	Strain of substrate stretching
λ	Metachronal wavelength
N_λ	Number of cilia rows per metachronal wave
L_c	Length of cilia bed
γ	Parameter determining advective or convective behavior of tracers
$U_{\parallel}$	Cross sectional fluid velocity parallel to cilia forward stroke
$U_{\perp}$	Cross sectional fluid velocity perpendicular to cilia forward stroke
$U_{slip\parallel}$	Fluid slip velocity parallel to cilia forward stroke
$U_{slip\perp}$	Fluid slip velocity perpendicular to cilia forward stroke

1 Introduction

1.1 A brief description of cilia and flagella

The cilium is an important and common sub-cellular organelle found in nature. It is found on most cells in our bodies [1] and is known to serve a variety of functions. For example, primary cilia are known to be responsible for trafficking of materials between the inner and outer segments of rod cells. Failure of cilia to perform this function leads to retinal degeneration [2]. Primary cilia are also used to sense signals in cerebrospinal fluid, a process important for neurogenesis [3].

Primary cilia are mostly immotile and incapable of fluid propulsion. However, there too exist active, motile cilia capable of fluid propulsion. In terms of outward appearances, motile cilia are similar to immotile primary cilia. They both are long, narrow, whip-like biological structures. But unlike immotile primary cilia, motile cilia possess an internal active mechanism. This mechanism consists of dynein motors powered by adenosine triphosphate (ATP) [4]. This mechanism enables motile cilia to be capable of spontaneous movement and is thus able to propel surrounding fluid.

Another organelle similar to the motile cilium is the flagellum. Motile cilia and flagella, although known by different names, are essentially structurally identical. Their difference comes mainly from the function they serve. Cilia commonly refer to the dense, beating bundles attached to stationary surfaces immersed in fluid (e.g. ciliated epithelial cells), while flagella commonly refer to attachments on free-swimming micro-organisms used for propulsion.

An example of cilia can be seen in our respiratory system. Here, the cilia are responsible for transportation of mucus, in essence forming part of an integral cleansing mechanism. Cilia are also known to play important roles in other organs in the human body. Breuning et al. [5] described how cilia serve to

maintain homeostasis in the brain. Neural precursor cilia have also been shown by Breuning et al. [6] to regulate sonic hedgehog homolog (Shh) signaling.

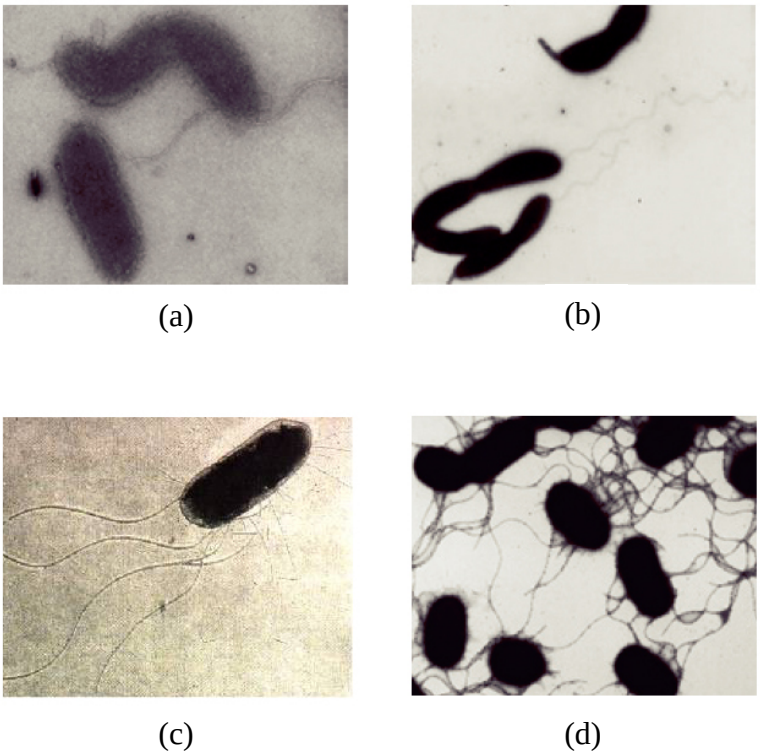

(a) (b)

(c) (d)

Figure 1.1 Images of *Idiomarina loihiensis* (a) and *Caulobacter crescentus* (b) are shown. These microorganisms are examples of monotrichous bacteria. Images of *Escherichia coli* (c) and *Salmonella enterica servovar* Typhimurium (d) are shown. These microorganisms are examples of peritrichous bacteria. Images (a), (b) and (d) are reproduced from Chevance and Hughes [8]. Image (c) is reproduced from Carnegie Mellon University Department of Biological Sciences, February 2015.

An example of hydrodynamic interactions with cilia formation in the brain was described by Guirao et al. [7]. The authors studied the effect of cerebral-spinal fluid flow on the orientation of cilia on ependymal cells. Ependymal cells are cells forming the epithelial membrane lining the ventricular system in the brain and spinal cord. Ependymal cells start by clustering basal bodies on the apical surface. Bundles of cilia would later grow out of the basal bodies. The cilia from such cells on the apical surface are arranged in a specific pattern and beat in coordination. Experiments performed by the authors with mice showed that primary cilia on radial glia cells first set up an initial flow. It

is with this flow that the ependymal cells are able to later dock, orientate and coordinate their own beating cilia.

As stated earlier, flagella are commonly used in the propulsion of micro-organisms. An example of flagella can be seen in spermatozoa. Here, the single flagellum attached to each spermatozoon is responsible for propelling the spermatozoon in the direction of the egg. Examples of flagella are also abundant in bacteria [8]. Examples of monotrichous bacteria include *Idiomarina loihiensis* (Figure 1.1(a)) and *Caulobacter crescentus* (Figure 1.1(b)), while examples of peritrichous bacteria include *Escherichia coli* (Figure 1.1(c)) and *Salmonella enterica servovar* Typhimurium (Figure 1.1(d)).

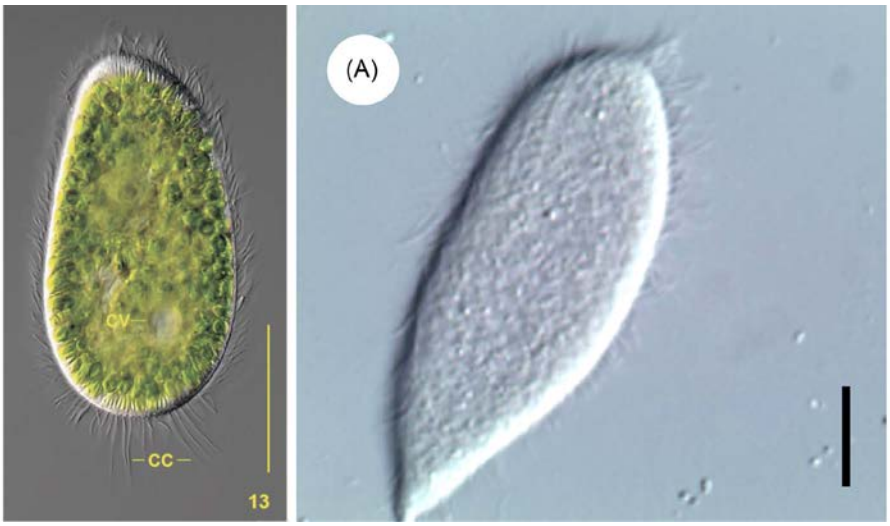

(a) (b)

Figure 1.2 Images of *Paramecium* (a) and *Opalina* (b) are shown. Both microorganisms are examples of microorganisms with cilia. Image (a) is reproduced from Yano et al. [9]. Image (b) is reproduced from Li et al.[10].

It must be noted that the distinction between motile cilia and flagella as stated above is only arbitrary. One example where cilia are used for propulsion can be seen with *Paramecium* (Figure 1.2(a)). A paramecium is a micro-organism about 200μm in length. The paramecium body is covered with cilia. The cilia then engage in coordinated, collective beating, allowing the paramecium to

swim in its desired direction. Another microorganism similar to *Paramecium* is *Opalina* [11] (Figure 1.2(b)).

Also, a distinction must be made with regards to the different kinds flagella, namely the flagella found on eukaryotic cells and the flagella found on bacteria. Eukaryotic flagella have an actively beating axoneme as its internal structure, while bacterial flagella are passive, corkscrew-shaped structures rotated by a motor at its base [12]. An excellent and recent discussion on these mechanisms is presented in [8].

Since motile cilia and flagella are structurally similar and serve biologically similar functions, we shall discuss them both in this work. As will be shown in Chapter 2, the numerical methods used to model cilia and flagella can also be highly similar. Subsequent chapters will focus solely on the motile cilia and its role in metachronal wave generation and fluid propulsion in the context of *Paramecium* or *Opalina* as a micro-swimmer.

1.2 Research motivation

A fascinating feature exhibited by cilia is the formation of metachronal waves. Metachronal waves are formed when successive cilia beat with a slight phase difference due to hydrodynamic interactions. The waves are symplectic if they travel in the same direction as the forward cilia stroke, and antiplectic if they travel in the direction of reverse cilia stroke. Both symplectic and antiplectic waves are found in nature. Metachronal waves are symplectic for *Opalina* and antiplectic for *Paramecium*.

While it is generally agreed upon that metachronal waves arise largely due to hydrodynamic interactions, their effects on fluid propulsion are still not thoroughly explored. At present, most numerical models of cilia impose metachronal waves by prescribing the displacements of the cilia. Such models allow the study of various flow quantities (e.g. cilia pumping efficiencies or

flow features) as a function of metachronal wave direction, wavelength or frequency.

However, there are increasingly more complex, non-linear models where cilia motion is a function of their internal biological mechanisms. Here, metachronal waves are spontaneously generated through coupling between the internal biological mechanisms and the surrounding fluid. Some of these models require simplification of the cilia into discrete point forces, while others represent the cilia realistically as long, narrow structures. These models do not allow direct control over the metachronal wave formation, direction, wavelength or frequency; however, they do offer the ability to study the effects of other physical parameters (e.g. fluid viscosities, cilia stiffness and spacing) on the metachronal waves themselves.

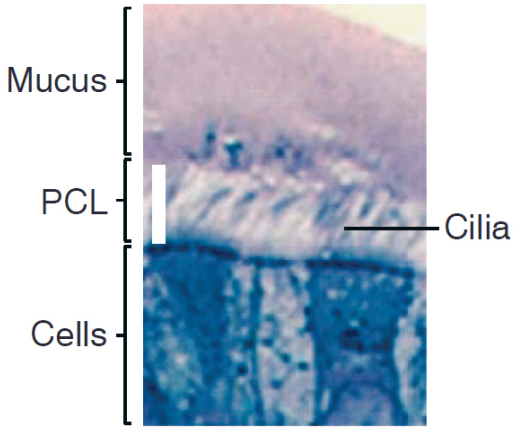

Figure 1.3 Light microscopy image of cilia immersed in a periciliary layer (PCL) is shown. A mucus layer sits atop the PCL. Image is reproduced from [13].

Computational models where cilia are realistically represented are often challenging to solve. In 3D simulations of cilia, though the internal biological mechanisms responsible for metachronal wave generation are often simplified, the computational costs are still considerable. As will be seen in Chapter 2, a number of these models require a fluid grid dense enough to resolve the internal mechanisms of the cilium. This results in a computationally expensive problem.

We therefore present a simplified 3D cilia model where the internal biological mechanisms of the cilia need not be resolved by the fluid grid. Our model therefore allows a coarse fluid grid to be used, hence reducing computational costs. Our model can then be used to study the various aspects of metachronal wave generation and the propulsion of cilia on their surrounding fluid.

In addition, there is to-date very few models that attempt to model the cilia in our respiratory system with realistic parameters. In the respiratory system, the cilia resides in a layer of Newtonian fluid called the periciliary layer (PCL). A layer of mucus sits atop the PCL [13], as shown in Figure 1.3. The challenge here is in modeling this two-fluid configuration. Once our basic cilia model is established, progression to this configuration is naturally in order. We shall therefore attempt to adapt our model to this two-fluid configuration, albeit with the major simplification that the mucus is treated as a Newtonian fluid.

1.3 Research objectives

The objectives of this research work are therefore as follows.

1. **Develop a simplified model of cilia.**
   We aim to use a simple rod-and-spring model to model the cilia. As our model is highly simplified, we must take great care to ensure our model is still reasonably realistic. Our model is presented in Chapter 3 and various benchmarks of our model is presented in Chapter 4.

2. **Investigate formation, robustness and effects of metachronal waves on a cilia bed.** This arrangement mimics the cilia on multi-ciliated micro-swimmers such as *Paramecium* and *Opalina*, or multi-flagellated micro-swimmers such as *Volvox*. These results are presented in Chapter 5 and Chapter 6.

3. **Model and observe the effects of a stratified, two-layered fluid on fluid flow generated by cilia.** This stratified fluid arrangement mimics the conditions in our respiratory system. We aim to observe the effects of viscosity differences and surface tension at the fluids' interface on flow velocities and flow structures generated by the cilia. These results are presented in Chapter 7.

1.4 Original Contribution

It has been commonly reported in literature that there is an optimum cilia spacing for maximum flow rate. We now show that correspondingly, in our model, there exists an optimum cilia density that gives rise to a maximum fluid slip velocity at the cilia tips. We also show that in the case of a two-fluid configuration, the existence of surface tension at the fluids' interface confines the vortex structures generated by the cilia to the lower fluid. As a result, higher fluid flow velocities are obtained by cilia activity. In addition, we report that viscosity ratios between the upper and lower fluids do not play a significant role in the average fluid flow velocities.

1.5 Outline of thesis

This thesis is organized as follows. In Chapter 2, we shall give a brief literature review of works investigating various aspects of cilia and flagella. In Chapter 3, we shall describe our numerical methods. In Chapter 4, we present benchmarks of our cilia model. In Chapter 5, we test the robustness of metachronal waves generated by our cilia model. In Chapter 6, we present results from a model consisting of an array of 21×21 cilia. In Chapter 7, we present results from a model with a stratified, two-fluid configuration. In Chapter 8, we present our conclusions and discussions on future work.

2 Literature review

2.1 Cilia and flagella in nature

Motile cilia and flagella possess an active internal mechanism that enables their beating action. This mechanism consists of 9 microtubule doublets arranged cylindrically around a central pair of microtubules [14]. This is commonly referred to as the “9+2” axoneme. A schematic of the cross section of an axoneme is shown in Figure 2.1.

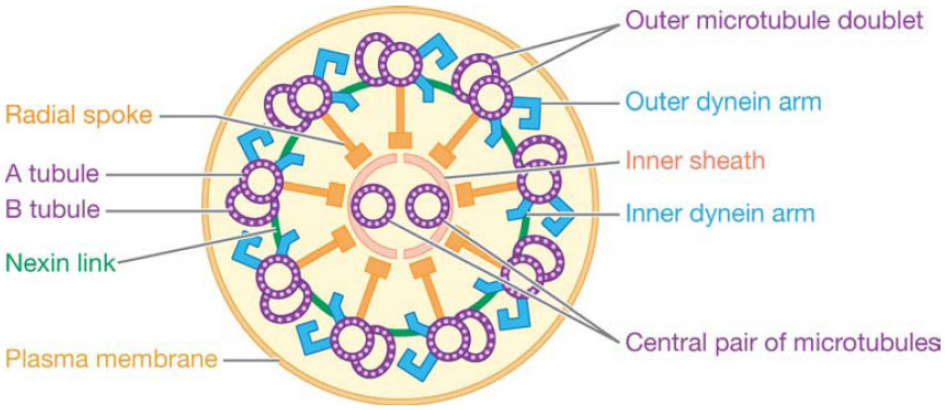

Figure 2.1 The internal axoneme of a cilium or flagellum is shown. Image is reproduced from Fauci and Dillon [14].

Dynein motors are arranged along the lengths of microtubule doublets. Dynein motors are proteins that provide the source of motion. Each dynein motor is attached at one end to a microtubule doublet in a permanent, ATP-independent fashion. Its other end is attached to a second neighboring microtubule doublet in an ATP-dependent fashion. The dynein motor then uses ATP as an energy source to “walk” along the second microtubule. This motion causes the microtubule doublets to slide along each other.

The sliding motion is converted into bending motion through the presence of nexin links and radial spokes. Nexin links are proteins that bind each microtubule doublet to its neighbours. Radial spokes are proteins that connect

the outer microtubule doublets to the central microtubule pair. Sliding between the microtubule doublets is thus restricted and the motion is converted into bending of the entire cilium/flagellum.

Cilia/flagella have a distinctive beat pattern, and there have been numerous efforts to understand the role dynein motors play to give the cilia/flagella its shape at each stage of the beat cycle. One remarkable early attempt by Sugino and Naitoh [15] used a trail-and-error method to uncover the dynein motor activation sequence required to give a cilium the shapes observed photographically by Machemer [16]. The activation sequence and resulting cilia shapes are reproduced in Figure 2.2. However, the mechanism required to give rise to this sequence is still not fully resolved [17], and is the subject of many studies. It should be noted that while excellent photographs and observations have been produced by Machemer in [16], these were primarily based on 2D visual observations of photographs. The beating shapes of cilia in 3D has since been widely accepted to be similar to that shown in Figure 2.2.

It appears the mechanism giving rise to the cilium beating sequence can arise spontaneously. Sanchez et al. [18] performed a remarkable experiment which showed that beating microtubule bundles can spontaneously form from a mixture of microtubules, kinesin, ATP and polyethylene glycol (PEG). Kinesin, like dynein, are motor proteins that enable motion on the cellular level. They function by ‘walking’ along a suitable medium. Dyneins move towards the ‘minus’ end of a microtubule, while kinesin moves towards to ‘plus’ end. Most notably, kinesin is known to be involved in cellular mitosis and package trafficking. The ATP in the mixture served as an energy source for the beating microtubule bundles while PEG served to facilitate assembly of the bundles.

The interactions between dynein motors driving cilia/flagella movements have been shown to be highly complex. Rai et al. [19] found that dynein motors have the ability to improve load-sharing through variation of step size. This leads to improved load-sharing within dynein groups, resulting in larger

collective force generation. In contrast, kinesin motors do not possess the ability to vary step size. Kinesin groups are therefore unable to share loads effectively and cannot collectively generate the large forces dynein groups are capable of.

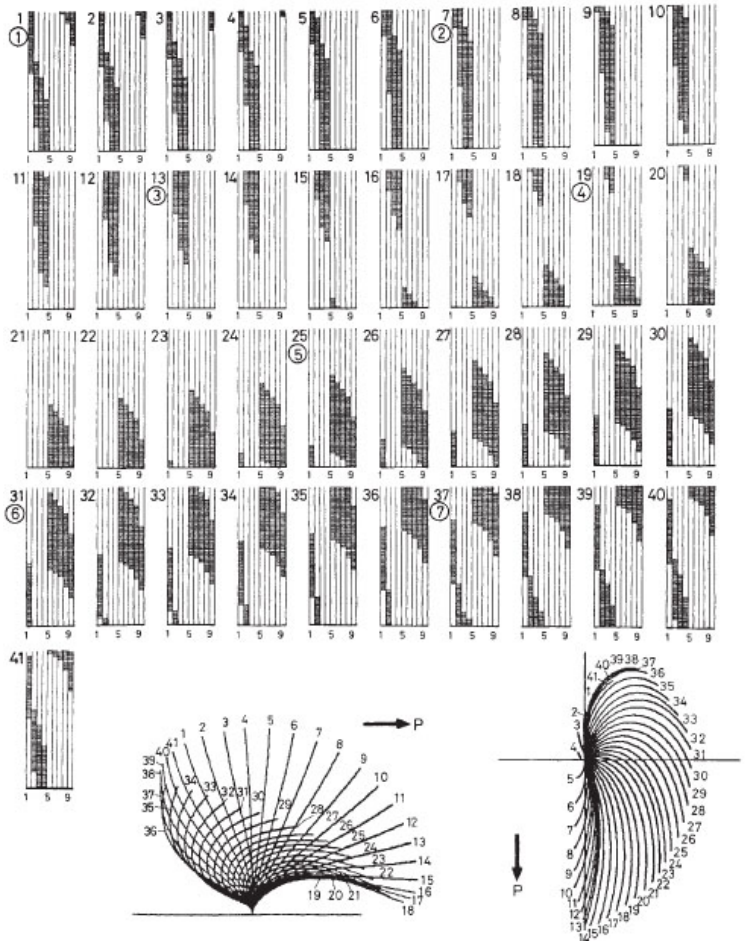

Figure2.2 Sugino and Naitoh [15] deduced the activation sequence of dynein motors that resulted in the observed beating shapes of cilia. The activation sequence of dynein motors are shown above while the resulting shapes of cilia are shown below.

An early attempt to study the effect of cilia beat on mucus transport was undertaken by Sanderson and Sleigh [20]. Here, the authors used high-speed photography and scanning electron microscopy to study cilia cut from the trachea of rabbits. The authors imaged and described the shapes of cilia in the forward and reverse strokes. The authors also described the existence of short-range metachronal waves across small patches of cilia (Figure 2.3). The

authors observed that during the forward stoke, cilia tips extend into the mucus layer to push the mucus forward, while during the reverse stroke, the cilia return to their initial positions beneath the mucus layer. This difference between the forward and reverse strokes is responsible for driving a net fluid flux.

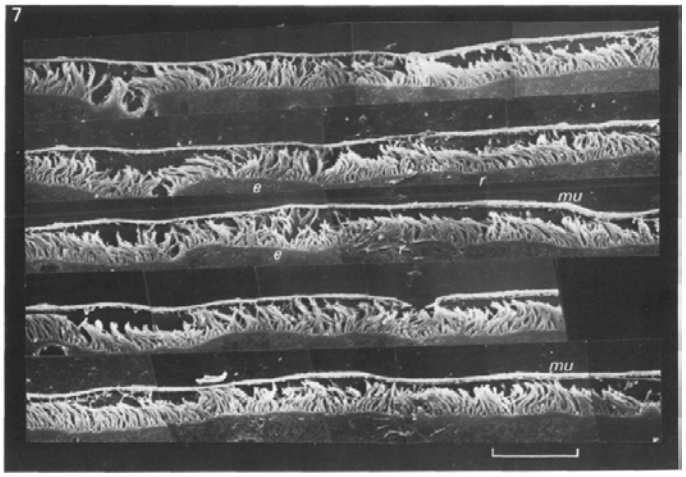

Figure 2.3 This figure shows a photograph by Sanderson and Sleigh [20] used to study metachronal waves in beating cilia.

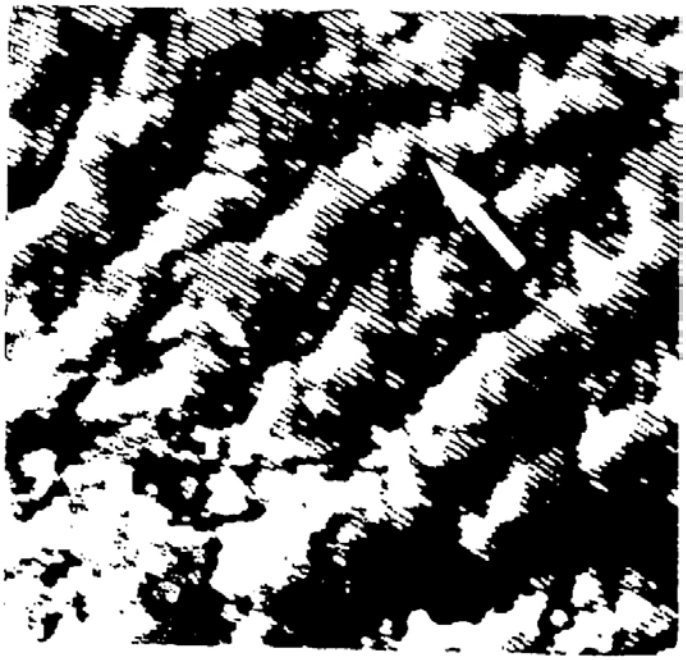

Figure 2.4 This figure shows a top view of an active ciliated cortical sheet extracted from *Paramecium multimicronucleatum* and attached to a glass slide (Okamoto and Nakaoka [21]). The arrow indicates wave propagation.

Following, Okamoto and Nakaoka [21] performed an experiment where ciliated cortical sheets from *Paramecium multimicronucleatum* were extracted and attached to glass slides. The cilia were then reactivated using cyclic adenosine monophosphate (cAMP) or cyclic guanosine monophosphate (cGMP) to form metachronal waves (Figure 2.4). The procedures for this remarkable experiment were pioneered by Nakaoka and Ooi [22], Bonini and Nelson [23] and Noguchi et al. [24]. The authors noted that the choice of cAMP or cGMP affected the direction of metachronal wave propagation. The authors also showed that increased concentrations of cAMP or cGMP caused metachronal wave frequencies to increase. There was no detectable difference in frequencies between the reactivated cilia on the glass slide and natural cilia residing on the paramecium, indicating that the basic functionalities of the cilia were not changed by the process of extraction from the paramecium and attachment to the slides.

As mentioned earlier, cilia are also used as propulsion in micro-organisms, an example of which is the paramecium. The paramecium is a single-celled organism with cilia covering its entire surface. The paramecium is able to control the beat of its cilia through the use of calcium ions. Iwadate and Nakaoka [25] showed that when caged calcium introduced into the paramecium were broken down by ultra-violet light, the calcium ions released caused a reversal in the direction of cilia forward stroke. This was accompanied by a contraction of the entire paramecium. The authors suggested that the release of calcium ions is a mechanism whereby the paramecium is able to change directions while swimming.

Another interesting micro-swimmer is the volvox. The volvox is similar to the paramecium in that its surface consists of a colony of flagellated algae. The algae reside on the extra-cellular matrix with their flagella pointed radially outward. Drescher et al. [26] studied the hydrodynamical interactions of mating volvox pairs. To model the effect of the numerous flagella, resistive force theory was applied to the volvox surface while lubrication theory was applied to the narrow gap between the volvox pairs. The authors then studied the different trajectories formed and suggested that spiraling trajectories

formed by volvox pairs helps in increasing the frequency of volvox contacts, greatly enhancing the reproduction process.

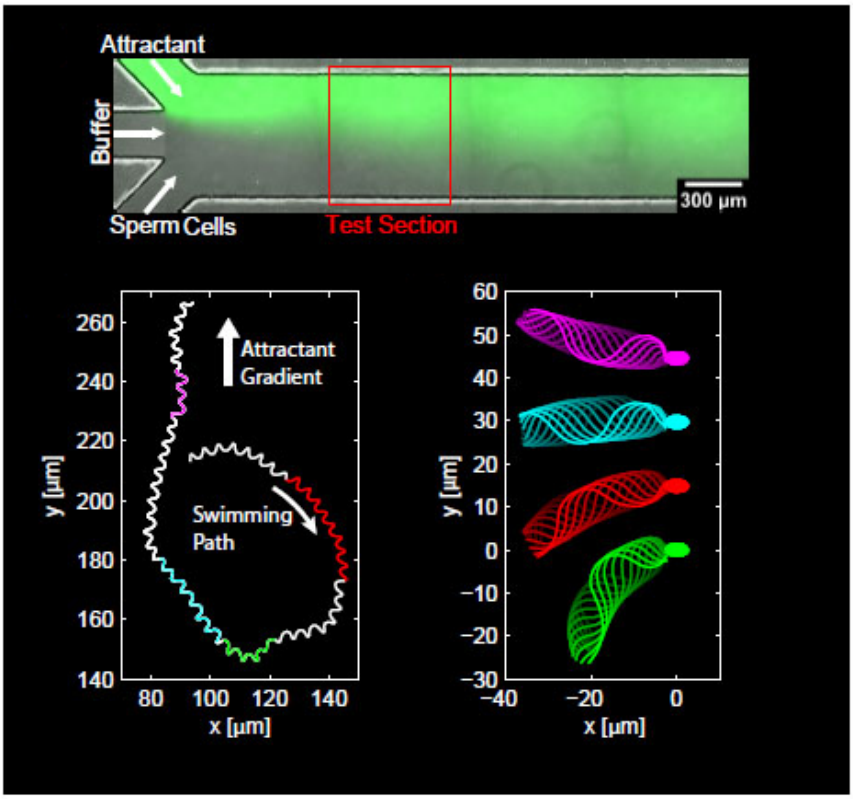

Figure 2.5 Guasto et al. [27] used a chemo-attractant gradient (top) to study the movement of bull spermatozoa. Each spermatozoon would swim in a circular path (lower left) to sense the chemo-attractant concentration. When it moving in the direction of increasing concentration, the spermatozoon adjusted its flagellum beat to change its swimming trajectory. Different types of flagellum beats observed by the authors are shown (lower right).

Besides passively interacting with surrounding fluid, flagella are also known to change their beat shape to aid in propulsion. Guasto et al. [27] imaged swimming spermatozoa in a chemo-attractant gradient (Figure 2.5). The authors reported that the flagellum of a spermatozoon would first beat in a way to cause the spermatozoon swim in a circular trajectory. This allowed the spermatozoon to sense the chemo-attractant concentration gradient over the diameter of its trajectory. When the spermatozoon sensed that it was swimming in the direction of increasing concentration, its flagellum modified its beat pattern such that a more linear trajectory was achieved. The spermatozoon alternated between linear and circular trajectories, allowing for

periodic course correction as it swam in the direction of increasing chemo-attractant concentration.

2.2 Artificial cilia and flagella in experiments

There have been interests in artificial cilia/flagella for the purpose of exploiting their numerous natural properties, examples of which include enhanced diffusion and improved mixing.

Shields et al. [28] fabricated cilia made of nanoparticle-polydimethysiloxane (PDMS) (Figure 2.6). These were essentially stalks of PDMS embedded with nanoparticles. The nanoparticles allowed the cilia to respond to an externally applied magnetic field. The artificial cilia were about 700nm in diameter and 25μm in length, making them about five times larger than natural cilia.

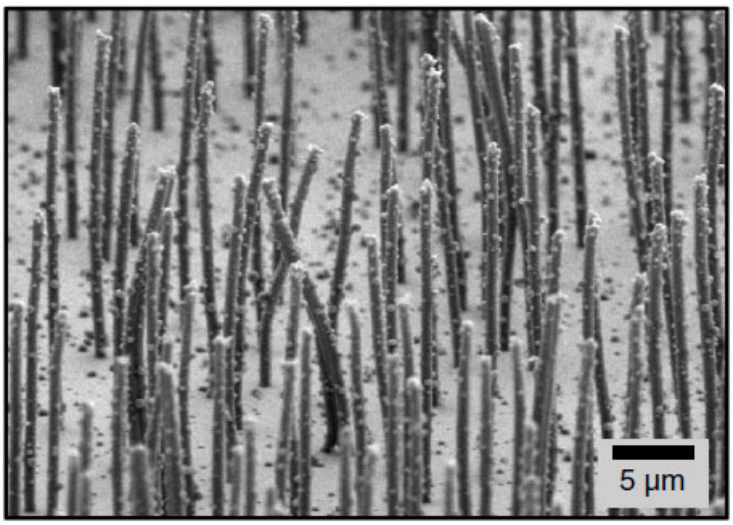

Figure 2.6 Artificial cilia made from PDMS are shown. The inclusion of nano-particles allows the cilia to react to an externally applied magnetic field. Image reproduced from [28].

The cilia were put in a fluid-filled chamber and angled to the substrate using an external magnetic field. A second rotating magnetic field was then superimposed over the first, causing each cilium to sweep a conic trajectory. This was done to mimic the cilia motion observed in a mouse embryo node.

By observing nanoparticles suspended in the fluid, the authors described two flow regions. The first region was observed above the cilia tips. This region made up the bulk flow. Here, a Poiseuille-Couette flow was established, i.e. the flow velocity profiles were observed to be parabolic. Maximum velocity occurred at the cilia tips and zero velocity occurred at the chamber ceiling. A recirculation region was also observed. Particles directly above the cilia moved continuously in the direction of bulk flow while particles directly below the chamber ceiling moved in the direction opposite to bulk flow. This recirculation was attributed to the enclosed nature of the chamber.

The second flow region was observed below the cilia tips. Here, the motion of particles was rapid but nondirectional. Particles oscillated back and forth quickly with little net motion. This region offered improved effective diffusivity.

Babataheri et al. [29] conducted similar experiments involving artificial cilia. In this study, the authors termed their artificial cilia “fleximags”. A carpet of fleximags was created and put in an magnetic apparatus. The apparatus produced magnetic fields in x-, y- and z-directions. The magnetic field was then made to give 2D planar or 3D motions. In the case of 2D planar motions, a magnetic force was applied in the y-direction, holding the fleximags at an angle to the substrate. The x-component of the magnetic force was then varied, causing the fleximags to move back and forth. In the case of 3D motions, the x- and y- components of the fields were oscillated. The shapes from experiment were shown to be in good agreement with shapes predicted from resistive force theory.

The authors tried to induce a net flux by imposing an asymmetry in the form of a fast forward stroke followed by a slow backward stroke. In the case of planar motion, the authors found that the net flux was lower than the flux of either the forward or backward strokes by two orders of magnitude. This was an indication of low pumping efficiencies when fleximags/cilia were used for fluid propulsion.

The authors also reported that since the shape of the fleximag changed throughout its stroke, the total force on the fleximag need not be proportional to the base torque. However, when the authors plotted the total force (deduced from the shapes of the fleximags) and compared it to the torque at the base (deduced from the angle at the substrate), they found a linear relationship. The system had in effect only one degree of freedom.

The authors reasoned that since the net base torque over a complete cycle was zero, the net force on the fleximag over a complete cycle must also be close to zero. This meant the net flux should also be close to zero. Therefore, the reason for a small net flux was due to the slight difference in shapes between the forward and reverse strokes.

Vilfan et al. [30] described the creation and study of self-assembled artificial cilia. The authors first produced micro trenches on a photoresist layer. The trenches were then used as guides as superparamagnetic beads were self-assembled into chains. These chains then formed the artificial cilia. Again, the cilia were actuated by an external magnetic field. The authors monitored the flow field by observing the advection of non-magnetic, tracer particles embedded in the fluid. The authors showed that the particles exhibited a spiral, corkscrew trajectory.

In a subsequent experiment, the Kokot et al. [31] used optical tweezers to assemble the cilia. In this study, the authors again monitored the flow field, this time using fluorescent tracer particles. The authors showed that there exists a linear relationship between the cilia beat frequencies and fluid flow velocities; the higher the beat frequencies, the higher the flow velocities.

Oh et al. described the manufacture and study of artificial cilia [32, 33]. In these studies, the artificial cilia were made to oscillate by piezoactuators. The piezoactuators were attached to microfluidic devices holding the cilia, and movement of the microfluidic devices caused the cilia to oscillate. By

operating at the resonance frequencies of the cilia, large oscillating amplitudes could be achieved.

In [33], the authors performed experiments and simulations of cilia in an enclosed, circular chamber. The authors showed that the presence of actuated cilia gave an 8-fold reduction in mixing times over cases where diffusion was the only mechanism for mixing. However in this study, a time-averaged, net flow of the fluid was observed. This net flow was symmetric about the symmetric axis of the cilia array. This observation indicated that cilia movement was reciprocal and symmetrical in both the forward and reverse strokes. According to Purcell's scallop theorem [34], if the movement of an actuator at low Reynolds numbers is reciprocal, there will be no net movement of either the fluid or the actuator. Therefore, the presence of a net fluid flow in this study indicated that the cilia were likely not operating at low Reynolds numbers.

This work was expanded upon by Kongthon et al. [35, 36] and by Kongthon and Devasia [37]. Here, mathematical models were included. The cilia was modelled as Euler-Bernoulli beams. The beam dynamics included both the added-mass effects and inertial effects of the surrounding fluid. The authors showed that actuated cilia could tremendously improve the mixing capabilities of their microfluidic device.

It should be noted that the artificial cilia in these studies were approximately 2 orders of magnitude longer than natural cilia, and the frequencies of the artificial cilia were approximately 5 times higher than that of natural cilia. It is therefore possible that the cilia were not operating under conditions of low Reynolds numbers; therefore inertial effects of both the fluid and the cilia contributed significantly to the mixing effects.

It is worth noting here that a somewhat similar numerical treatment of passive stereocilia was shown by Zetes and Steele [38]. Here, both the inertial effects of the cilia and the viscous effects of the surrounding fluid were taken into account; however inertial effects of the surrounding fluid was neglected.

Unlike cilia found on micro-swimmers or in respiratory systems, the frequencies typical of stereocilia are significantly higher ($10^0 \sim 10^6 Hz$). As such, inertia of the stereocilia was also expected to play a significant role in the response of the system.

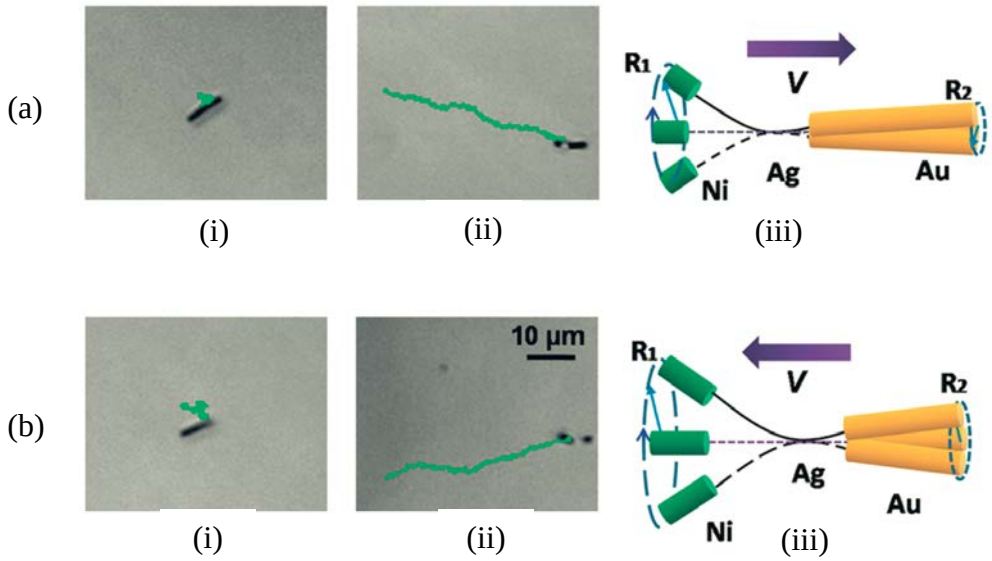

Figure 2.7 Artificial micro-swimmers made by Gao et al. [39] is shown. The swimmers were made of a nickel end, a silver middle and a gold head. Swimmers could be either "pushers" (a) or "pullers" (b). Rigid swimmers with a constant diameter were unable to move, as shown in a(i) and b(i), while swimmers with a flexible middle were able to, as shown in a(ii) and b(ii). Different lengths of nickel/gold sections changed the swimmers from "pushers" to "pullers", as shown in a(iii) and b(iii).

Besides studying artificial cilia attached to substrates, there have also been studies involving free swimmers actuated by artificial flagella. A remarkably simple flagellated swimmer was created by Gao et al. [39]. The swimmers were made of 3 sections: a gold "head", a silver middle and a nickel "tail" (Figure 2.7). The swimmers were created using conventional nano-wire growing techniques. Hydrogen peroxide was then used to erode the silver middle, causing its diameter to decrease and hence enabling the structure to bend.

The authors then used a changing magnetic field to actuate the nickel end,

essentially causing it to rotate like a miniature propeller. The entire structure thus wriggles, and depending on the relative lengths of the gold and nickel ends, the swimmer can propel itself forward or backward, in effect changing from a "puller" to "pusher". This is shown in Figures 2.7(a) and (b).

The authors pointed out is that if the silver middle was not eroded, i.e. if the swimmer was rigid, the swimmers would still wriggle in the magnetic field but no net locomotion was possible. It seemed deformability was crucial for the propulsion of the swimmers at low Reynolds numbers.

2.3 Cilia and flagella in simulations

There has also been considerable interest in the modeling of dynamics of free-swimming micro-swimmers. An excellent overview of this subject has been provided by Lauga and Powers [40]. An example of a model of a micro-swimmer was presented by Vladimirov. Here, the author demonstrated that when the swimmers were idealized as chains of spheres [41] or as simple dumbbells [42], analytical solutions to their dynamics could be readily obtained.

An example of numerical simulations involving explicit modeling of cilia was presented by Vaughan et al. [43]. Here, finite element models were used to model osteocytes and osteoblasts in vitro and in vivo. Each cell had a passive cilium attached to its top. In vitro simulations modelled cells in a flow chamber, while in vivo simulations modelled cells in a fluid-filled lacular cavity. The simulations enabled observation of stresses at the cilia base. These stresses were then observed to be transmitted to the cell bodies. These stresses have been suggested to be part of a mechanotransduction process, and are responsible for the triggering of biochemical signals.

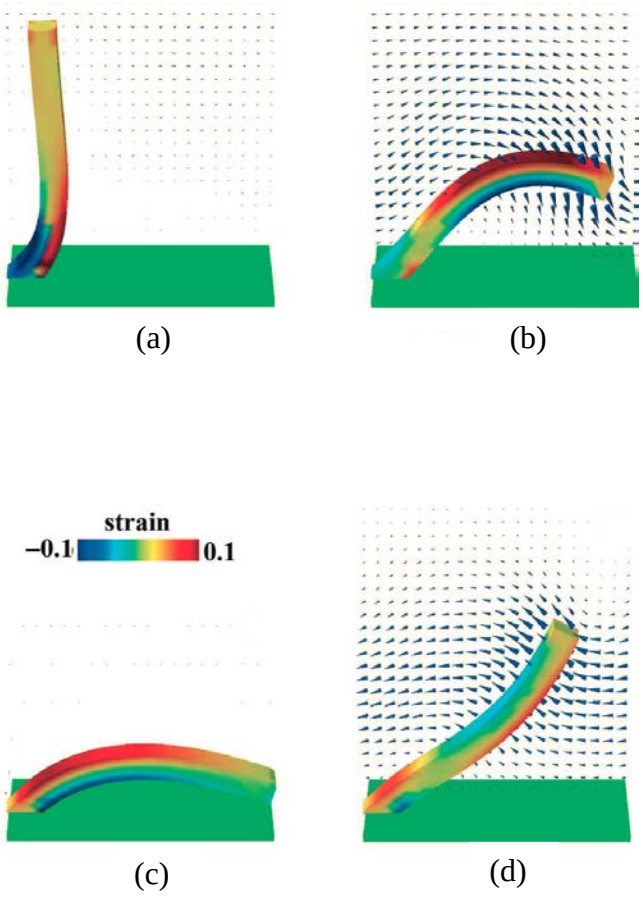

Figure 2.8 Snapshots of simulations of cilium performed by Alexeev et al. [44] are shown. The cilium was modelled with a spring network and the fluid was solved using the lattice Boltzmann method. The cilium was held at 45° to the substrate and a vertical force was applied at the tip. A single cilium was simulated with periodic boundary conditions to mimic an infinite cilia bed.

Another example of explicit modeling of cilia was presented by Alexeev et al. [44]. In this study, the cilium was modelled using a spring network with an associated Youngs' modulus. The cilium was angled at 45 degrees to the substrate (Figure 2.8). The fluid was solved using the lattice Boltzmann method while the fluid-structure coupling was carried out using a lattice Boltzmann method/lattice spring model approach. An oscillating vertical force was then applied at the cilium tip. One cilium was simulated with periodic boundary conditions, hence effectively simulating an infinite cilia bed.

The authors grouped cilia length, beat frequencies, fluid viscosity and bending moduli into a non-dimensional Sperm Number. Through the simulations, the

authors found that net flow volume reversal was possible through variation of the Sperm Number.

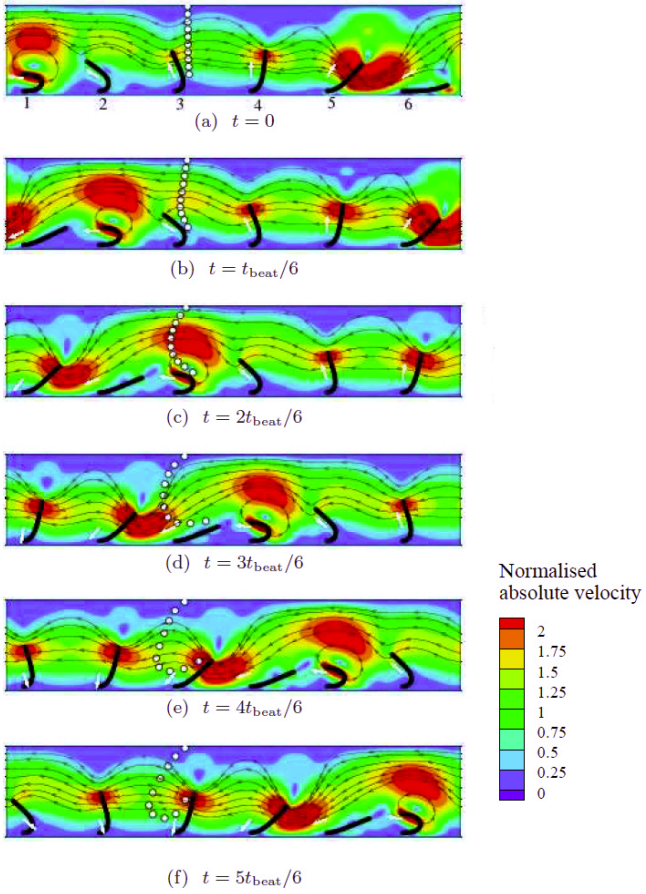

Figure 2.9 Snapshots from cilia simulations by Khaderi et al. [45] are shown. Antiplectic metachrony is displayed. Contours represent fluid velocity magnitudes and streamlines represent fluid direction. White circles represent the displacements of passive particles while white arrows denote the direction of the applied magnetic field.

Khaderi et al. [45] studied the effects of metachronal waves on cilia beds (Figure 2.9). Here, the authors simulated cilia that were subjected to external oscillating magnetic fields. This effectively enabled their simulations to mimic experiments involving artificial magnetic cilia. The simulated cilia were 2D in nature, and a spatial phase difference in the driving field was imposed. The cilia were treated as elastic Euler-Bernoulli beams taking into account geometric non-linearity. The Maxwell equations were solved to determine

body couples on the cilia, and the coupled Stokes equations were solved for the fluid.

The authors identified three non-dimensional numbers governing the behavior of the system: the magneto-elastic number, the fluid number and the inertia number. The magneto-elastic number is a ratio of magnetic force to elastic force, the fluid number is the ratio of viscous force to elastic force, and the inertia number is the ratio of inertia of the cilia to its own elastic force.

The authors studied mainly the case of antiplectic metachrony. The authors found that there was no instance where flux was reversed. This observation was due to the fact that as a single cilium was in the recovery stroke, most of the surrounding cilia were in the forward stroke; hence net flux in the backward direction was always suppressed. Also, the recovering cilium generated a vortex about its tip instead of causing an opposing flux. This was due to the other cilia around it beating in the forward stroke. This action shielded the effects of the cilia in the recovery stroke.

The authors also studied the flow rates generated by a cilia bed with and without metachronal waves. They found that in the case without metachronal waves, large fluxes were generated during both the forward and recovery strokes. The net flux was non-zero, but propulsion efficiency was reduced. When metachronal waves were imposed, the opposing flux caused by cilia undergoing the recovery stroke was reduced and propulsion efficiency increased.

This increase in flux brought about by metachrony was shown in a subsequent 3D study [46]. Here, the authors found that while both symplectic and antiplectic metachrony produced higher flux than the case of no metachrony, antiplectic metachrony produced higher flux than the case of symplectic metachrony. In addition, for the case with no metachrony, the authors investigated the effects of cilia spacing on flux. The authors reported a steady decrease in flux with increase in cilia spacing. There was no optimum cilia

spacing which gave rise to a maximum flux. This aspect of an optimal cilia spacing will be investigated in Section 6.3 of this thesis.

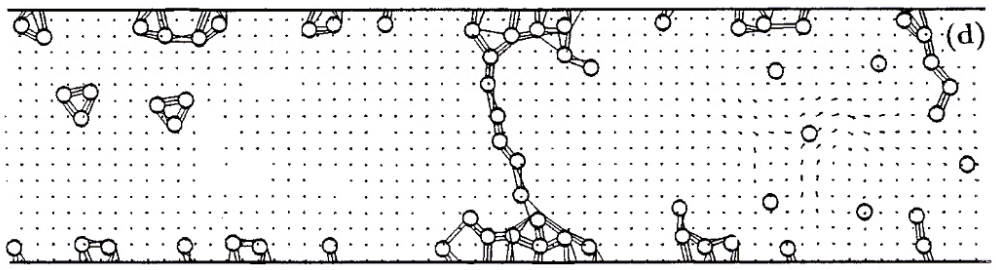

Figure 2.10 Dillon et al. [47] simulated the formation of biofilm caused by bacteria. The freely-moving, flagellated bacteria were immersed in a fluid. The fluid-bacteria interaction was coupled using the immersed boundary method (IBM). Adhesion between bacteria bodies was modelled using an elastic spring.

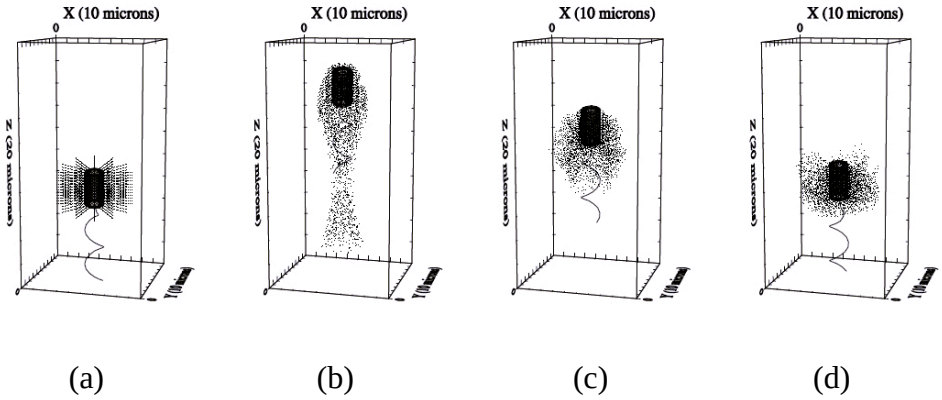

Figure 2.11 Simulation results of a swimming bacterium are shown. The bacteria body was made of a spring network. The bacteria tail was modelled as a rigid spiral and was regenerated from the body at each time step. Opposing torques applied on the body and tail propel the bacteria. IBM was used to couple the spring network to its surrounding fluid. Image reproduced from [49].

Finally, the authors varied the cilia spacing, hence changing the cilia density. The authors found that when cilia spacings were large, metachronal wave speeds did not make much difference in net flux. However, when the spacings were small, there was significantly greater net flux in the presence of antiplectic waves compared to symplectic waves. The authors concluded that antiplectic metachrony should be favoured in nature, but noted that there are many organisms that exhibit symplectic metachrony. This suggests that

symplectic metachronal waves may be optimised for some other as yet unknown property.

Dillon et al. [47] used the immersed boundary method (IBM) [48] to study the formation of biofilm (Figure 2.10). Biofilm in nature are known to be formed by flagellated bacteria. Although our interest is mainly in flagellated eukaryotic cells rather than flagellated bacteria, in this instance the authors presented an excellent example of how IBM can be used to simulate the hydrodynamic interactions of swimming organisms. In this study, a pair of point forces was imposed behind each bacterial body to simulate the flagella action. These forces represent a virtual flagellum that was regenerated according to the body orientation after each time step. Since the flagellum was not explicitly simulated as an immersed boundary structure, its hydrodynamic coupling with the fluid was only one-way, i.e. the flagellum exerts a force on the fluid but it is not explicitly advected by the fluid.

In addition, adhesion forces between bacteria bodies were also modelled by a mechanism of linear elastic springs. The adhesion mechanism allowed the simulation of aggregation of bacteria on surfaces of walls.

Hsu and Dillon [49] later extended this method to simulate swimming bacteria (Figure 2.11). The authors modelled each bacteria body as a cylindrical spring network. Again, the rotating flagellum was simulated by imposing a series of forces on a spiral behind the body. The forces on the flagellum contributed a torque on the fluid; hence a corresponding, opposing torque was imposed on the body. As in [47], the location of the flagellum was assumed to move together with the body. The flagellum was regenerated after advection of the bacteria body at each time step.

Lee et al. [50] presented a 2D model of muco-ciliary transport where the motion of cilia was prescribed. This prescribed motion was imposed by calculating the fluid body forces necessary to cause the cilia to advance through a set of prescribed positions. In this model, the cilia resided in the PCL beneath a mucus layer. Both the PCL and mucus layer were treated as

Newtonian fluids. The interface between PCL and mucus was treated using the immersed boundary method where surface tension effects were considered. In this study, the authors found that increasing viscosity in the mucus layer reduced the mean mucus velocity, while increasing the cilia density increased the mean mucus velocity.

The authors later extended this work to model 3D cilia in a single fluid [51]. Similar to Khaderi et al. [45-46], the authors reported that the existence of imposed metachronal waves smoothed out the oscillating flow of the surrounding fluid, resulting in a higher net fluid flow rate. In a further work [52], the authors imposed a random phase difference on each cilium in an array. The authors found that this array offered similar fluid flow rates to an array in which all cilia were in phase. This study implied the importance of a coherent metachronal wave.

In [52], the authors also simulated conditions where varying numbers of cilia within the array were immotile. The authors found that fluid flow rate decreased linearly as the number of immotile cilia increased. Besides this, the authors found that ciliary beat patterns and cilia lengths were optimized to give maximum flow rates. However, it should be noted here that the authors compared the cilia's natural beat pattern with beat patterns that were "inferior", i.e. "windscreen wiper" motions and stiff planar motions. In contrast, as will be mentioned later, Guo et al. [67] compared the natural cilia beat patterns between *Opalina* cilia and rabbit trachea cilia.

Since Pozrikidis [53], the methods of Stokeslets have been a popular way to model Stokes flow. Similar to Dillon et al. [47], Cortez et al. [54] used the immersed boundary method together with the method of regularized Stokeslets [55] to simulate the movements of a flexible, helical swimmer. In this study, the swimmer was a 3D structure consisting of control points connected by springs. Smith [56] extended the use of the same method to simulate choanoflagellates and cilia. Here, the flagella of the choanoflagellate and the cilia were reduced to simple, one-dimensional structures. The method of regularized Stokeslets has also been extended to study flow around prolate

spheroids [57] in general. Since then, the method of regularized Stokeslets has been further developed to be applicable near walls [58, 59].

One fundamental aspect of cilia or flagella is their efficiency in propelling fluid. An early form of the idea of efficiency, or optimization, was put forward by Lighthill [60]. Lighthill measured efficiency as the ratio of power needed to overcome viscous drag to the power exerted by the micro swimmer. Osterman and Vilfan [61] attempted to determine if the cilia dynamics on a paramecium was indeed optimized. The authors defined an efficiency based the ratio of flow rate to power utilized by each cilium. The authors compared several cases. The first case modelled each cilium as a single free bead, the second case modelled each cilium as a bead at constant distance from its origin, the third case modelled each cilium as a stiff row of beads and the forth case modelled each cilium as a flexible row of beads. The authors found the last case to be most efficient. The authors also found that although the efficiency of paramecium cilia was less than 1%, the beat stroke of the cilia was still highly optimized.

In the case of micro-swimmers, the optimal swimming stroke of a swimmer at low Reynolds numbers was obtained by Avron et al. [62]. Here, the authors used the ratio of energy dissipated per unit length of the swimmer to its velocity as a measure of its inefficiency. The authors thus obtained the shapes a 2D circular swimmer must evolve through for maximum swimming efficiency. Early analysis on the shapes of a micro-swimmer can be found in studies by Saffman [63] and by Shapere and Wilczek [64].

Similarly, attempts to obtain the optimized shape of a flagellum were presented by Spagnolie and Lauga [65] and by Lauga and Eloy [66]. Here, the flagellum was modelled as a sinusoidally travelling wave. In both works, efficiency was defined as the ratio of work done to drag a single, undeformed flagellum through the fluid to the work done by the undulating flagellum if it propelled itself with the same velocity.

While on the subject of efficiency, Guo et al. [67] numerically studied and compared the beat patterns of cilia found on the protozoan *Opalina* with that found in the rabbit trachea. Surprisingly, the authors found that *Opalina* cilia exhibited higher efficiency than that of the rabbit trachea cilia. The authors therefore showed that rabbit trachea cilia were not optimal, since there exists a cilia beat pattern possessed by the *Opalina* cilia that was more efficient.

Another interesting result on the subject of optimal swimming was reported by Li and Spagnolie [68]. Here, the authors studied swimmers in the form of rigid, rotating cylinders with helical cross-sectional profiles. These swimmers therefore resembled rotating screws. The authors parameterized the cross-sectional profiles and found that there existed optimal swimming velocities for certain "screw thread" depths. Optimal swimming velocities were also found for swimmers possessing various numbers of "screw threads".

There have also been interests in the mixing abilities of cilia. Khatavkar et al. [69] presented a numerical study on the mixing abilities of a two-cilia system. Mixing was quantified by observing the displacement field of the fluid using a front-tracking method. The authors reported that in a two-cilium system where the cilia were separated by a distance approximately equal to their length, a phase difference of $\pi/2$ gave optimal mixing. The authors reported that this configuration caused a "blinking vortex system". This was a system where dominant vortices were formed alternately at each cilia tip, giving rise to chaotic advection and mixing [70].

Of special interest to us are models of cilia capable of spontaneously producing metachronal waves. To achieve spontaneous formation of metachronal waves, models often utilize a non-linear, active switching mechanism. As dynein has been shown to be responsible for cilia activity, this active switching mechanism is often designed to mimic dynein activity. An early discussion on the dynein activation models for cilia activity was given by Murase [71], while a more recent summary was provided by Linderman and Lesich [72]. In this summary, the authors mentioned that there has been a few competing views on the nature of this switching mechanism. There is the

curvature control mechanism proposed by Brokaw [73-76], the central-pair spoke mechanism proposed by Omoto and Kung [77-78], the dynein cross-bridge cycle mechanism proposed by Sugino and Naito [79] and Murase and Shimizu [80], and perhaps most recently the geometric clutch hypothesis proposed by Lindemann [81]. This last mechanism is a more general description of the curvature-controlled model.

Building on earlier work [82-84], Gueron and Levit-Gurevich [85] constructed a model consisting of a "geometric switch". The authors showed that as the number of cilia in their model was increased, the hydrodynamic coupling between the cilia reduced the energy required per cilium to generate the same flow. The authors also showed that when the fluid viscosity was in the range of $\mu_{water} < \mu < 5\mu_{water}$, there was little difference in the energy consumed per cilia.

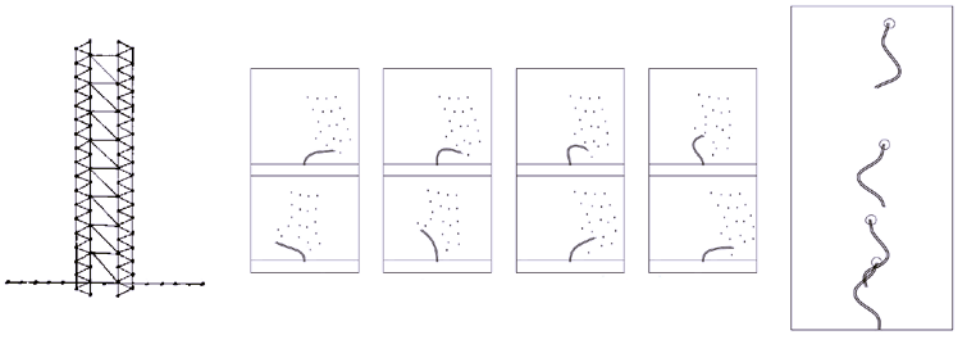

Figure 2.12 (a) The cilium model proposed by Dillon et al. [86] is shown. The model used a spring network with crosslinks to mimic the role of microtubules and dynein motors. (b) Snapshots of a single cilium undergoing its beat cycle is shown. The cilium stroke was controlled by its curvature. (c) The same cilium model could be applied to the flagellum of a swimmer.

A 2D example of a geometric clutch model was implemented by Dillon et al. [86]. The authors presented realistic simulations of cilia using IBM [48] (Figure 2.12). The cilia were modelled as a pair of microtubules, each represented by spring filaments with diagonal cross-links. The resultant spring networks were highly resistant to stretching, while bending stiffness was

provided by cross-links. In addition, the dynein action was modelled as diagonal links binding the pair of microtubules. The authors defined two forms of dynein arrangements. The first arrangement was the left-to-right arrangement. Here, dynein springs that were permanently attached to the left microtubule could detach from the right microtubule. The second arrangement was the right-to-left arrangement. Here, dynein springs permanently attached to the right microtubule could detach from the left microtubule. Curvature between the two microtubules was used to determine if the dynein springs were in the right-to-left or left-to-right arrangement.

The authors reported that their spring model could also be used to model a swimming organism. This work therefore showed how a single model could be used effectively to model both cilia and flagella. This was possible because of the internal structural and mechanical similarities between cilia and flagella.

This study was later extended by Yang et al. [87] to model multiple cilia. In this study, the authors demonstrated that the geometric clutch mechanism could enable cilia to spontaneously generate metachronal waves.

A 3D example of the clutch model was presented by Elgeti and Gompper [88]. Again, the cilia here were made up of linear spring elements with cross links. However, instead of a mechanism where cross linked springs were made to attach or detach from the microtubules, the rest lengths of springs were simply varied to simulate cilia activity. By modeling patches of 20×20 cilia or 60×60 cilia, the authors showed that metachronal waves could spontaneously form. The authors showed that in their model the metachronal waves travelled mostly at an angle of $30° - 50°$ relative to the power stroke, i.e. the waves were symplectic in nature. The authors also reported an optimal efficiency when the cilia were spaced at about half their lengths, i.e. $d / L \sim 0.5$.

Vilfan and Jülicher [89] offered an alternative to explicit modelling of cilia. A pair of cilia was simplified into point forces moving in elliptical trajectories. By solving the incompressible Stokes equations, solutions to the flow-field

was obtained. The solutions showed regions where cilia beat in either synchrony or asynchrony. A range of phase differences was possible when the cilia were close, but the phase differences could take on only values approaching 0 rad and π rad when the distance between the cilia pair increased to infinity.

Lagomarsino [90] and Wollin and Stark [91] studied the onset of metachronal waves by again simplifying each cilium into a discrete point. The cilium points were then confined to oscillate in one dimension. A parameter describing the positions of the points was then used to approximate the geometric switch, allowing each point to switch between the forward and reverse strokes. A similar study was carried out by Niedermayer et al. [92], where the conditions under which chains of cilia are able to produce metachronal waves was presented.

It can therefore be concluded that there is much interest in the dynamics of cilia and flagella. Artificial cilia are shown to be applicable to micro mixers, and artificial micro-swimmers have the potential to be developed into miniature robots. Much effort has been spent on describing the internal mechanisms of the axoneme in order to achieve accurate models of cilia and flagella, yet because of computational challenges, these models are at present highly simplified.

We seek to further the work on cilia by studying a simplified model. Similar to the works by Dillon et al. [86] and Yang et al. [87], our work uses a numerical method based on IBM to simulate cilia-fluid interactions. We shall describe our method in the next chapter.

3 Numerical implementation of the immersed boundary method (IBM)

3.1 Implementation of governing equations and formulation of fluid solver

The immersed boundary method (IBM) was first described by Peskin [48] as an efficient method to couple the movements of an immersed, deformable solid structure to its surrounding fluid. It was first used to model the pumping movements of the human heart [93-98]. Since then, it has been shown to be applicable to a multitude of micro-scale problems that are biological in nature. Examples of such problems include studies on the deformations of cells in shear flow [99, 100] and studies on the aggregation of blood platelets [101, 102].

The IBM consists of a fixed fluid Cartesian grid. The discretized solid structure grid is then superimposed over the fluid grid. The traditional form of the IBM relies on a numerical form of the Dirac delta function to facilitate fluid-structure interactions. Point forces on the solid structure are passed to the fluid grid through this delta function. The fluid variables are then solved, and the fluid velocities passed back to the solid structure using the same delta function. The solid structure can then be advected according to those velocities.

If the immersed deformable solid structure takes the form of an enclosed membrane, then the IBM has a tendency to allow leakage of fluid through the membrane [103]. As a result, mass loss is a phenomenon commonly observed in simulations involving enclosed membranes. It is also well-known that this mass loss phenomenon is a deficiency in numerical implementation. The common and easy solution to overcome this deficiency is to have a membrane mesh finer than the fluid grid. However, our cilia do not present an enclosed

membrane where mass leaks through; therefore this mass loss phenomenon does not present a problem in our simulations.

An improvement to the IBM is the immersed interface method (IIM) [104]. In the IIM, discontinuities in variables (e.g. pressure and forces) across the immersed membrane are accounted as additional correction terms in the Navier-Stokes equations. However in our case, the cilium is represented as a 1D structure in 3D space. It therefore does not present a membrane where discontinuities in variables can be computed. Implementation of IIM in 3D is also significantly more tedious and time-consuming than IBM. We therefore consider the IBM satisfactory for our purposes due to its ease of implementation over the IIM.

With the mechanism of force transfer between the solid structure and the fixed fluid Cartesian grid, the IBM negates the need for any form of deforming grids or re-gridding. In addition, the fluid Cartesian grid can be a structured grid. The indices describing the grid are therefore ordered, making implementation of the method straightforward. This gives the IBM a distinct advantage over more advanced (e.g. Galerkin [105]) methods.

This study seeks to model each cilium as a one-dimensional elastic structure immersed in a Newtonian fluid. The fluid and cilia form a coupled system that is modelled using IBM. The cilium deforms and exerts forces on the fluid, while the motion of the fluid in turn determines the motion and deformation of the cilium. Figure 3.1 shows a simplified diagram of IBM.

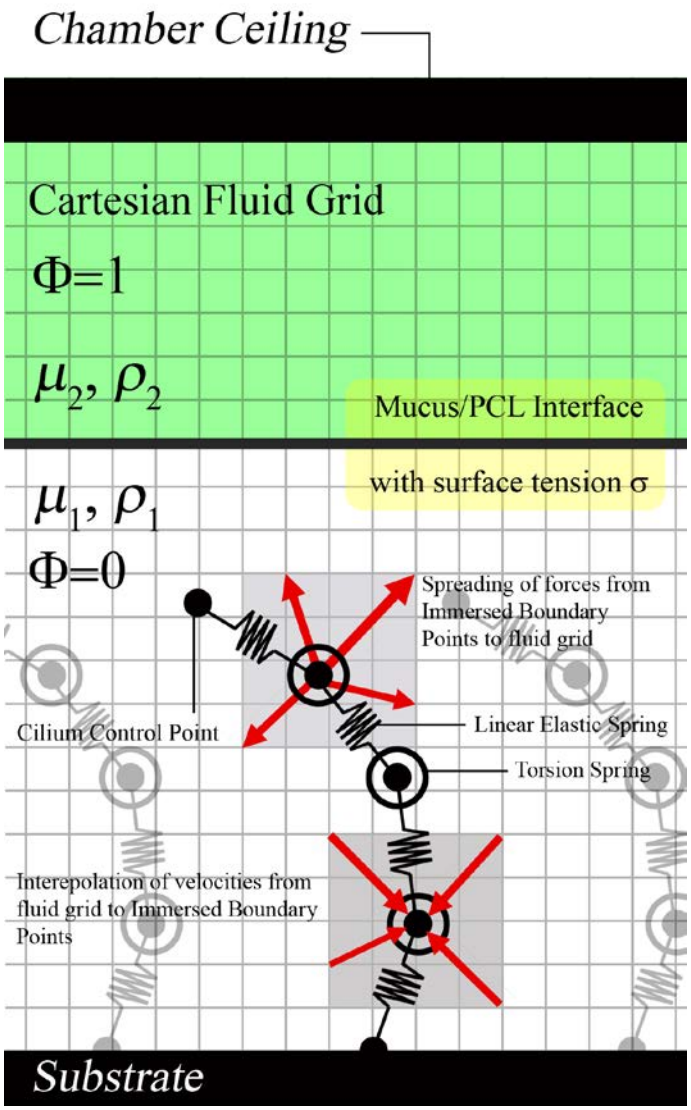

Figure 3.1 The Immersed Boundary Method (IBM) complete with a single cilium is shown. The cilium is discretized as a series of points joined by linear elastic springs. The inclusion of torsion springs at control points provides a bending resistance. Forces are spread to the fluid grid for the solving of the Navier-Stokes equations. After the Navier-Stokes equations are solved, velocities are interpolated from the fluid grid to advect the cilium points. In cases where two fluids are present, the second fluid sits above the first fluid as an additional layer (hatched region). The lower fluid possesses viscosity μ_1 and density ρ_1 while the upper fluid possesses viscosity μ_2 and density ρ_2. The two fluids are separated by an interface with surface tension σ. In the case where $\mu_2 = \mu_1$, $\rho_2 = \rho_1$ and $\sigma = 0 Nm^{-1}$, the system behaves as if only a single fluid is present.

In this study the fluid is regarded as viscous and incompressible. The governing equations for the fluid are thus the momentum equation

$$\frac{\partial \vec{u}}{\partial t}+\left(\vec{u}\cdot\vec{\nabla}\right)\vec{u}=-\frac{1}{\rho}\vec{\nabla}p+\vec{\nabla}\left(\upsilon\vec{\nabla}\cdot\vec{u}\right)+\frac{1}{\rho}\vec{f}(\vec{X},t)\delta\left(\vec{x}-\vec{X}\right)+\frac{1}{\rho}\vec{F}_{\sigma}\left(\vec{x},t\right)\ , \quad (3.1)$$

and the continuity equation

$$\vec{\nabla}\cdot\vec{u}=0\,. \quad (3.2)$$

Here, ρ is the fluid density, $\upsilon=\mu/\rho$ is the fluid kinematic viscosity, $\vec{u}=\left[u\,v\,w\right]^{T}$ is the fluid velocity, p is the fluid pressure, $\vec{f}\left(\vec{X},t\right)=\left[\,f_x\ f_y\ f_z\,\right]^{T}$ is the force exerted by the cilium on the fluid and $\vec{F}_{\sigma}\left(\vec{x},t\right)$ is a force arising from surface tension. In our model, the surface tension is spread over a small thickness; hence $\vec{F}_{\sigma}\left(\vec{x},t\right)$ represents a body force. $\delta\left(\vec{x}-\vec{X}\right)$ is a 3D delta function, $\vec{X}=\vec{X}\left(s,t\right)$ represents the coordinate of the cilium and s is the Lagrangian coordinate along the cilium. These equations are collectively known as the Navier-Stokes equations.

In our simulations, we shall solve the incompressible Navier-Stokes equations using the projection method described by Chorin [106, 107]. Here, an intermediate velocity $\vec{u}^{*}$ is first obtained. Next, an update φ to the pressure is obtained. This is followed by an updating of $\vec{u}^{*}$ to obtain $\vec{u}^{n+1}$, which is the actual velocity at the next time step.

We discretize the forcing term $\vec{f}\left(\vec{X},t\right)\delta\left(\vec{x}-\vec{X}\right)$ as $\vec{F}\left(\vec{x},t\right)$, where $\vec{F}\left(\vec{x},t\right)=\left[\,F_x\,F_y\,F_z\,\right]^{T}$ is the body force acted on the fluid by the cilium. The relation between $\vec{F}\left(\vec{x},t\right)$ and $\vec{f}\left(\vec{X},t\right)$ is given by

$$\vec{F}\left(\vec{x},t\right)=\sum_{m=1}^{N}\vec{f}_m\left(\vec{X},t\right)\hat{\delta}\left(\vec{x}-\vec{X}_m\left(s,t\right)\right), \quad (3.3)$$

where N is the number of points making up the cilium. The delta function $\delta\left(\vec{x}-\vec{X}\right)$ in (3.1) is approximated as $\hat{\delta}\left(\vec{x}-\vec{X}\right)$, where $\hat{\delta}\left(\vec{x}-\vec{X}\right)$ takes the form

$$\hat{\delta}\left(\vec{x}-\vec{X}\left(s,t\right)\right)=\begin{cases}\prod_{i=1}^{3}\frac{1}{4h}\left[1-\cos\left(\frac{\left(x_i-X_i\left(s,t\right)\right)\pi}{2h}\right)\right] & \text{for } 0\le\left\|\vec{x}_i-\vec{X}_i\left(s,t\right)\right\|\le 2h \\ 0 & \text{for } 2h<\left\|\vec{x}_i-\vec{X}_i\left(s,t\right)\right\| \end{cases},$$

(3.4)

h is the distance between fluid grid points, and i represents the three principal orthogonal directions in Cartesian coordinates.

Both the non-linear convective term $\left(\vec{u}\cdot\vec{\nabla}\right)\vec{u}$ and the body force terms $\vec{F}\left(\vec{x},t\right)$ and $\vec{F}_\sigma\left(\vec{x},t\right)$ are treated explicitly and discretized using the second-order Adam-Bashforth method. The linear viscous term $\vec{\nabla}\left(\upsilon\vec{\nabla}\cdot\vec{u}\right)$ is discretized using the Crank-Nicholson method. In our implementation, the pressure lags by half a time step. The time-discrretized momentum equation is thus

$$\frac{\vec{u}^*-\vec{u}^n}{\Delta t}+\frac{3}{2}\left(\left(\vec{u}\cdot\vec{\nabla}\right)\vec{u}\right)^n-\frac{1}{2}\left(\left(\vec{u}\cdot\vec{\nabla}\right)\vec{u}\right)^{n-1}=$$
$$-\left(\frac{1}{\rho}\vec{\nabla}p\right)^{n-1/2}+\frac{1}{2}\vec{\nabla}\left[\upsilon\left(\vec{\nabla}\cdot\vec{u}\right)^*+\upsilon\left(\vec{\nabla}\cdot\vec{u}\right)^n\right]+\left[\frac{3}{2}\left(\frac{1}{\rho}\vec{F}\left(\vec{x},t\right)\right)^n-\frac{1}{2}\left(\frac{1}{\rho}\vec{F}\left(\vec{x},t\right)\right)^{n-1}\right]+\cdot$$
$$\left[\frac{3}{2}\left(\frac{1}{\rho}\vec{F}_\sigma\left(\vec{x},t\right)\right)^n-\frac{1}{2}\left(\frac{1}{\rho}\vec{F}_\sigma\left(\vec{x},t\right)\right)^{n-1}\right]$$

(3.5)

We shall now briefly discuss the spatial discretizations. The variables in the Navier-Stokes equations are solved using a finite-difference method on a staggered Cartesian grid. The staggered grid is otherwise known as a marker-

and-cell (MAC) grid [108]. The velocity component u is staggered by a half grid spacing in the y and z directions, v is staggered by a half grid spacing in the x and z directions and w is staggered by a half grid spacing in the x and y directions. p is defined at cell centers and $\vec{F}$ is defined at grid points. Quantities are solved at their respective staggered locations. A 2D version of this grid is shown in Figure 3.2.

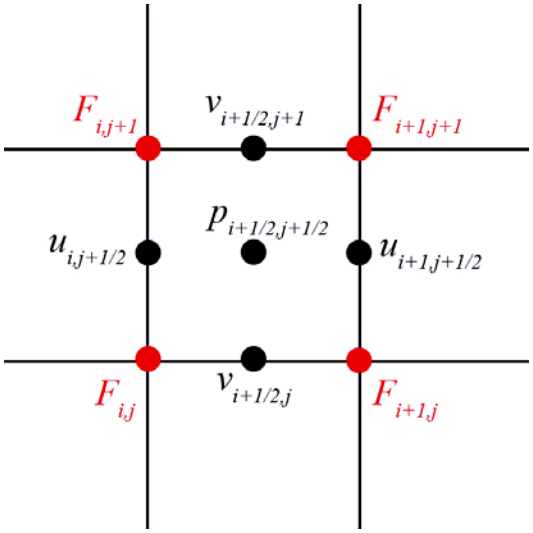

Figure 3.2 Depiction of location of fluid variables on a staggered grid is shown. This grid is also known as a marker-and-cell (MAC) grid. Velocities (u,v) are defined at locations staggered by half grid spacing, pressure p is defined at cell centers and the fluid body force F is defined at grid points.

The spatial derivatives in the viscous linear term $\vec{\nabla}\left(\upsilon\vec{\nabla}\cdot\vec{u}\right)$ are discretized using a second-order central difference scheme. Here, we present only the discretized derivatives involving u in the x-direction:

$$\frac{\partial}{\partial x}\left(\upsilon\frac{\partial u}{\partial x}\right)\Bigg|_{i,j+1/2,k+1/2}^{n} = \begin{pmatrix} u_{i+1,j+1/2,k+1/2}^{n}\upsilon_{i+1,j+1/2,k+1/2}^{n} \\ -u_{i,j+1/2,k+1/2}^{n}\left(\upsilon_{i+1,j+1/2,k+1/2}^{n}+\upsilon_{i-1,j+1/2,k+1/2}^{n}\right) \\ +u_{i-1,j+1/2,k+1/2}^{n}\upsilon_{i-1,j+1/2,k+1/2}^{n} \end{pmatrix} / \Delta x^{2} \ . \qquad (3.6)$$

Here, superscript n denotes variables at the nth time step and subscripts i, j and k represent the indices corresponding to the fluid grid points. The viscous

terms $\upsilon^n_{i+1,j+1/2,k+1/2}$ and $\upsilon^n_{i-1,j+1/2,k+1/2}$ are required at locations where υ is not defined, therefore $\upsilon^n_{i+1,j+1/2,k+1/2}$ and $\upsilon^n_{i-1,j+1/2,k+1/2}$ are obtained through simple linear interpolation.

Similarly, first order spatial derivatives from the non-linear convective term $\left(\vec{u}\cdot\vec{\nabla}\right)\vec{u}$ are discretized using a second-order central difference scheme. We present only the derivatives in the momentum equation in the x direction:

$$\left(u\frac{\partial u}{\partial x}\right)^n\Bigg|_{i,j+1/2,k+1/2} = u^n_{i,j+1/2,k+1/2}\frac{u^n_{i+1,j+1/2,k+1/2}-u^n_{i-1,j+1/2,k+1/2}}{2\Delta x}, \tag{3.9}$$

$$\left(v\frac{\partial u}{\partial y}\right)^n\Bigg|_{i,j+1/2,k+1/2} = v^n_{i,j+1/2,k+1/2}\frac{u^n_{i,j+3/2,k+1/2}-u^n_{i,j-1/2,k+1/2}}{2\Delta y}, \tag{3.10}$$

$$\left(w\frac{\partial u}{\partial z}\right)^n\Bigg|_{i,j+1/2,k+1/2} = w^n_{i,j+1/2,k+1/2}\frac{u^n_{i,j+1/2,k+3/2}-u^n_{i,j+1/2,k-1/2}}{2\Delta z}. \tag{3.11}$$

Again, the terms $v^n_{i,j+1/2,k+1/2}$ and $w^n_{i,j+1/2,k+1/2}$ are required at locations where v and w are not defined, and are therefore obtained through simple linear interpolations.

The pressure in our implementation is evaluated at the $\left(n-1/2\right)^{\text{th}}$ time step. Since pressure variables are defined at cell centres and pressure derivatives are often needed at the staggered velocity grid points, the pressure derivatives in the momentum equations are discretized as

$$\frac{\partial p^{n-1/2}}{\partial x}\Bigg|_{i,j+1/2,k+1/2} = \frac{p^{n-1/2}_{i+1/2,j+1/2,k+1/2}-p^{n-1/2}_{i-1/2,j+1/2,k+1/2}}{\Delta x}, \tag{3.12}$$

$$\frac{\partial p^{n-1/2}}{\partial y}\Bigg|_{i+1/2,j,k+1/2} = \frac{p^{n-1/2}_{i+1/2,j+1/2,k+1/2}-p^{n-1/2}_{i+1/2,j-1/2,k+1/2}}{\Delta y}, \tag{3.13}$$

$$\frac{\partial p^{n-1/2}}{\partial z}\Bigg|_{i+1/2,j+1/2,k} = \frac{p^{n-1/2}_{i+1/2,j+1/2,k+1/2}-p^{n-1/2}_{i+1/2,j+1/2,k-1/2}}{\Delta z}. \tag{3.14}$$

Note that our discretizations are all second-order accurate in space and time.

We use the projection method to solve the Navier-Stokes equations. An intermediate velocity $\vec{u}^*$ is first solved at time n. Next, the pressure is used to impose the incompressibility condition. Finally the velocities are corrected to their divergence-free values at time $n+1$. It can be seen from (3.5) that $\vec{u}^*$ is present in both the time derivative $\frac{\partial \vec{u}}{\partial t}$ and the linear viscous term $\vec{\nabla}\left(\upsilon\vec{\nabla}\cdot\vec{u}\right)$. Rearranging the momentum equation (3.5), we obtain

$$\begin{aligned}
&\frac{\vec{u}^*}{\Delta t}-\frac{1}{2}\vec{\nabla}\left(\upsilon\vec{\nabla}\cdot\vec{u}^*\right)=-\frac{1}{\rho}\left(\vec{\nabla}p\right)^{n-1/2}-\frac{3}{2}\left(\left(\vec{u}\cdot\vec{\nabla}\right)\vec{u}\right)^n+\frac{1}{2}\left(\left(\vec{u}\cdot\vec{\nabla}\right)\vec{u}\right)^{n-1}\\
&+\frac{1}{2}\vec{\nabla}\left(\upsilon\vec{\nabla}\cdot\vec{u}\right)^n+\left[\frac{3}{2}\left(\frac{1}{\rho}\vec{F}\left(\vec{x},t\right)\right)^n-\frac{1}{2}\left(\frac{1}{\rho}\vec{F}\left(\vec{x},t\right)\right)^{n-1}\right]+\\
&+\left[\frac{3}{2}\left(\frac{1}{\rho}\vec{F}_\sigma\left(\vec{x},t\right)\right)^n-\frac{1}{2}\left(\frac{1}{\rho}\vec{F}_\sigma\left(\vec{x},t\right)\right)^{n-1}\right]+\frac{\vec{u}^n}{\Delta t}
\end{aligned} \quad . \quad (3.15)$$

It can be seen that the above equation for $\vec{u}^*$ can be cast as a Helmholtz equation which we can then solve implicitly.

After obtaining $\vec{u}^*$, we solve for a pressure correction φ using

$$\frac{\vec{u}^{n+1}-\vec{u}^*}{\Delta t}=-\frac{1}{\rho}\vec{\nabla}\varphi \ . \quad (3.16)$$

Taking $\vec{\nabla}$ on both sides, we obtain

$$\frac{\vec{\nabla}\cdot\vec{u}^{n+1}-\vec{\nabla}\cdot\vec{u}^*}{\Delta t}=-\vec{\nabla}\left(\frac{1}{\rho}\vec{\nabla}\varphi\right). \quad (3.17)$$

Imposing the incompressibility condition by setting $\vec{\nabla} \cdot \vec{u}^{n+1} = 0$, we obtain

$$\frac{\vec{\nabla} \cdot \vec{u}^*}{\Delta t} = \vec{\nabla}\left(\frac{1}{\rho} \vec{\nabla} \varphi \right). \tag{3.18}$$

The above forms a Poisson equation. In a similar fashion to the Helmholtz equation, this Poissson equation is solved implicitly for φ. Since the matrices formed by both the Helmholtz and Poisson equations are symmetric, they can be solved using the preconditioned conjugate method. Solving of these equations are parallelized using MPI in C and solved using the HYPRE [109] library.

In using the HYPRE library, we need only to specify coefficients for the difference equations, i.e. the discretized form of the Helmholtz and Poisson equations. Matrix assembly and solving were then performed by calling the appropriate HYPRE functions.

After solving for φ, we advance the velocities to the $(n+1)^{\text{th}}$ time step using

$$\vec{u}^{n+1} = \vec{u}^* - \Delta t \left(\frac{1}{\rho} \vec{\nabla} \varphi \right). \tag{3.19}$$

Next, we advance p^n to the $(n+1/2)^{\text{th}}$ time step using the equation

$$p^{n+1/2} = p^{n-1/2} + \varphi - \frac{\Delta t}{2} \left(\vec{\nabla} \cdot \vec{u}^* \right). \tag{3.20}$$

We have now obtained the velocities at the $(n+1)^{\text{th}}$ time step and the pressure at the $(n+1/2)^{\text{th}}$ time step. This concludes the advancement of the discretized Navier-Stokes equations by one time step.

3.2 Implementation of stratified two-layered fluid arrangement

In simulations where two different fluids are present, the second fluid sits above the first fluid, effectively forming a stratified fluid arrangement (Figure 3.1). We now require the location of the interface. To solve the location of the interface, we use a conservative form of the level set method described by Olsson and Kreiss [110].

In our implementation, the level set function is denoted by a scalar Φ, where $0 \le \Phi \le 1$. This is unlike the standard level set functions where Φ is the scalar distance to the interface (Sussman et al. [111]). Our choice of level set function allows fluid material properties ρ and υ at any location $\vec{x}$ to be easily calculated as

$$\upsilon = (1-\Phi)\upsilon_1 + \Phi\upsilon_2, \tag{3.21}$$

$$\rho = (1-\Phi)\rho_1 + \Phi\rho_2, \tag{3.22}$$

where ρ_1 and ρ_2 represent the densities of the two fluids respectively, and υ_1 and υ_2 represent the kinematic viscosities of the two fluids respectively.

The level set field function Φ is convected using the equation

$$\frac{\partial \Phi}{\partial t} + \vec{\nabla}(\Phi\vec{u}) = 0. \tag{3.23}$$

It should be noted that the above equation is hyperbolic; therefore in order to ensure stability of our explicit time-marching scheme, the convective term $\vec{\nabla}(\Phi\vec{u})$ is implemented using a TVD scheme with Superbee limiter. This implementation is fully described in [110].

The Superbee limiter, however, has been shown to be insufficient to maintain the interface thickness over repeated time evolution. Hence, as in [110], we implement an intermediate step to ensure a constant profile and thickness of the interface. The intermediate step requires solving the equation

$$\frac{\partial \Phi}{\partial \tau} + \vec{\nabla} \cdot \left(\vec{g} - \varepsilon_0 \vec{\nabla} \Phi \right) = 0, \tag{3.24}$$

where $\vec{g} = \Phi(1-\Phi)\hat{n}$. The normal at the interface $\hat{n}$ is given by

$$\hat{n} = \frac{\nabla \Phi}{|\nabla \Phi|}. \tag{3.25}$$

Equation 3.24 is solved to steady state by time-stepping through artificial time τ. This solving process takes place within each physical time step Δt. In our implementation, we set $\Delta \tau = \Delta t / 10$. At steady state, the level set function at the interface will be smoothly spread across a thickness proportional to ε_0. A typical interface thickness from our simulations is shown in Figure 3.3.

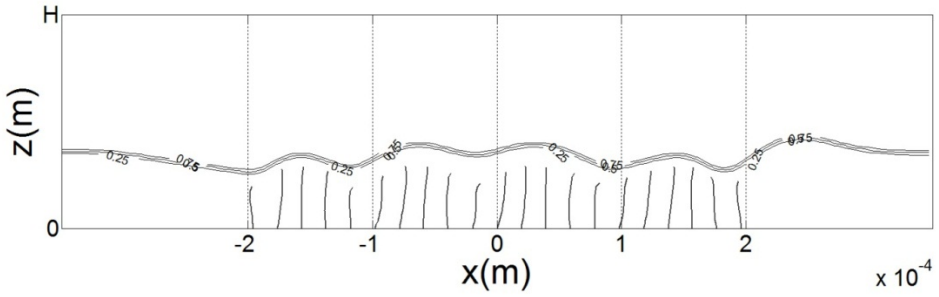

Figure 3.3 The interface thickness in a stratified, two-fluid arrangement is shown. The simulation conditions are $\sigma = 0.0025 Nm^{-1}$ and $\mu_2 / \mu_1 = 6$ at $t = 0.3s$.

Time integration is carried out using a second-order Runge-Kutta scheme, namely

$$\begin{aligned}
\vec{\Phi}^{*} &= \vec{\Phi}^{n} + \Delta\tau F_n\left(\vec{\Phi}^{n}\right), \\
\vec{\Phi}^{**} &= \vec{\Phi}^{*} + \Delta\tau F_n\left(\vec{\Phi}^{*}\right), \\
\vec{\Phi}^{n+1} &= \frac{1}{2}\left(\vec{\Phi}^{n} + \vec{\Phi}^{**}\right),
\end{aligned} \tag{3.26}$$

while spatial derivatives are implemented using our standard second-order central-difference finite difference schemes. We find that within each time physical time step Δt , only about ~5 iterations are needed to reach convergence.

We note that although there are faster, more advanced time marching-schemes developed for the evolution of level set functions [112-113], the bottleneck in our computational scheme lies in the solving of the Poisson equation for the pressure. Here, the convergence rate of the solution appears to be slowest among all our schemes; therefore any improvement in the time-marching scheme of our level set implementation is expected to bring only marginal benefits to our overall algorithm. The simple, second-order Runge-Kutta schemes implemented here are therefore sufficient for our needs.

Finally, we implement the surface tension as a body force. This body force is calculated as

$$\vec{F}_{\sigma}\left(\vec{x},t\right) = \sigma\left(-\vec{\nabla}\cdot\frac{\vec{\nabla}\Phi}{\left|\vec{\nabla}\Phi\right|}\right)\vec{\nabla}\Phi\ . \tag{3.27}$$

This body force enters into the momentum equation 3.1. In our numerical implementation, it is treated explicitly using the Adam-Bashforth method (equations 3.5 and 3.15).

3.3 Implementation of cilia using a rod-and-spring model

In our model, the cilium is assumed to be neutrally buoyant and massless. The cilium is modelled using a rod-and-spring model (Figure 3.1). Due to the nature of the IBM, the fluid grid points and the flagellum points need not coincide. Linear elastic springs imposed between the cilium points provide resistance to stretching and torsion springs imposed at each cilium point provide resistance to bending.

The force $\vec{f}\left(\vec{X},t\right)$ at each cilium point is calculated as

$$\vec{f} = \vec{f}_{elastic} + \vec{f}_{moment} + \vec{f}_{active}, \tag{3.28}$$

where $\vec{f}_{elastic}$ is the force from a linear spring given as

$$\begin{aligned}\vec{f}_{elastic}(\vec{X}_i,t) = &-k\left(\left\|\vec{X}_{i+1}-\vec{X}_i\right\|-\Delta s_0\right)\frac{\vec{X}_i-\vec{X}_{i+1}}{\left\|\vec{X}_i-\vec{X}_{i+1}\right\|} \\ &-k\left(\left\|\vec{X}_{i-1}-\vec{X}_i\right\|-\Delta s_0\right)\frac{\vec{X}_i-\vec{X}_{i-1}}{\left\|\vec{X}_i-\vec{X}_{i-1}\right\|}\end{aligned}. \tag{3.29}$$

Here k is a spring constant and Δs_0 is the rest length of the linear elastic spring connecting two adjacent points.

$\vec{f}_{moment}$ is the force at each discretized cilium point arising from moments in the cilium. $\vec{f}_{moment}$ at each cilium point can be calculated as

$$\begin{aligned}\vec{f}_{moment}\left(\vec{X}_i,t\right) = &-\frac{\vec{X}_{i+1}-\vec{X}_i}{\left\|\vec{X}_i-\vec{X}_{i+1}\right\|^2}\times\vec{M}_{i+1}+\frac{\vec{X}_{i-1}-\vec{X}_i}{\left\|\vec{X}_i-\vec{X}_{i-1}\right\|^2}\times\vec{M}_{i-1} \\ &+\frac{\vec{X}_{i+1}-\vec{X}_i}{\left\|\vec{X}_i-\vec{X}_{i+1}\right\|^2}\times\vec{M}_i-\frac{\vec{X}_{i-1}-\vec{X}_i}{\left\|\vec{X}_i-\vec{X}_{i-1}\right\|^2}\times\vec{M}_i\end{aligned}, \tag{3.30}$$

where $\vec{M}$ is the moment at each cilium point. $\vec{M}$ is calculated as

$$\vec{M} = -T_\theta \left(\vec{\theta} - \vec{\theta}_0 \right), \tag{3.31}$$

where T_θ is a torsional spring constant. This torsional restoring force arises when adjacent cilium points form angular deviations from $\vec{\theta}_0$, which is the rest angle defined between the points. In our simulations, each cilium is modelled as a straight beam, therefore $\theta_0 = 0$.

In the regime where k is stiff, the rod-and-spring model can be used to represent an Euler-Bernoulli beam where the bending modulus EI is obtained as

$$EI = T_\theta \Delta s_0, \tag{3.32}$$

where Δs_0 is the distance between discretized points on the beam. In our simulations, k is stiff enough such that cilium stretch is negligible.

Explicit modeling of the geometric clutch mechanism was implemented by Dillon et al. [86], Yang et al. [87] and Elgeti and Gompper [88]. These implementations require resolution of the internal micro-tubules making up the cilia. In our immersed boundary implementation, this would require our fluid grid size to be prohibitively small. In addition to that, the small time-step size required for a fine grid makes the simulations uneconomical to run. Therefore, we instead use a minimalist model where the active forces are represented as simple triangular loadings on the cilia and the switching mechanism is the energy expanded by the cilia. This energy can be thought to represent the energy expanded by the dynein motors during each beat cycle.

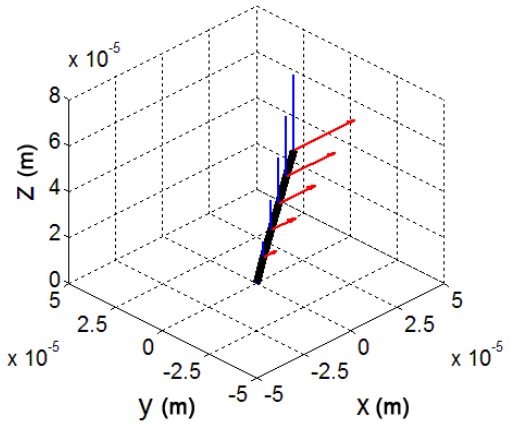

(a)

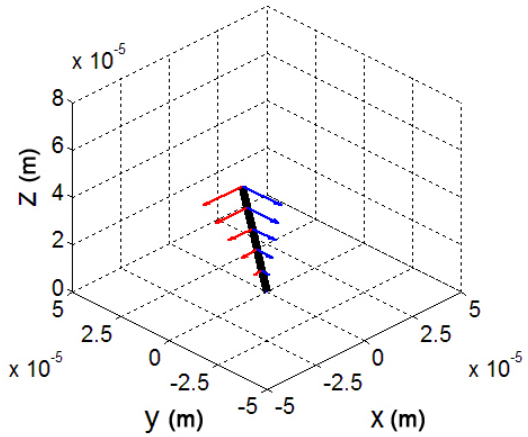

(b)

Figure 3.4 (a) Forces of the forward stroke $\vec{f}_{forward}$ are shown. Triangular loads are applied in the positive x-direction (red arrows) and in the positive z-direction (blue arrows). (b) Forces of the reverse stroke $\vec{f}_{reverse}$ are shown. Triangular loads are applied in the negative x-direction (red arrows) and in the negative y-direction (blue arrows).

In our minimalist model, the cilium is driven by an active force $\vec{f}_{active}$. $\vec{f}_{active}$ is applied in two distinct steps corresponding to the forward and reverse strokes of the cilium. The length and velocity scales in our simulations are small; therefore we can assume that the flow generated by the cilia happens at very low Reynolds numbers. Purcell [34] has shown that reciprocal movements at zero Reynolds numbers cannot produce a net fluid flux. In order to observe a

net fluid flux, we therefore design the forward stroke of our cilia to be different from the reverse stroke. Also, we design our cilia to undergo large, non-linear deformations. This causes the fluid flow to be non-reversible.

The forward stroke, $\vec{f}_{forward}$, is therefore implemented as a distributed triangle load along the cilium in the positive *x*- and *z*-directions, while the reverse stroke $\vec{f}_{reverse}$, is implemented as a distributed triangle load in the negative *x*- and *y*-directions. The forward stroke force vectors are shown in Figure 3.4(a) while the reverse stroke force vectors are shown in Figure 3.4(b). The difference in application of forces between the forward and reverse strokes ensures our cilia movement is not reciprocal.

Thus, at each cilium control point, $\vec{f}_{forward}$ and $\vec{f}_{reverse}$ can be represented as

$$\vec{f}_{forward}\left(\vec{X},t\right)= f_0\left(\vec{X},t\right)\left(\vec{i}+\alpha\vec{k}\right)\Delta s, \tag{3.33}$$

$$\vec{f}_{reverse}\left(\vec{X},t\right)=-f_0\left(\vec{X},t\right)\left(\vec{i}+\beta\vec{j}\right)\Delta s, \tag{3.34}$$

where

$$f_0\left(\vec{X}\left(s,t\right),t\right)=P_0 s\,. \tag{3.35}$$

P_0 is a force per unit area and f_0 is a force per unit length that determines the strength of the active force. α and β are parameters used to modify the cilium motion in the forward and reverse strokes. In our simulations, we choose $\alpha=4$ and $\beta=2$. α can be attributed to dynein activity confining the cilium beat to a single plane during its forward stroke, while β can be attributed to dynein activity causing a sideways sweep of the cilium during its reverse stroke.

Our linear, triangular force loading is utilized for simplicity and convenience. A wide range of force models have been adopted in other studies. For example, in cases where the cilium is simplified as a single bead [90], the force is modelled as a point force. In the case of Alexeev [44] where the

cilium is a 3D structure, the force is a point force acting on the cilium tip. In the case of Khaderi et al. [45] and Khaderi and Onck [46], the force distribution is determined by an external magnetic field. In the case of Gueron and Levit-Gurevich [85] and Dillon et al. [86], realistic forces are used by virtue of modeling the internal mechanisms of the cilium.

The energy expanded by the cilium as it transverses the $x-$direction is given by

$$E(t)=\iint\begin{bmatrix}u\\0\\0\end{bmatrix}\cdot\frac{\partial\vec{f}_{active}}{\partial s}dsdt\,, \tag{3.36}$$

In order to determine if the cilium is in the forward or reverse stroke, we apply the following criteria

$$\vec{f}_{active}\left(\vec{X},t\right)=\begin{cases}\vec{f}_{forward}\left(\vec{X},t\right) & \text{if E(t)}=E_0 \text{ and cilium is in reverse stroke}\\ \vec{f}_{reverse}\left(\vec{X},t\right) & \text{if E(t)}=E_0 \text{ and cilium is in forward stroke}\end{cases}, \tag{3.37}$$

where E_0 is a predefined energy level. As stated in Section 2.3, Gueron and Levit-Gurevich [85] found that the energy expanded by cilia in fluids with viscosities in the range of $\mu_{water}<\mu<5\mu_{water}$ appear to have little variation. It therefore seems plausible to use a fixed value of energy as the switching mechanism.

Equations 3.36 and 3.37 can be interpreted as a mechanism whereby each cilium switches from a forward to reverse stroke when the forward stroke has expanded energy E_0, and subsequently switches from a reverse stroke to a forward stroke when the cilium has expanded energy E_0. Using a constant level of energy as a switch gives the advantage of allowing the fluid flow rates to be a direct indication of propulsive efficiency of the cilia.

For convenience, E_0 is chosen to be the same for both the forward and reverse strokes.

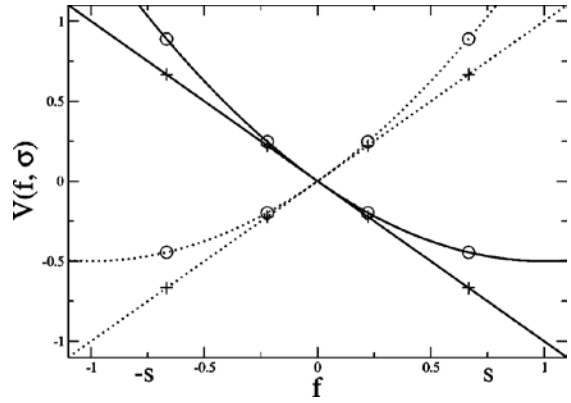

(a)

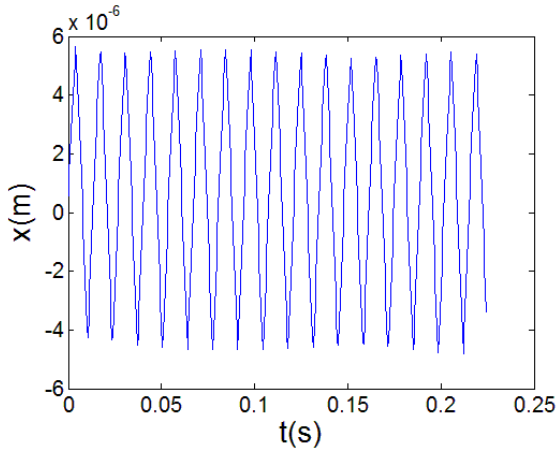

(b)

Figure 3.5 (a) In [90], a simple switching mechanism based on displacement ($\pm s$) is used. The relationship between potential energy $V(\mathrm{f},\sigma)$ of a cilium with reference to its position f is shown. (b). The displacement of our cilium tip with energy as the switching mechanism is shown. It can be seen that the cilium switches between forward and reverse strokes when its tip reaches positions that are fairly constant throughout its beat cycle.

In [90], the authors used a model where each cilium is simplified as a discrete bead. The non-linear switching mechanism was implemented as fixed positions of the cilium, i.e. as the cilium travels linearly along displacement f, it encounters switching position points located at $\pm s$ (Figure 3.5(a)). The cilium then switches between its forward and reverse strokes accordingly. The

authors also defined a potential $V(\mathrm{f},\sigma)$ for each cilium, where $\sigma = \pm 1$ is a parameter that determines the stroke the cilium is in (to be consistent with [90], only here do we use s to denote switching position and σ to denote the switching mechanism. In the rest of this thesis, s is used to denote Lagrangian coordinate along the cilium and σ is used to denote surface tension between the fluid interfaces). The active force on the cilium is hence $\partial V(\mathrm{f},\sigma)/\partial \mathrm{f}$. The authors investigated two forms of $V(\mathrm{f},\sigma)$: a linear form and a quadratic form. The linear form of $V(\mathrm{f},\sigma)$ exerts a constant force on the cilium throughout the cilium motion, while the quadratic form of $V(\mathrm{f},\sigma)$ exerts a decreasing force on the cilium as it approaches the switching points. Since the potential is now well-defined with respect to the switching mechanism, it is thus a small extension to substitute the potential (i.e. energy) as the switching mechanism.

We find that substituting the energy in place of position for the switch does not drastically vary the dynamics of the cilium. We show this by conducting a simulation of a single cilium in a flow chamber. This simulation is performed with parameters as shown in Table 3.1. This cilium is located at $(0,0)$ in the flow chamber. The displacement of the cilium tip parallel to the forward stroke is shown in Figure 3.5(b). It can be seen that, despite using energy as a switch, the cilium switches between its forward and reverse strokes when its tip reaches positions that are fairly constant throughout its beat cycle. We therefore believe that substituting the energy for the switch does not change the dynamics of our model drastically compared to the case where position is used as the switch.

Since $\vec{f}_{elastic}$, $\vec{f}_{moment}$ and $\vec{f}_{active}$ are now known, $\vec{f}\left(\vec{X},t\right)$, which exist on the cilium control points, can then be transferred to the fluid grid. Subsequently, the Navier-Stokes equations can now be solved. Solving the Navier-Stokes equations provides us with the fluid velocities and pressure. The velocities are then used to advect the cilium points.

The cilium points are advected by interpolating velocities from the fluid grid using

$$\left(\frac{\partial \vec{X}_m(s,t)}{\partial t}\right)^{n+1} = \sum_{r=1}^{N_z}\sum_{q=1}^{N_y}\sum_{p=1}^{N_x} \vec{u}_{p,q,r}(x,t)\hat{\delta}\left(\vec{x}_{p,q,r} - \vec{X}_m(s,t)\right), \qquad (3.38)$$

where $\left(\frac{\partial \vec{X}_m(s,t)}{\partial t}\right)^{n+1}$ is the velocity of each cilium grid point at time $n+1$. The positions of the cilium points are next updated using

$$\vec{X}^{n+1}(s,t) = \frac{1}{2}\left[\left(\frac{\partial \vec{X}(s,t)}{\partial t}\right)^{n+1} + \left(\frac{\partial \vec{X}(s,t)}{\partial t}\right)^{n}\right]\Delta t + \vec{X}^{n}(s,t)\ , \qquad (3.39)$$

It should be noted that by imposing the active force $\vec{f}_{active}$, the cilium obtains an intrinsic amplitude and frequency. This amplitude and frequency are dependent upon the stiffness of the cilium and its interaction with surrounding cilia and fluid.

The IBM can thus be summarized is as follows: assuming the fluid velocity $\vec{u}^n$ and the position of the cilium $\vec{X}^n$ at time step n are known, the IBM advances the system by Δt using the following procedure:

1. Calculate $\vec{f}\left(\vec{X},t\right)$ on the cilium due to its present position $\vec{X}^n(s,t)$ using equations 3.28, 3.29, 3.30 and 3.37.
2. Spread the force $\vec{f}\left(\vec{X},t\right)$ to the fluid grid points to obtain $\vec{F}(x,t)$ at all fluid grid points using equations 3.3 and 3.4.
3. Calculate the body force acting on the fluid due to surface tension forces using equation 3.27.
4. Obtain scalar fluid material properties υ and ρ from level set function Φ using equations 3.21 and 3.22.

5. Solve the Helmholtz form of the momentum equation 3.15 to obtain the intermediate velocities $\vec{u}^*$
6. Solve the Poisson form of the pressure correction equation 3.18, for the pressure correction φ.
7. Update $\vec{u}^*$ to $\vec{u}^{n+1}$ using equation 3.19.
8. Update $p^{n-1/2}$ to $p^{n+1/2}$ using equation 3.20.
9. Solve equation 3.23 for level set function Φ.
10. Maintain the interface thickness using equation 3.24.
11. Interpolate the fluid velocities to the cilium using equation 3.38 to obtain the velocity of the cilium control points.
12. Advance the positions of the cilium control points using equation 3.39.
13. Repeat from 1.

3.4 Discussion of parameters used in simulations

In our simulations, we set cilia length $L = 4.9 \times 10^{-5} m$. Our value of L is one order of magnitude larger compared to that of natural cilia ($4\mu m - 6\mu m$). This larger value of L is used because of a limitation of the projection method. In the projection method, the time-stepping mechanism is utilized to impose the incompressibility condition; therefore time-stepping cannot be avoided. Since the time-scale of our simulation is proportional to Reynolds number, extremely small time steps are required when Reynolds number is low. By increasing the value of L by one order of magnitude, we increase the Reynolds number. This increase in Reynolds number allows us to increase our time-step size while still keeping our simulations in the low Reynolds number regime, therefore reducing our computational costs.

Besides increasing the Reynolds number, our problem of small time-steps is further mitigated by use of parallelized algorithms. We are thus able to simulate a reasonable number of cilia beats in a reasonable time.

We note that the lengths of artificial cilia are typically longer than that of natural cilia. For example, Shields et al. [28] fabricated cilia of lengths $10\mu m - 25\mu m$. Khaderi and Onck [46] simulated cilia of length $100\mu m$. Oh et al. [32-33] and Kongthon et al. [35-37] fabricated cilia of lengths $800\mu m$. Our cilia length therefore lies within this relevant range.

In our simulations, we neglect both the mass of the cilium and density differences between the upper and lower fluids (i.e. we set $\rho_2 = \rho_1 = 1000 kgm^{-3}$). We justify this by showing that, (1) the gravitational force due to differences in density are negligible compared to the surface tension force, (2) the inertia of the cilium is negligible compared to the active force, (3) the inertia of the fluid is negligible compared to the active force, and (4) the density of mucus is expected to be similar to that of water.

In our simulations, assuming a characteristic length of cilia $L = 5\times10^{-5} m$, a characteristic density difference of $\Delta\rho \sim 1000 kgm^{-3}$, a characteristic surface tension of $\sigma \sim 0.01 Nm^{-1}$ and $g = 9.81 ms^{-2}$, an order of magnitude estimate of the Bond number is $Bo = \frac{L^2 \rho g}{\sigma} \sim 2.45\times10^{-3}$. The Bond number is a measure of the gravitational force relative to the surface tension force. Since the Bond number is expected to be small, the effects of gravity on density differences between the upper and lower fluids can be expected to be negligible.

Also, assuming a characteristic cilium length as $L = 5\times10^{-5} m$, the characteristic volume of the cilium is therefore $L^3 = 1.25\times10^{-13} m^3$. Assuming a time scale of $T \sim 0.025 s$ (frequency of $40 Hz$), a characteristic acceleration is $a = L/T^2 \sim 8\times10^{-2} ms^{-2}$. Assuming $\rho = 1000 kgm^{-3}$, we therefore obtain an equivalent inertial force of the cilium as $ma = \rho V a \sim 1\times10^{-11} N$. This inertial term is about 2 orders of magnitude smaller than the $1000 pN$ force a microtubule pair typically exerts [114]. Hence, the cilium active force is balanced mostly by the fluid's viscous force, therefore the inertial effects of

the cilium should be negligible. We therefore exclude inertial effects of the cilium in our simulations.

Using the argument above, we can also reasonably state that the volume of fluid moved per cilium is also on the order of $\sim L^3$, and, given similar densities and accelerations, inertial effects of the fluid are similarly negligible. We can therefore justifiably exclude effects of density differences between the upper and lower fluids.

In addition, since ~95% of mucus is known to consist of water [115, 116], we can expect the density of mucus to be $\sim 1000 kgm^{-3}$. We therefore set $\rho_2 = \rho_1 = 1000 kgm^{-3}$ in all our simulations. In addition, since the lower fluid is approximated to be similar to water, we set $\mu_1 = 1 \times 10^{-3} kgm^{-1} s^{-1}$.

In our simulations, the force distribution along the cilium length P_0 is chosen such that the total force acting on the cilium is $P_0 \int sds = 0.95 \times 10^{-9} N$. This force approximates the force exerted by a microtubule pair [114].

The stiffness of cilia has been shown to take on a wide range of values. For example, Okuno and Hiramoto [117] reported the stiffness of microtubule pairs to be in the range of $0.3 \times 10^{-21} - 1.1 \times 10^{-20} Nm^2$. This range of stiffness spans 2 orders of magnitude. Given this large uncertainty, we therefore chose our cilium stiffness to cover the range of $6.90 \times 10^{-23} Nm^2 - 1.38 \times 10^{-18} Nm^2$.

Our value of E_0 is chosen to approximate physical values. For example, in the case of Mukundan et al. [114], the characteristic force generated in a filament pair is $\sim 1000 pN$. Given that a cilium is typically $\sim 5 \mu m$ long, the characteristic energy per cilium can therefore be approximated as $9 \times 1000 pN \times 5 \mu m \sim 4.5 \times 10^{-14} J$. Our value of E_0 is therefore chosen to be $E_0 = 4.863 \times 10^{-14} J$.

The surface tensions of common fluids are typically $\sigma \sim 0.01 Nm^{-1} - 0.07 Nm^{-1}$ [118]. Lee et al. [50] used a range of $\sigma \sim 1\times10^{-7} Nm^{-1} - 10 Nm^{-1}$ to simulate the surface tension between mucus and periciliary layer (PCL). In our simulations, we use a range of $\sigma = 0 Nm^{-1} - 0.02 Nm^{-1}$. Although our range of σ is narrower than that listed by Deng et al. and Lee et al., we shall show in Chapter 7, that, for $\sigma > 0.02 Nm^{-1}$, there is negligible deformation of the interface; hence higher values of σ is expected to have negligible effects on the dynamics of our simulations.

The parameters used for our simulations are summarized in Table 3.1.

	Description	**Symbol**	**Units**	**Value**
Cilia parameters	Cilia length	L	m	4.91×10^{-5}
	Cilia bending stiffness	EI	Nm^{2}	6.90×10^{-23} - 1.38×10^{-18}
	Cilia stretching stiffness	k	Nm^{-1}	1.2×10^{-2}
	Energy expanded by cilia per stroke	E_0	J	4.863×10^{-14}
	Active force parameter	P_o	Nm^{-2}	7.9×10^{-1}
	Cilia number density	d^{-2}	m^{-2}	1.15×10^{9} - 4.06×10^{9}
Fluid parameters	Density of lower fluid	ρ_1	kgm^{-3}	1000
	Density of upper fluid	ρ_2	kgm^{-3}	1000
	Dynamic viscosity of lower fluid	μ_1	$kgm^{-1}s^{-1}$	1.0×10^{-3}
	Dynamic viscosity of upper fluid	μ_2	$kgm^{-1}s^{-1}$	1.0×10^{-3} - 6.0×10^{-3}
	Surface tension at fluid interface	σ	Nm^{-1}	0.00 – 0.02
Fluid domain dimensions	Chamber length	L_Ω	m	7×10^{-4}
	Chamber width	W_Ω	m	7×10^{-4}
	Chamber height	H_Ω	m	1.72×10^{-4}
Numerical parameters	Number of cilium control points	N_c	-	6 - 14
	Time step size	Δt	s	1.25×10^{-6} - 5.0×10^{-6}
	Fluid grid size	h	m	4.40×10^{-6} - 2.9×10^{-6}

Table 3.1 This table summarizes the parameters used for our cilia simulations.

4 Validation and benchmarking of IBM code

4.1 Validation of fluid solver using the case of a lid-driven cavity

We first validate our numerical implementation of our fluid solver. To accomplish this, we solve the problem of a lid-driven cavity and compare our simulated results with that available in literature. In this section, we shall use the results presented by Sahin [119] and Jiang et al. [120].

Our lid-driven cavity is made up of a cubic fluid domain of sides $1m \times 1m \times 1m$. A velocity boundary condition of $\vec{u}_\Gamma = 0$ is imposed on five walls. The five faces are located at $\vec{X} = \vec{X}(0, y, z)$, $\vec{X} = \vec{X}(1, y, z)$, $\vec{X} = \vec{X}(x, 0, z)$, $\vec{X} = \vec{X}(x, 1, z)$ and $\vec{X} = \vec{X}(x, y, 0)$. A shearing velocity boundary condition of $\vec{u}_\Gamma = [010]^T$ is imposed on the sixth face at $\vec{X} = \vec{X}(x, y, 1)$. As for the pressure, we impose $\vec{\nabla} p \cdot \vec{n} = 0$ on all faces. A Reynolds number of $\mathrm{Re} = 400$ is achieved by imposing a fluid kinematic viscosity of $\upsilon = 400^{-1} m^2 / s$ and a fluid density of $\rho = 1 kg / m^3$. A streamline plot of the fluid flow is shown in Figure 4.1(a). A comparison for the velocity along the centerline $\vec{X} = \vec{X}(0.5, 0.5, z)$ is shown in Figure 4.1(b). It can be seen our results agree well with those of Sahin [119] and Jiang et al. [120].

We therefore conclude in this section that our fluid solver has been reasonably validated.

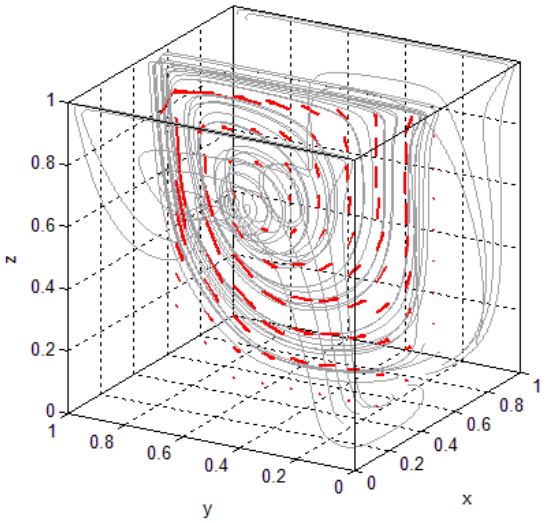

(a)

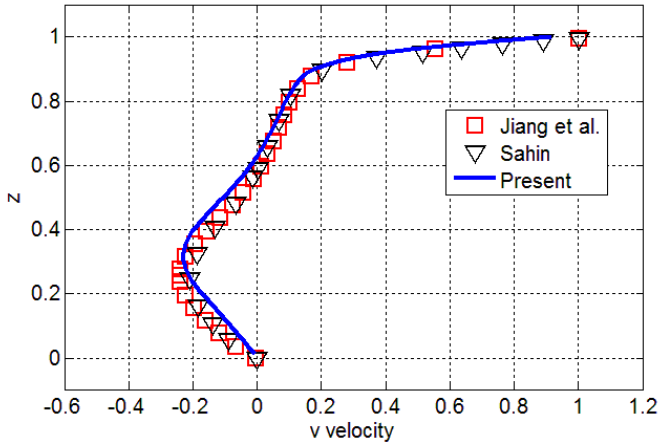

(b)

Figure 4.1 (a) Stream traces and vectors for a lid-driven cavity is shown. The Reynolds number for this simulation is $\mathrm{Re} = 400$. This plot is taken at $\vec{X} = \vec{X}(0.5, y, z)$. Flow in the cavity is driven at the face $\vec{X} = \vec{X}(x, y, 1)$ with a velocity of $v = 1$. (b) Validation of the centerline velocity along $\vec{X} = \vec{X}(0.5, 0.5, z)$ is shown. We obtain good agreement with simulation results from Sahin [119] and Jiang et al [120]. A 80^3 grid is used in our simulation.

4.2 Validation of solid model using an Euler-Bernoulli beam

We next demonstrate that our simple rod-and-spring model can be used to model an Euler-Bernoulli cantilever beam with a bending modulus EI. As stated in equation 3.32, the relationship between the bending modulus EI, the torsion spring constant T_θ and the distance between control points Δs_0 on the cantilever beam is given as

$$EI = T_\theta \Delta s_0 . \tag{3.32}$$

In these simulations, a cantilever beam of length $L = 0.5m$ and stiffness $EI = 5.56 \times 10^{-3} Nm^2$ is used. A force of $6.67 \times 10^{-3} N$ is applied at the beam tip in the positive $y-$direction. The base of the beam is located at $\vec{X} = \vec{X}\left(0.5, 0.5, 0\right)$ where a clamped boundary condition has been imposed. The linear spring constant k is set stiff enough such that stretching between the control points can be neglected in all our simulations. The kinematic viscosity υ and density ρ are maintained at $400^{-1} m^2/s$ and $1 kg/m^3$ respectively. The boundary conditions on all sides of the fluid domain are $\vec{u} = 0$ and $\vec{\nabla} p \cdot \vec{n} = 0$. With these parameters, the system is over-damped and no significant oscillations of the cantilever beam are observed. The parameters used for this set of simulations are shown in Table 4.1.

Figure 4.2(a) shows the convergence of the cantilever deflection as different numbers of discretized points M are used. As M is increased, the deformation of the cantilever approaches the analytical Euler-Bernoulli beam equation. We can then calculate the relative percentage error at the cantilever tip as

$$\text{Relative percentage error} = \frac{\Delta y}{\Delta y_{Euler-Bernouli\ Eqn}} \times 100\% , \tag{4.1}$$

where Δy is the simulated cantilever tip deflection and $\Delta y_{Euler-Bernouli\ Eqn}$ is the analytical deflection given by the Euler-Bernoulli beam equation. The relative percentage error in tip deflection is shown in Figure 4.2(b). We find that as M is increased to $M = 39$, the relative percentage error is reduced to 2%.

We can therefore conclude in this section that our simple rod-and-spring model can be used to approximate a beam.

	Description	**Symbol**	**Units**	**Value**
Cantilever parameters	Cantilever beam length	L	M	0.5
	Linear spring constant	k	N/m	200
	Torsion spring constant	T_θ	Nm/rad	3.33×10^{-2}-0.422
	Tip loading force	P	N	6.67×10^{-3}
Fluid parameters	Fluid density	ρ	kg/m^3	1
	Fluid kinematic viscosity	υ	m^2/s	400^{-1}
Fluid domain dimensions	Dimensions of fluid domain	$H_\Omega \times L_\Omega \times W_\Omega$	m	1×1×1
Numerical parameters	Number of cantilever points	N	-	4 – 39
	Number of fluid grid points	N_x, N_y and N_z	-	20^3 - 100^3
	Time step size	Δt	s	5.0×10^{-4}

Table 4.1 The parameters used for simulations of a cantilever beam under a tip loading is shown. The number of points discretizing the beam M varies from 4 to 39. A constant bending modulus of $EI = T_\theta \Delta s_0 = 5.56\times10^{-3}\,Nm^2$ is used. The linear spring constant k is stiff enough such that stretching of the beam can be neglected.

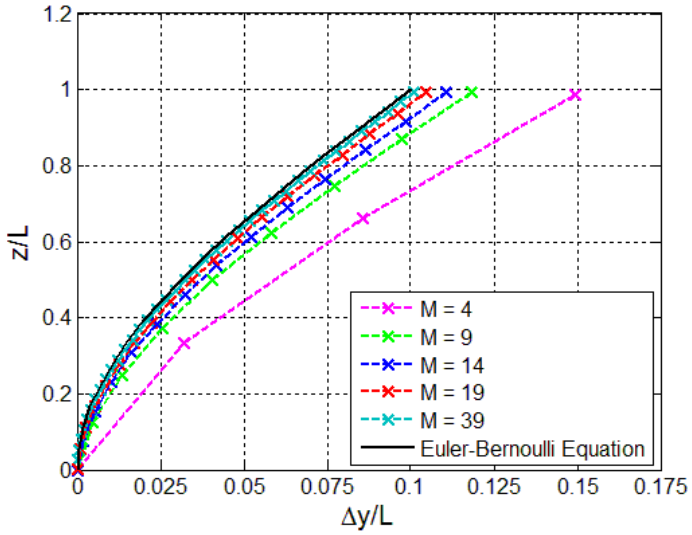

(a)

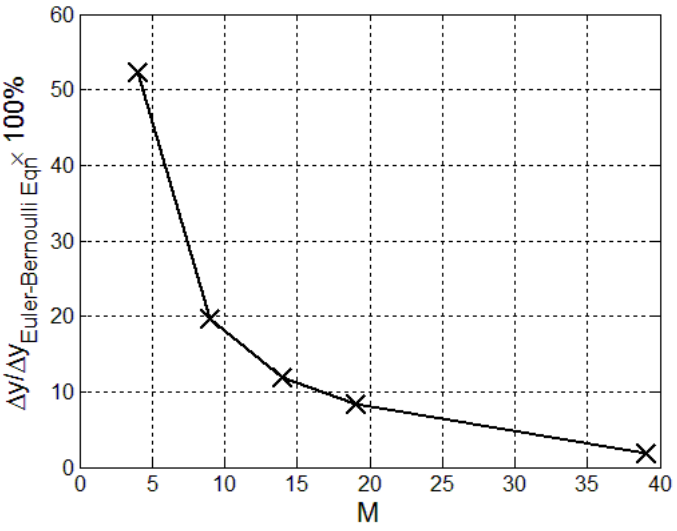

(b)

Figure 4.2 (a) The final steady deformation of the simulated cantilever beams are shown. As the number of points M making up the cantilever beam is increased, the solution approaches the analytical Euler-Bernoulli solution. (b) The percentage error in tip deflection is shown. As the number control points M is increased, the error is reduced. At $M = 39$, the error is 2%.

4.3 Benchmarking of code against a case of flow reversal by cilia

In sections 4.1 and 4.2, we validate our fluid solver and solid model using steady-state cases. We shall next benchmark the dynamic, solid-fluid coupling aspect of our code. For this, we choose to benchmark our results against results from a study presented by Alexeev et al. [44].

Alexeev et al. found that, in a setup where artificial cilia are positioned at an angle of $45°$ to the substrate and subjected to a vertical oscillating force, flow reversals will occur for certain values of the sperm number Sp. Sp is a non-dimensional number given as

$$Sp = L\left(\frac{\left(2\pi\hat{f}\right)(4\pi\mu)}{EI}\right)^{1/4}. \tag{4.3}$$

Here, $\hat{f}$ is the frequency of cilia due to forced oscillations, μ is the dynamic viscosity of the fluid, EI is the bending stiffness of the cilia and L is the length of the cilia. By necessity, here $\hat{f}$ is also the frequency of the imposed force.

In this study, the authors imposed a vertical, sinusoidal oscillating force on the tip of each cilium. The non-dimensional force amplitude is given by A, where A is given as

$$A = \frac{aL^2}{3EI}, \tag{4.4}$$

where a is the actual force amplitude given in Newtons.

We set up our benchmark case with an array of 21×21 cilia enclosed in a fluid chamber as shown in Figure 4.3(a). Each cilium is separated by a distance of L in the $x-$direction and a distance of $0.5L$ in the $y-$direction. The chamber height is $1.5L$. These parameters are as per [44].

In our simulations, the substrate at $\vec{X} = \vec{X}(x, y, 0)$ and the ceiling at $\vec{X} = \vec{X}(x, y, H_\Omega)$ have fluid boundary conditions of $\vec{u} = 0$ and $\vec{\nabla} p \cdot \vec{n} = 0$. The side faces have fluid boundary conditions of $\vec{\nabla}(\vec{u} \cdot \vec{n}) = 0$ and $p = 0$. Our simulation parameters are listed in Table 4.2.

	Description	**Symbol**	**Units**	**Value**
Cilia parameters	Cilia length	L	m	4.91×10^{-5}
	Cilia bending stiffness	EI	Nm^2	2.26×10^{-19}
	Cilia stretching stiffness	k	Nm^{-1}	1.2×10^{-2}
	Force magnitude at cilia tip	A	N	2.81×10^{-9}
	Forcing frequency	$\hat{f}$	Hz	30 - 400
Fluid parameters	Fluid density	ρ	kgm^{-3}	100 - 1000
	Fluid dynamic viscosity	μ	$kgm^{-1}s^{-1}$	1.0×10^{-4} - 1.0×10^{-3}
Fluid domain parameters	Fluid chamber length	L_Ω	m	1.26×10^{-3}
	Fluid chamber width	W_Ω	m	7.0×10^{-4}
	Fluid chamber height	H_Ω	m	7.32×10^{-5}
Numerical parameters	Number of cilium control points	N_c	-	14
	Time step size	Δt	s	1.25×10^{-6}
	Fluid grid size	h	m	2.9×10^{-6}

Table 4.2 Parameters used in our simulations for benchmarking against results by Alexeev et al. [44] are shown.

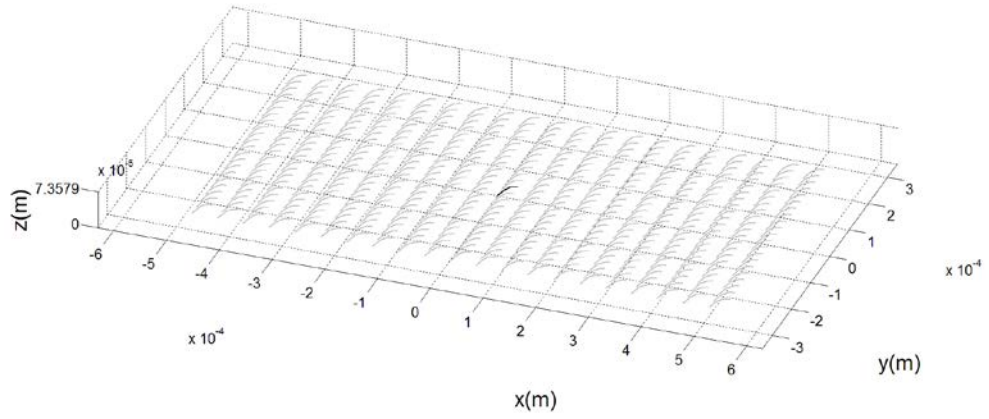

(a)

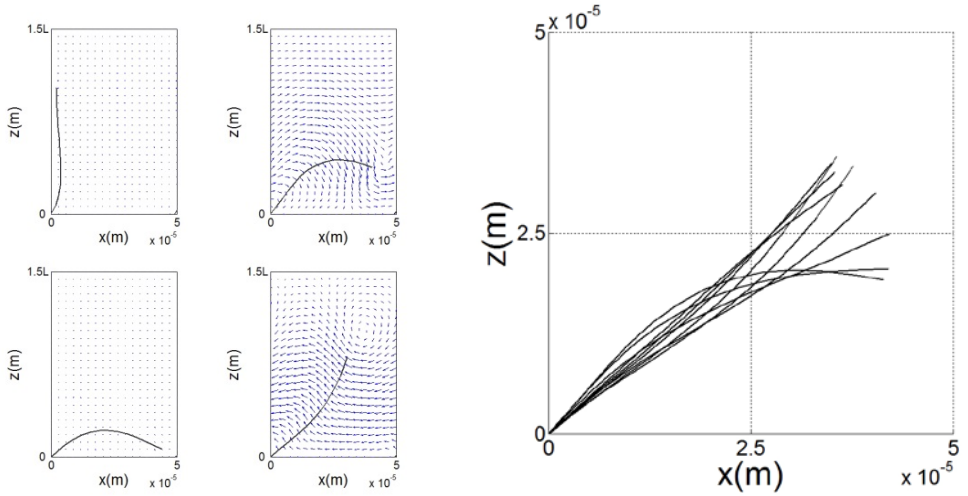

(b) (c)

Figure 4.3 (a) Our benchmark case consists of an array of 21×21 cilia. The cilia are angled at $45°$ to the substrate and tip loadings are imposed. Each cilium is spaced a distance of L in the $x-$direction and a distance of $0.5L$ in the $y-$direction. The chamber height is $1.5L$. Boundary conditions for the fluid are $\vec{u}=0$ and $\vec{\nabla}p\cdot\vec{n}=0$ for the substrate and chamber ceiling, and $\vec{\nabla}\left(\vec{u}\cdot\vec{n}\right)=0$ and $p=0$ for the surrounding side faces. In this figure, $Sp=3$. (b) The oscillations of the cilia at $\left(0,0\right)$ for the case of $Sp=3$ is shown. The cilium exhibits deformations large enough such that the cilia tip contacts the substrate. (c) The oscillations of the cilium at $\left(0,0\right)$ for the case of $Sp=5$ are shown. Compared to the case where $Sp=3$, the oscillations here are of smaller amplitude. The ciliuim shapes in (b) and (c) are similar to that obtained by Alexeev et al. [44].

We choose the cases where $Sp = 3$ and $Sp = 5$ for our benchmark. In both cases, we set $A = 10$. These two cases are of special significance because (1) the magnitudes of flow rates at $Sp = 3$ and $Sp = 5$ are largest at $A = 10$, (2) the net flow direction is reversed between $Sp = 3$ and $Sp = 5$, and (3) at $Sp = 3$, the cilia exhibit large deformations such that their tips spend a significant portion of their oscillation cycle pressed against the substrate of the chamber.

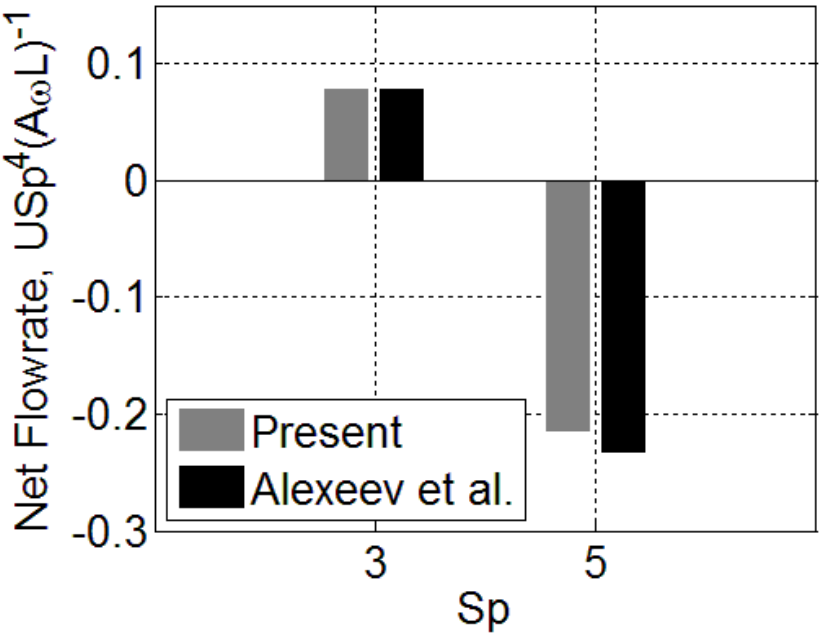

Figure 4.4 Fluid flow rates obtained in our simulations are shown. Our model is able to produce similar flow magnitudes and flow reversals as obtained by Alexeev et al. [44].

The shapes of a representative cilium as it undergoes its oscillations are shown in Figure 4.3(b). This cilium is located at $(0,0)$ in the flow chamber, shown shaded black in Figure 4.3(a). The shapes of this cilium are similar to those obtained by Alexeev et al. [44] shown in Figure 2.8.

A side view of this cilium when $Sp = 5$ is shown in Figure 4.3(c). In this case, the oscillation amplitudes are smaller than in the case where $Sp = 3$. At no

time is the cilium observed to contact the substrate. The cilium shapes shown here are similar to that obtained by Alexeev et al. [44].

Figure 4.4 compares the flow rates for the cases of $Sp = 3$ and $Sp = 5$. As in Alexeev et al. [44], we scale our flow rate with Sp, A, $\varpi = 2\pi \hat{f}$ and L. Although Alexeev et al. [44] used a 3D prismatic structure to represent the cilia while we used a simple 1D spring model, we are able to obtain similar flow magnitudes and similar flow reversals between $Sp = 3$ and $Sp = 5$.

We thus conclude in this section that our simple 1D spring model is able to reproduce the results obtained by Alexeev et al. [44] reasonably well. We can also conclude the fluid-structure dynamics in our code has also been validated.

4.4 Performance of numerical implementation of IBM code

In the final section of this chapter, we test the computational performance of our parallelized code using an SGI Altix UV 1000. Here, we solve the problem of a lid-driven cavity of $\mathrm{Re} = 400$ around a single cantilever beam, as shown in Figure 4.5(a). The parameters for the lid-driven cavity are as per Section 4.1 while parameters for the beam model are as per Section 4.2. However, unlike Section 4.1, here, the beam is unloaded, i.e. $P = 0N$.

For this section, the beam is discretized into 40 control points and the fluid domain is discretized into a 128^3 grid. The speed-up curve is shown in Figure 4.5(b). It can be seen that when the number of processors N_{proc} is doubled from 32 to 64, a speed-up greater than 2 is achieved. When N_{proc} is quadrupled from 32 to 128, a speed-up of 3.2 is achieved. At this value of N_{proc}, our code presents an efficiency of about 80%.

We therefore conclude in this section that we have obtained a reasonably efficient, parallelized code with good performance.

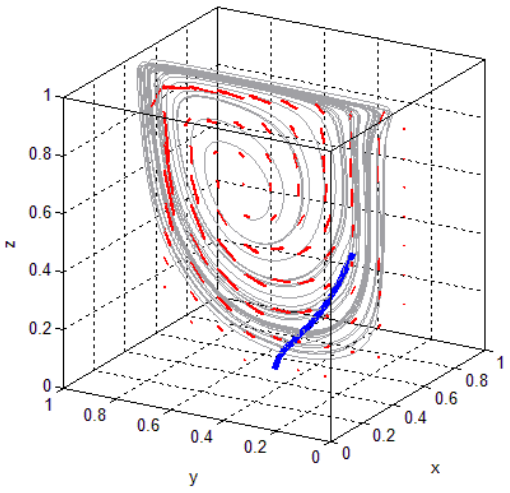

(a)

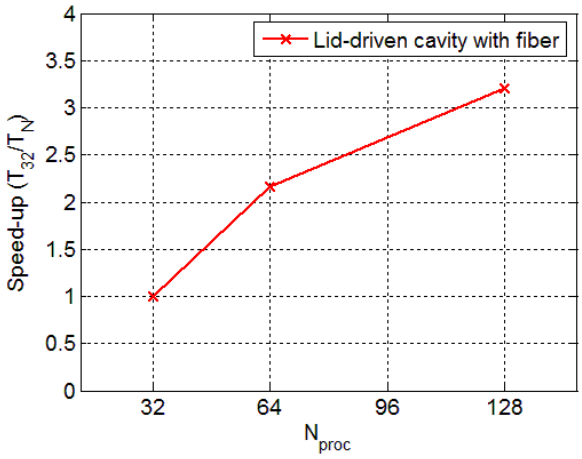

(b)

Figure 4.5 (a) The problem of a lid-driven cavity with a single vertical beam is used to test the efficiency of our code. (b) Results of a speed-up test for our code is shown.

5 Characterization of simulated cilia array

5.1 Robustness of cilia metachronal waves

In this section we shall discuss some characteristics of our simulated cilia system [121]. As the frequencies and wavelengths of metachronal waves will be used frequently throughout this thesis, we shall devote Section 5.2 to a discussion on the methods used to obtain these quantities.

Next, we shall determine the stability and robustness of our metachronal waves by subjecting them to two forms of perturbations.

In Section 5.3, we impose the first form of perturbation by reversing the strokes of a selected group of cilia. By reversing the strokes of cilia, we seek to simulate realistic experiments where localized reversal of cilia stroke is induced by photorelease of caged calcium [25]. By studying the kymographs of metachronal waves, we observe that if the perturbed cilia array is small, metachronal waves formed before and after the perturbed regions are hydrodynamically coupled. However, if the perturbed region is large, this coupling would seem unlikely.

In Section 5.4, we impose the second form of perturbation by imposing deformations on the substrate. The deformations are imposed in the form of cyclic stretching of the cilia substrate in the direction parallel to forward stroke, i.e. the $x-$direction. We then observe the effect of cyclic stretching on the natural beat frequency of the cilia. We observe the superposition of both the cilia beat frequency and the imposed cyclic stretching frequency.

In Section 5.5, we attempt to discover the mechanism behind the formation of metachronal waves. We do this by varying the parameters α and β in

equations 3.33 and 3.34. We show that as α and β is reduced, the cross-wise coupling between adjacent cilia weakens and metachronal waves do not form.

In Section 5.6, we show in our model that metachronal waves will form in the case where the cilia array is irregular. Photographs of *Paramecium* [122] (Figure 5.1(a)) show a regular arrangement of cilia basal bodies. However in nature, there are many instances where cilia arrangements are irregular (Figure 5.1(b)). We therefore seek to extend our model to cases of irregular cilia arrangement.

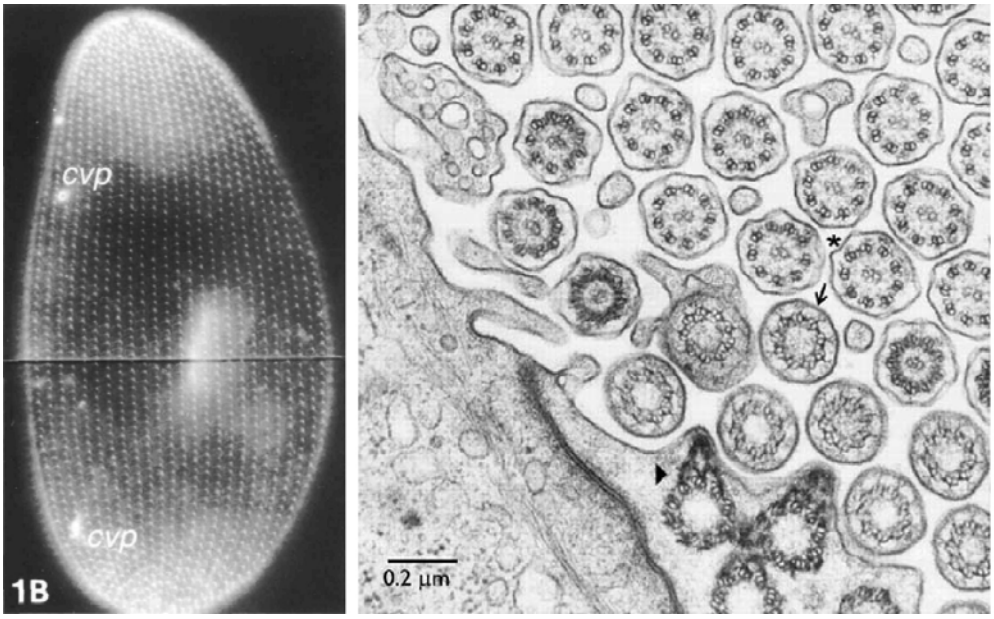

(a) (b)

Figure 5.1 (a) The regular arrangement of basal bodies on *Paramecium* is shown. Image is reproduced from [122]. (b) The irregular arrangement of mouse oviduct cilia is shown. Image is reproduced from [123].

In Section 5.7, we shall determine the flux calculation over the cilia array. We show that as our finite cilia array is large enough, the flux passing over the centre of the array is a good approximation to that over an infinite cilia bed.

In this chapter, we shall confine our discussion to the case where cilia bending stiffness $EI = 6.9 \times 10^{-21} Nm^2$. The rest of the simulation parameters are as shown in Table 3.1.

The implementation of the forcing function in our model does not allow us to specify metachronal wave direction. As it happens, symplectic metachronal waves are generated. However, as will be shown in Section 6.2, antiplectic metachronal waves can be generated by stiff cilia. Since most waves generated in our model are symplectic, we shall focus on those.

5.2 Extracting frequencies and wave numbers of cilia array

In this section, we shall describe how the wave numbers and frequencies of cilia in our simulations are obtained. The methods presented here will be used for the rest of this thesis.

By simulating our array of 21×21 cilia (Figure 5.2(a)), we observe the spontaneous formation of metachronal waves. The heights of cilia tips above the substrate are then used to track the oscillations of cilia. The imposed active force $\vec{f}_{active}$ causes each cilium tip to attain its maximum height during the forward stroke, and its minimum height during the reverse stroke. This is because during the forward stroke, $\vec{f}_{forward}$ is imposed on the cilium. $\vec{f}_{forward}$ consists of a force component in the $z-$direction, which serves to raise the cilium tip. During the reverse stroke, $\vec{f}_{reverse}$ is imposed on the cilium. $\vec{f}_{reverse}$ consists of a force component in the $y-$direction, which serves to lower the cilium tip.

By tracking the heights of each cilium tip, metachronal wave fronts over the array can then be obtained (Figure 5.2(b)). Here, cilia tip heights are represented as contours. Cilia tips are higher during the forward stroke; therefore light contours represent cilia undergoing the forward stroke.

Similarly, cilia tips are lower during the reverse stroke; therefore dark contours represent cilia undergoing the reverse stroke.

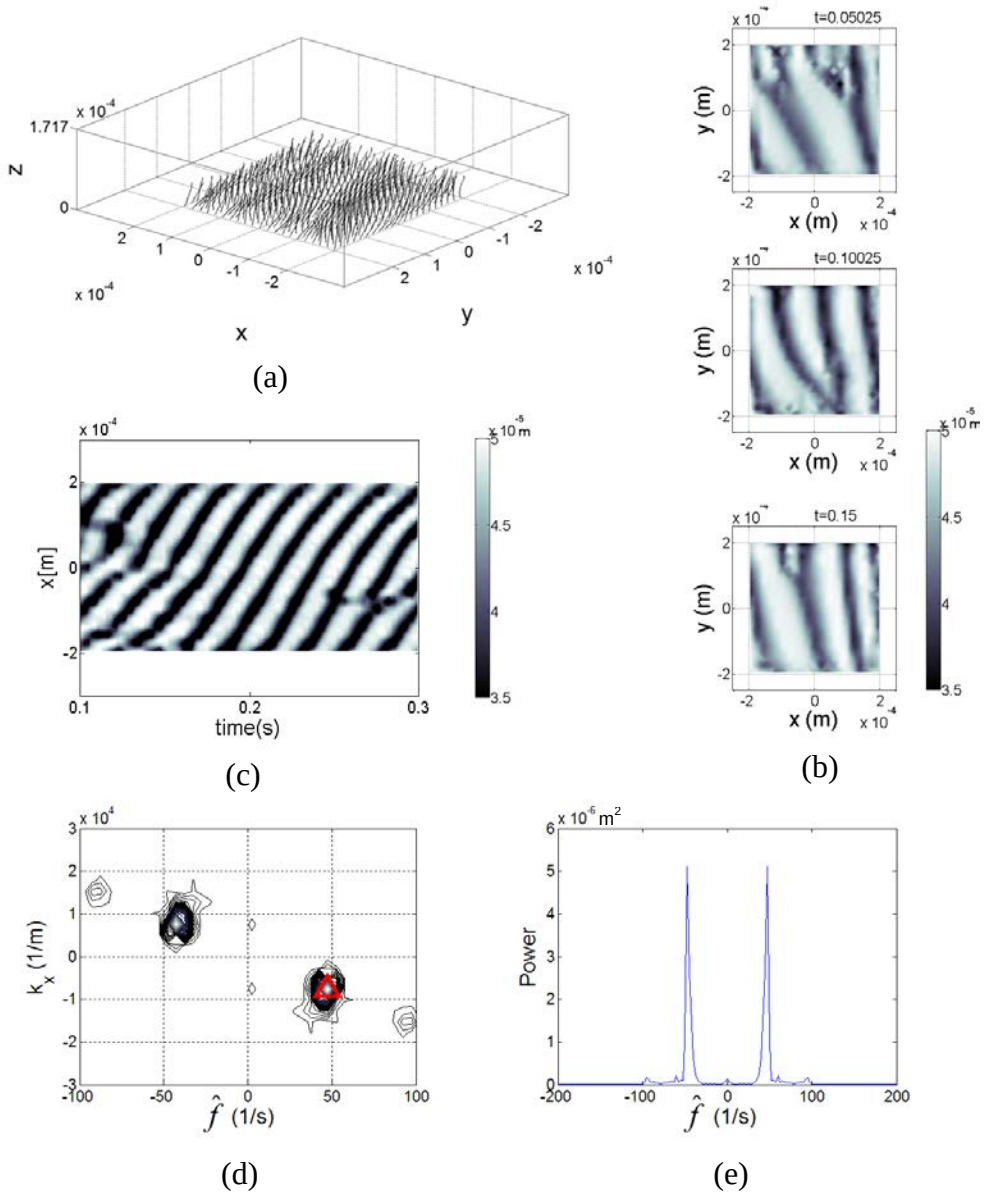

Figure 5.2 (a) We use the immersed boundary method to simulate an array of 21 by 21 cilia. (b) By tracking the cilia tip heights above the substrate, we obtain contour plots indicating cilia beat motion. The colorbar indicates the heights of cilia tips above the substrate. Since cilia tips are higher during the forward stroke and are lower during the reverse stroke, light contours therefore represent cilia in the forward stroke while dark contours represent cilia in the reverse stroke. (c) By extracting a cross section at $y = 0$ at each time, we are able to obtain a kymograph. (d) By performing fast Fourier transforms (FFTs) on the kymographs, we obtain the wave numbers and frequencies of the metachronal waves. (e) The dominant frequencies in our simulations can then be extracted. This dominant frequency corresponds to the red triangle in (d). Consequently, dominant wave numbers can also be obtained.

In our simulations, we record snapshots of the cilia array at intervals of $2\times10^{-4}s$. At each time interval, we first generate the contours of cilia tip heights (Figure 5.2(b)). The movement of contours show the movement of metachronal waves across the cilia array. Next, we extract the contour values at $y=0$ to assemble a kymograph (Figure 5.2(c)). The kymograph allows us to study the propagation of metachronal waves in time.

By performing fast Fourier transforms (FFTs) on the kymograph, we obtain a contour plot of the kymograph spectra (Figure 5.2(d)). k_x, the dominant wave number in the $x-$direction, and $\hat{f}$, the dominant frequency of the cilia array, can then be obtained. The dominant frequency obtained is the observed frequency of the metachronal waves. This frequency (Figure 5.2(e)) is also the intrinsic frequency of cilia oscillation determined by our choice of the forcing function $\vec{f}_{active}$.

5.3 Metachronal waves are resistant to cilia disruptions through cilia stroke reversal

It is of interest to study how the propagation of metachronal waves is affected by cilia stroke reversal. For example, Narematsu et al.[124] showed that when the motions of a localized patch of cilia are reversed through the localized photorelease of caged calcium ions, metachronal waves are still able to pass through the patch, with no change in the wave's wavelength or frequency. This observation suggests that the propagation of metachronal waves are robust to localized perturbations, and further studies are needed to establish the spatial extent of perturbations needed to destablize metachronal wave propagation. As a first step towards this, we attempt to use our model to simulate the cilia motion reversal in a localized cilia patch. We do this by imposing the following forcing function on the cilia control points,

$$\vec{f}_{forward}\left(\vec{X},t\right)=f_x\left(\vec{X},t\right)\left(-\vec{i}+\alpha\vec{k}\right), \tag{5.1}$$

$$\vec{f}_{reverse}\left(\vec{X},t\right)=f_x\left(\vec{X},t\right)\left(\vec{i}+\beta\vec{j}\right). \tag{5.2}$$

These forcing functions are similar to equations 3.33 and 3.34, with the exception that the force vectors in the $x-$ and $y-$directions are reversed.

We first subject a small 3×3 cilia array to stroke reversal. This small array is located in the center of the full cilia array. The metachronal waves through the array are shown in Figure 5.3. We observe that as a metachronal wave front (marked by a solid black line) forms (Figures 5.3(a)) and approaches the perturbed region (Figure 5.3(b)), the metachronal wave front is broken (Figures 5.3(c) and (d)). As the wave front passes over the perturbed region, the metachronal wave front reestablishes itself and reforms (Figures 5.3(e) and (f)).

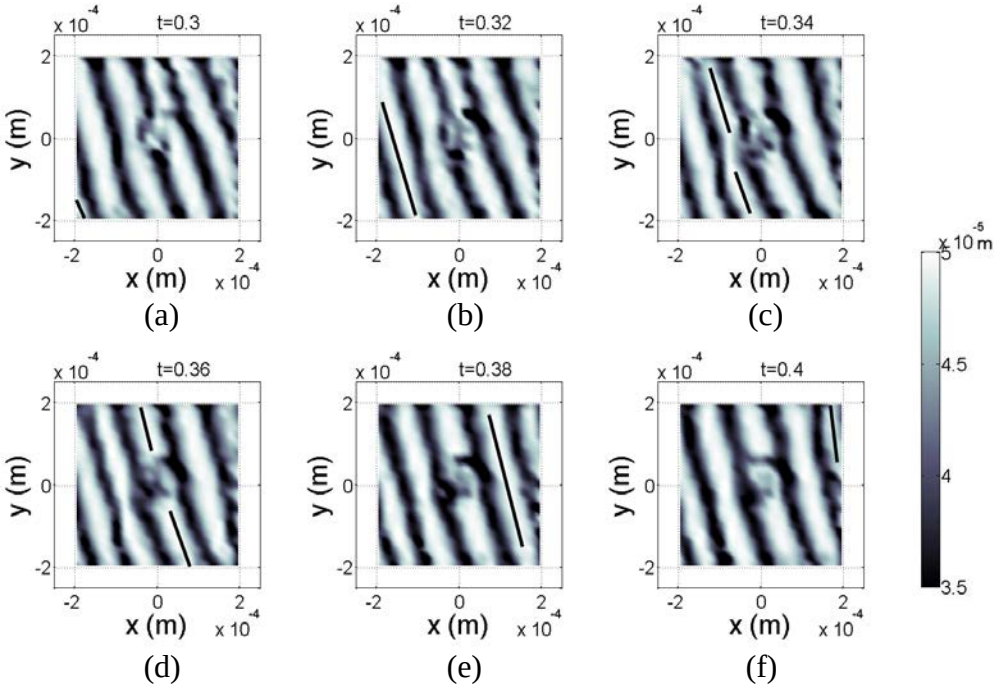

Figure 5.3 This figure shows contours of metachronal waves passing over a 3×3 array where the cilia has been perturbed by reversal of the cilia beat stroke. A chosen wave front (solid black line) is marked and tracked. The wave front forms (a) and travels to the perturbed region (b), The wave front breaks over the perturbed region in (c) and (d), then reforms after it in (e). The wave front then travels to the edge of the array (f).

We next increase the size of the size of perturbation to a 21×3 cilia array (Figure 5.4). This array is oriented such that its long axis is perpendicular to the direction of the cilia forward stroke. This orientation is chosen so that the wave front enters the perturbed region fully.

We observe that metachronal wave fronts forming before (Figures 5.4(a)-(b)) and after (Figures 5.4(d)-(f)) the perturbed region. The wave fronts vanish when they meet the perturbed region (Figure 5.4(c)).

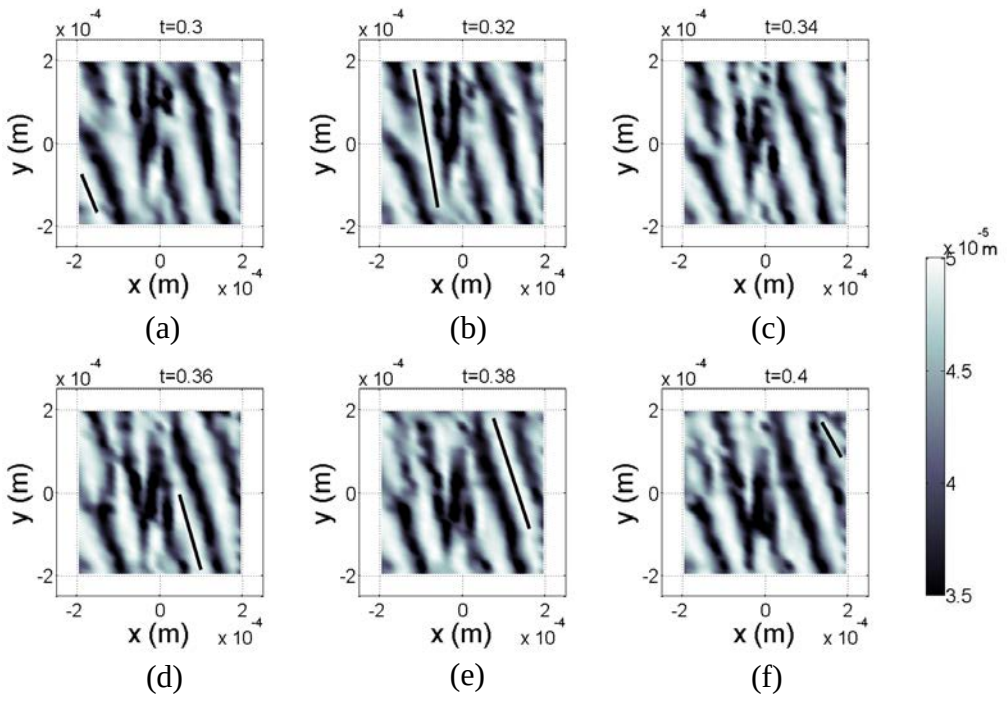

Figure 5.4 This figure shows contours of metachronal waves passing over a 21×3 array where the cilia has been perturbed by reversal of the cilia beat stroke. A chosen wave front (solid black line) is marked. The wave front forms (a) and travels to the perturbed region (b). The wave front vanishes at the edge of the perturbed region (c). Another wave front is formed after the perturbed region (d), and travels to the edge of the array (e), (f). There is no evidence the wave front after the perturbed region in (d)-(f) is associated with the wave front before the perturbed region in (a)-(b).

We continue to increase the size of the perturbed region to an 21×7 array (Figure 5.5). In this instance, the perturbed array is large enough such that metachronal waves are observed within the perturbed region. A chosen wave front in the unperturbed region is marked with a solid black line while a chosen wave front in the perturbed region is marked with a solid blue line.

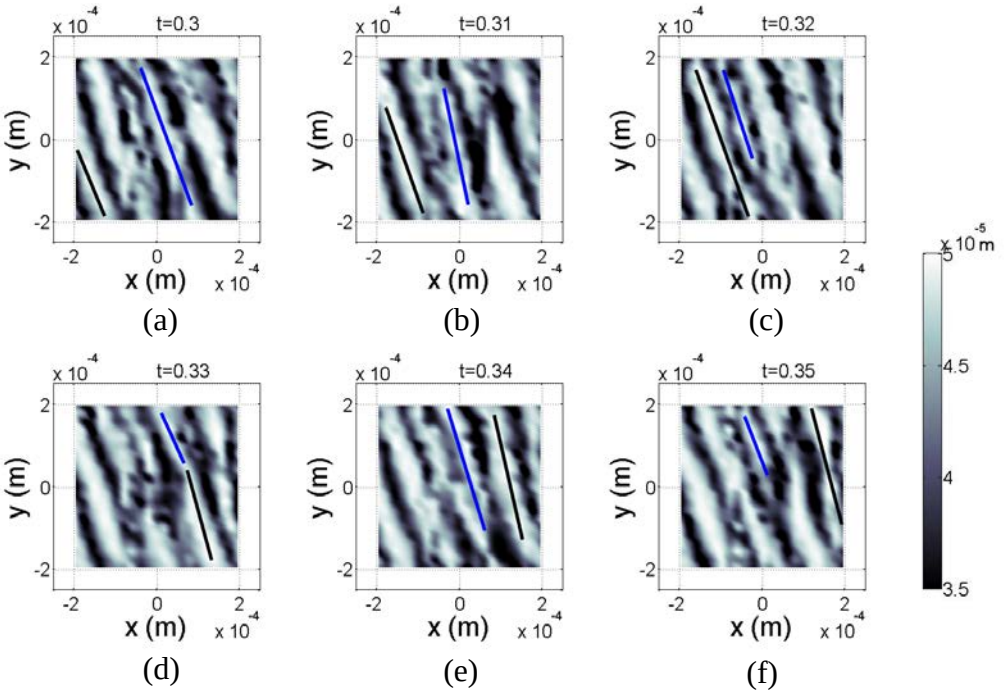

Figure 5.5 This figure shows contours of metachronal waves passing over an 21×7 array where cilia stroke has been perturbed by having the cilia beat stroke reversed. The perturbed region is now large enough to form its own metachronal waves. Two chosen wave fronts (solid black and blue lines) are marked. The black line represents a wave front in the unperturbed region while the blue line represents a wave front in the perturbed region. The wave fronts form in (a), (b) and (c). The wave front marked in black travels rightward while the wave front marked in blue travels leftward. Both wave fronts vanish at the boundary between the perturbed and unperturbed regions. New wave fronts are formed after the perturbed regions in (d). The new wave front marked in blue travels leftward while the new wave front marked in black travels rightward in (e)-(f).

As before, when the perturbed region is an 21×3 array, we observe metachronal waves forming before (Figures 5.5(a)-(c)) and after (Figures 5.5(d)-(f)) the perturbed region. The metachronal wave front in the unperturbed region travels rightward to the perturbed region and vanishes. Similarly, the metachronal wave front in the perturbed region travels leftward to the unperturbed region and vanishes.

In all 3 cases of disruptions due to cilia reversal investigated here, it can be seen that metachronal wave fronts are formed immediately outside the regions of perturbation. We do not observe any significantly large region adjacent to the perturbed regions where metachronal wave fronts do not form.

We therefore show in this section that the metachronal waves generated in our model are robust and stable. They are resistant to localized perturbations within the array.

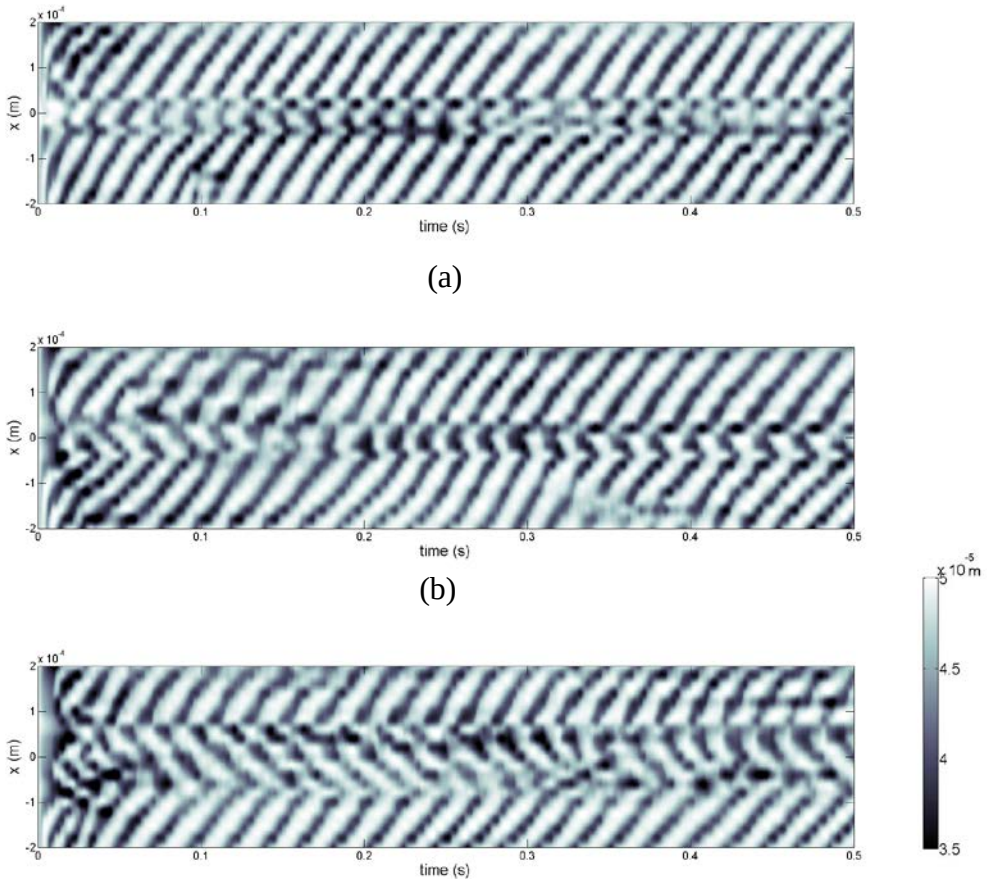

Figure 5.6 This figure shows kymographs taken at the cross section $y = 0$. (a) Kymograph of a 3×3 cilia array subjected to perturbation is shown. Wave fronts across the perturbed region are not continuous. (b) Kymograph of a 21×3 cilia array subjected to perturbation is shown. Wave fronts across the perturbed region are observed to be continuous. (c) Kymograph of a 21×7 cilia array subjected to perturbation is shown. In this case, the perturbed region is large enough such that it can form its own metachronal waves. Wave fronts across the perturbed region are observed to be only somewhat continuous.

Furthermore, we observe that if the perturbed region is large enough, the region can form its own metachronal waves. From our simulations, we report that the number of rows of cilia per wavelength is $N_\lambda \sim 4-7$. This suggests

that for a wave front to form, we need at least 4 to 5 rows of cilia; hence any region of disturbance consisting of less 4 to 5 cilia should not be able to form its own metachronal waves.

We now seek to understand if the metachronal waves observed before (i.e. to the left of) the perturbed region is hydrodynamically coupled to the metachronal waves observed after (i.e. to the right of) the perturbed region. We do this by examining the kymographs of the metachronal waves taken at the cross section $y = 0$. This is shown in Figure 5.6.

We observe that in the case where a 3×3 cilia array is perturbed (Figure 5.6(a)), the wave fronts across the perturbed region are not continuous. However we do know that here the waves before and after the perturbed region are related, as reasoned in Figure 5.3.

In the case where a 21×3 cilia array is perturbed (Figure 5.6(b)), we observe that wave fronts are discontinuous across the perturbed region for $t < 0.2s$, but are distinctly continuous for $t > 0.3s$. We suggest this is an indication that hydrodynamic coupling causes the cilia in the perturbed region to adapt such that continuous wave fronts are formed. This is likely because the perturbed region is narrow (i.e. with a width less than 4-7 cilia) and can be affected by hydrodynamic influence from the larger unperturbed regions.

In the case where a 21×7 region is perturbed (Figure 5.6(c)), we observe that the wave fronts are only somewhat continuous for the simulation duration. We suggest this is an indication that in this case the perturbed region is large (i.e. with a width greater than 4-7 cilia) enough such that the hydrodynamic influence from the unperturbed regions are no longer significant enough to affect the cilia dynamics within the perturbed region.

We therefore conclude in this section that hydrodynamic coupling can affect cilia motion within perturbed regions if the perturbed regions are small or narrow (i.e. with a size containing less than 4-7 cilia). This hydrodynamic coupling causes the metachronal waves before and after the perturbed regions

to be coupled. If the perturbed region is large enough, it is very likely that cilia dynamics in the perturbed region are independent of cilia dynamics in the unperturbed region. The metachronal waves observed after the perturbed region are therefore likely to be only weakly coupled to the metachronal waves observed before the perturbed region.

For comparison with literature, the value of d/L can be estimated to be $d/L \sim 0.1-0.5$ [61, 87, 129, 130]. Assuming $L \sim 5\mu m$, the value of metachronal wavelength is estimated to be $\lambda \sim L-2L$ [88, 125, 126]. The number of cilia per wave can therefore be estimated as $N_\lambda = \frac{\lambda}{d} \sim \left(\frac{d}{L}\right)^{-1}$ to $2\left(\frac{d}{L}\right)^{-1}$, and therefore $N_\lambda \sim 2-20$. Our reported value of $N_\lambda \sim 4-7$ thus agrees with that in literature.

Next, we shall study the effects of perturbations on the fluid flow field. We shall observe the trajectories of passive massless particles embedded in the flow field. These particles are seeded at a height of $1.07L$ above the substrate. These particles are merely advected with fluid velocity as per equations 3.38 and 3.39; they do not otherwise interact with the flow field.

Figure 5.7 shows the particle trajectories of the case with no cilia perturbations (a), the case with an 3×3 array of perturbed cilia (b), the case with an 21×3 array of perturbed cilia (c) and the case with an 21×7 array of perturbed cilia (d).

We observe that in the case where an 3×3 array of cilia is perturbed (Figure 5.7(b)), particles flow in a curved path around the perturbed region. This is in contrast to the relatively straight trajectories if no perturbation is imposed (Figure 5.7(a)).

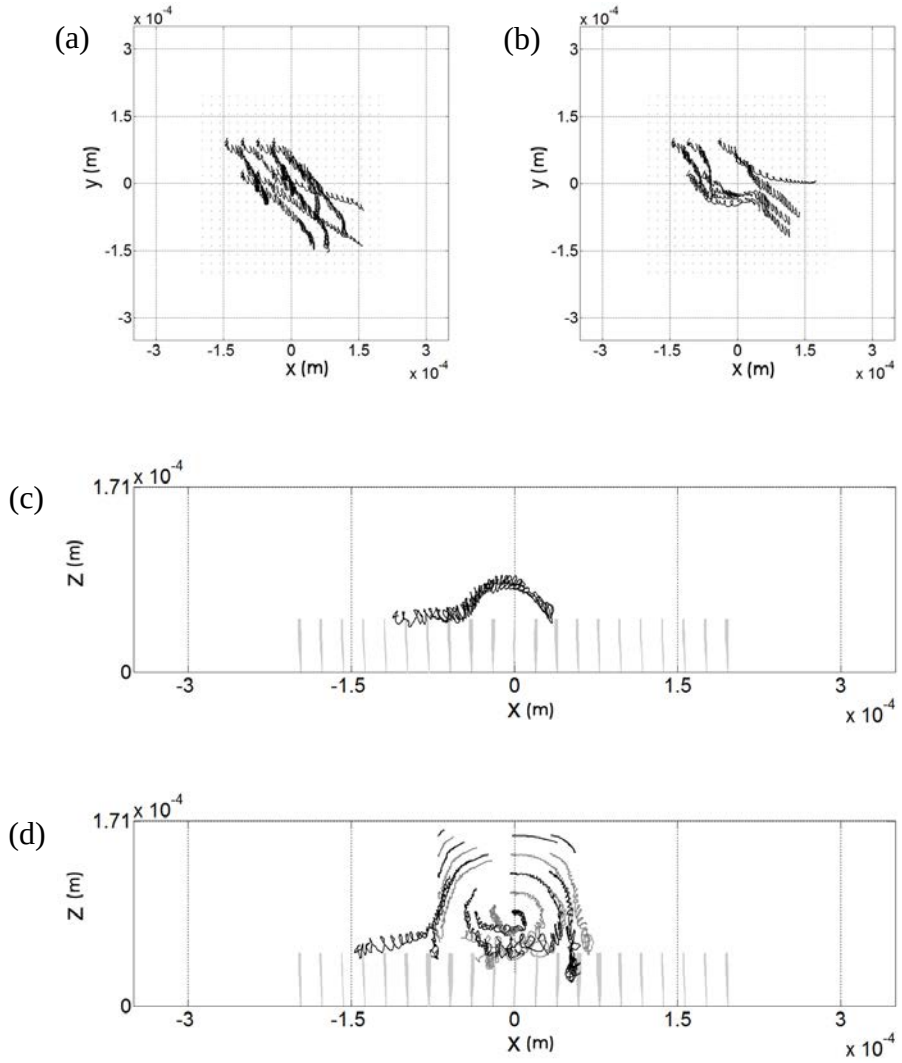

Figure 5.7 This figure shows the paths of passive tracer particles over perturbed regions of the cilia array. (a) In the case where no cilia is perturbed, the particles flow smoothly over the cilia array. (b) In the case where the perturbed region is a small 3×3 array, particles flow around the perturbed region. (c) In the case where the perturbed region is an 21×3 array, particles flow over the perturbed region. (d) In the case where the perturbed region is an 21×7 array, a vortex is formed above the perturbed region. Some particles flow over the perturbed region while others are entrained within the vortex. In (a), (b) and (c), the particles are seeded at a height of $1.07L$ above the substrate.

When the perturbed region is enlarged to an 21×3 array (Figure 5.7(c)), we observe particles flowing in a curved path over the perturbed region. This observation indicates the formation of a vortex above the perturbed region. In the case where the perturbed region is enlarged to an 21×7 array (Figure 5.7(d)), a vortex is clearly observed above the perturbed region. This is shown

by the trajectories of particles above the perturbed region. Some particles are observed to flow over the perturbed region while others are entrained within the vortex.

These observations are similar to those obtained experimentally by Narematsu et al. [124]. Here, the authors used Indian Ink to observe the existence of vortices over perturbed cilia regions. Experimentally, the cilia beat stroke has been reversed by local photorelease of caged calcium ions, forming a perturbed condition similar to that in our simulations.

In this section, we conclude that using our simplified cilia model, perturbation of cilia by way of localized cilia stroke reversal can produce vortices in the flow field. This is a phenomenon that has been observed experimentally.

5.4 Metachronal waves are resistant to substrate deformations

We next perturb the cilia array by subjecting the cilia substrate to cyclic stretching. We simulate cyclic stretching by imposing a sinusoidal displacement on the control points representing the cilia base. This displacement is imposed as

$$\vec{X}_b(s,t) = \vec{X}_{b0}(s,t) + A_c \frac{\vec{X}_{b0}(s,t)}{L_c/2} \sin\left(2\pi \hat{f}_{substrate} t\right). \tag{5.3}$$

$\vec{X}_b(s,t)$ is the position of the control point at the base of each cilium, $\vec{X}_{b0}(s,t)$ is the neutral position of that control point, $L_c = 4\times10^{-4} m$ is the full length of the cilia bed, $\hat{f}_{substrate}$ is the stretching frequency imposed on the substrate and A_c is the stretching amplitude.

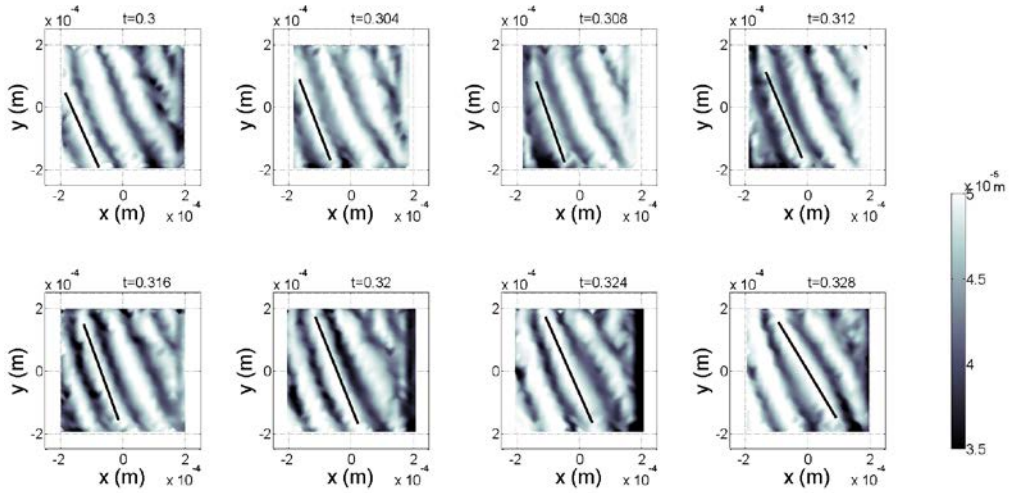

Figure 5.8 This figure shows the progression of a wave front on a cilia substrate subjected to cyclic stretching. A representative wave front is indicated by the solid black line. The cyclic stretching takes place in the direction parallel to the forward stroke. The natural frequency of the cilia is $\hat{f}_0 = 47.2Hz$ while the cyclic stretching frequency is $\hat{f}_{substrate} = 35Hz$. The stretching strain is $\varepsilon = 0.06$. One cycle of the imposed cyclic stretching is shown.

Also, we define the stretching strain ε as

$$\varepsilon = \frac{A_c}{L_c / 2}. \tag{5.4}$$

Figure 5.8 shows the metachronal wave fronts for a case where the cyclic stretching frequency $\hat{f}_{substrate}$ is imposed at $35Hz$. In comparison, the natural frequency of the cilia $\hat{f}_0$ is $47.2Hz$; the stretching strain is $\varepsilon = 0.06$. In this instance we note that metachronal waves are present and are not disrupted by the presence of cyclic stretching.

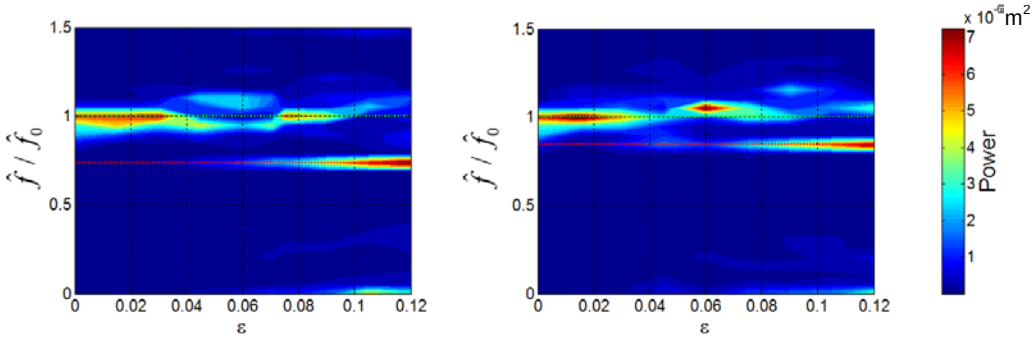

(a) (b)

Figure 5.9 Spectra amplitudes at varying magnitudes of stretching strain ε are shown. In (a), a cyclic stretching frequency of $\hat{f}_{substrate} = 35Hz$ is imposed, while in (b), a cyclic stretching frequency of $\hat{f}_{substrate} = 40.2Hz$ is imposed. In both cases, the dominant frequency at low stretching strains is $\hat{f} / \hat{f}_0 = 1$, which corresponds to the natural frequency of the beating cilia. At high stretching strains where $\varepsilon > 0.1$, the dominant frequencies correspond to the cyclic stretching frequencies of $\hat{f} / \hat{f}_0 = 0.74$ in the case of (a) and $\hat{f} / \hat{f}_0 = 0.85$ in the case of (b), i.e. $\hat{f} / \hat{f}_{substrate} = 1$ in both cases.

Next, we vary the stretching strain amplitude at two frequencies: $\hat{f}_{substrate} = 35Hz$ and $\hat{f}_{substrate} = 40.2Hz$. By performing FFTs on the kymographs, we obtain the spectra at each value of stretching strain ε. The spectrum amplitudes are shown in Figure 5.9, where the normalized spectra $\hat{f} / \hat{f}_0$ are plotted against stretching strain ε.

We observe that at low stretching strains the dominant frequency is the natural frequency of the cilia, i.e. $\hat{f} / \hat{f}_0 = 1$. At higher stretching strains where $\varepsilon > 0.1$, the metachronal waves become disrupted by the cyclic stretching, and hence the dominant frequencies become the cyclic stretching frequencies, i.e. $\hat{f} / \hat{f}_{substrate} = 1$. We obtain $\hat{f} / \hat{f}_0 = 0.74$ when $\hat{f}_{substrate} = 35Hz$ and $\hat{f} / \hat{f}_0 = 0.85$ when $\hat{f}_{substrate} = 40.2Hz$.

We therefore conclude in this section that the metachronal waves generated in our model are resistant to substrate deformations in the form of cyclic

stretching when stretching amplitudes are low. However at high stretching amplitudes, we observe that the metachronal waves become disrupted and the dominant frequencies become the imposed stretching frequencies.

5.5 The sideways sweep motion of cilia is necessary to generate metachronal wave fronts

In this section, we briefly investigate the contribution of the sideways sweep motion imposed on the cilia to the formation of metachronal waves. As indicated in equations 3.33 and 3.34, the sideways sweep motion is imposed by virtue of the two components α and β. α represents the magnitude of a triangular load in the $z-$direction imposed during the forward stroke. β represents the magnitude of a triangular load in the $y-$direction imposed during the reverse stroke. α attempts to confine the cilia forward stroke to a plane. It also serves to accentuate the sideways motion of the cilia during the reverse stroke by returning the cilia to the plane of its forward stroke. β gives the cilia its sideways motion. By changing the parameters α and β, we can observe the effects of the sideways motion on the formation of metachronal waves.

Figure 5.10 displays the kymographs of cases where α is varied with values of (a) $\alpha = 0$, (b) $\alpha = 1$, (c) $\alpha = 2$ and (d) $\alpha = 4$. We observe that when $\alpha = 0$, no metachronal waves are formed. Between 1 and $\alpha = 4$, we observe robust formation of metachronal waves.

Figure 5.11 displays the kymograph of a case where $\beta = 0$ is imposed at $t = 0.15s$. We observe that when $\beta = 0$, the cilia do not display a sideways sweep motion and the lateral coupling of cilia oscillations is absent. Consequently, for $t > 0.15s$, metachronal waves do not form.

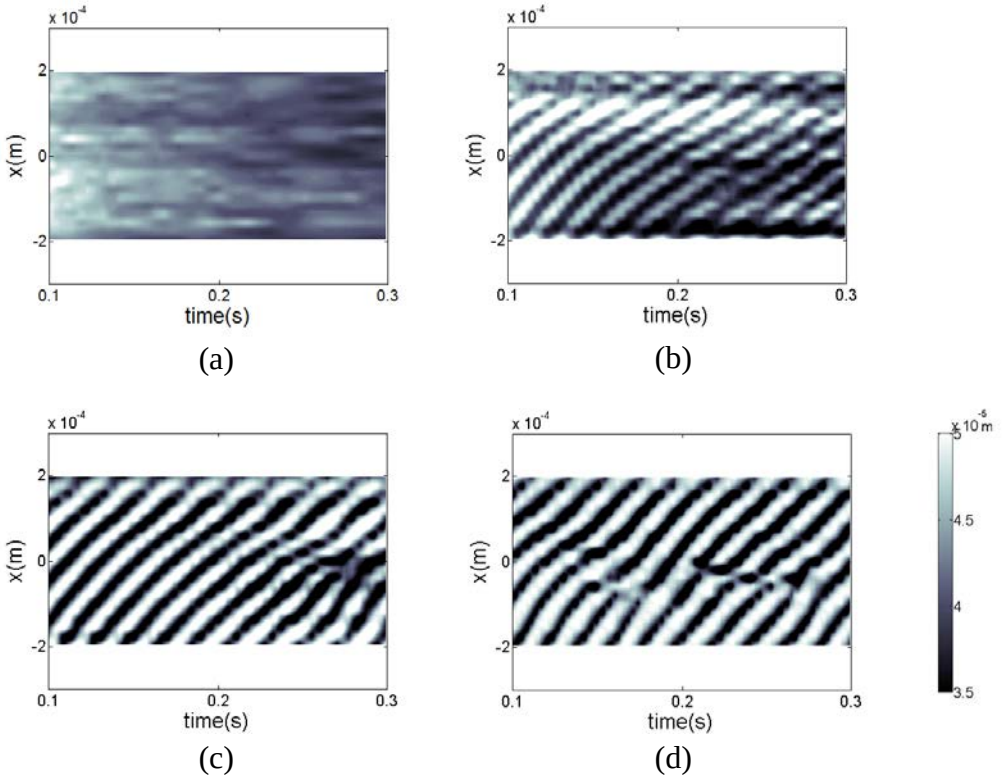

Figure 5.10 This figure shows the effect of α on metachronal waves. As α is increased through (a) $\alpha = 0$, (b) $\alpha = 1$, (c) $\alpha = 2$ and (d) $\alpha = 4$, metachronal waves form and become robust.

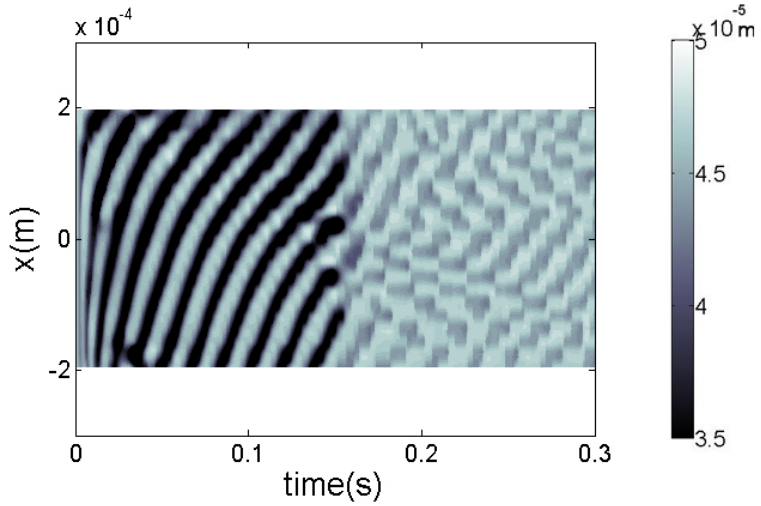

Figure 5.11 The kymograph of a case where $\beta = 0$ is imposed at $t = 0.15s$ is shown. It is observed that when $\beta = 0$, the metachronal wave fronts are disrupted.

We therefore conclude that both the planar motion (as determined by α) and the sideways sweep motion (as determined by β) of the cilia are necessary for the formation of metachronal wave fronts.

5.6 Metachronal waves can form when the cilia array is irregular

In this section, we briefly investigate the effect of cilia arrangement on metachronal wave formation. In the case of *Paramecium*, cilia arrangement is known to be highly regular. This is evident from images of basal bodies found on *Paramecium* [122]. We now investigate metachronal wave formation and propagation in a case where cilia arrangement is irregular.

We generate an irregular cilia array by first constructing a 2D, unstructured mesh on the substrate. This mesh is situated in the range of $-2\times10^{-4}m \le x \le 2\times10^{-4}m$ and $-2\times10^{-4}m \le y \le 2\times10^{-4}m$. A Delaunay triangulation algorithm is used in the triangulation of this mesh. The cell vertices in the mesh are then used to determine the locations of cilia. This method of generating the cilia bed enables the cilia spacing to be highly similar but yet causes the arrangement of cilia to be irregular. This cilia arrangement is shown in Figure 5.12(a). Compared to the case of a 21×21 cilia array with a total of 441 cilia, this irregular cilia array presents a total of 479 cilia.

The kymograph from this irregular cilia array is shown in Figure 5.12(b). It can be seen that although the cilia arrangement is irregular, metachronal wave fronts are still formed. We conducted further simulations where the irregular cilia array is rotated by $\pi/2$, π and $3\pi/2$ radians. In each of these instances, metachronal waves are observed.

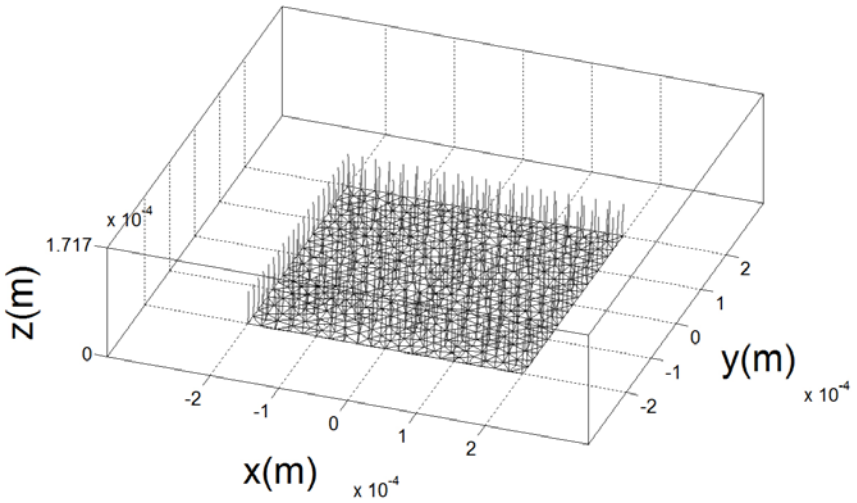

(a)

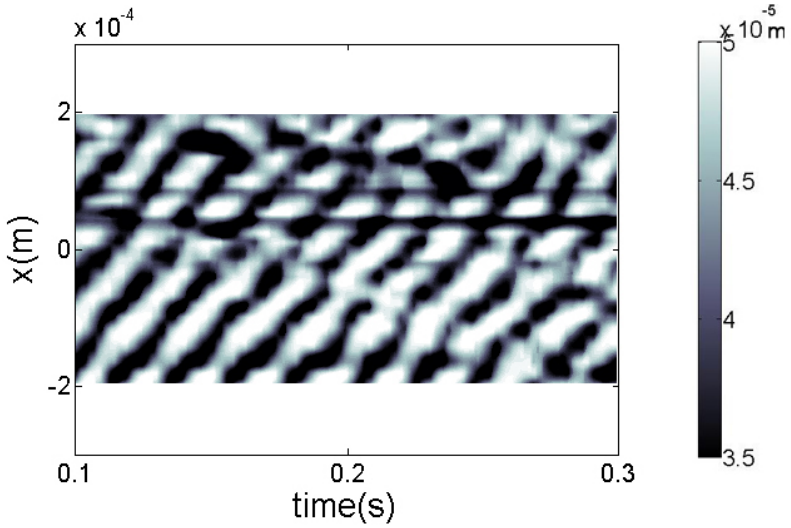

(b)

Figure 5.12 (a) This figure shows an irregular cilia array. The cilia are located at vertices of an unstructured mesh generated by a Delaunay triangulation algorithm. The mesh is shown on the substrate. (b) The kymograph from the unstructured cilia array is shown. Despite the unstructured arrangement of cilia, metachronal waves are observed.

We therefore conclude in this section that since formation of metachronal waves over an irregular array are observed, metachronal wave formation in our model is robust against cilia arrangement.

5.7 Cilia array is large enough to represent an infinite array

Although our cilia array is finite in size, the fluid quantities at the array centre are a fairly good representations of that of an infinite array. We show this by comparing fluxes through the walls of a rectangular column located approximately at the array centre. This column encloses 9 cilia and is chosen to represent a unit cell of cilia arrangement. We show that since flow quantities across opposite faces of this column are similar, this unit cell is thus a repeatable unit and hence encloses a representative flow field of an infinite cilia array.

This column is shown in Figure 5.13(a). In this figure, the case where $\mu_2 / \mu_1 = 6$ and $\sigma = 0.0025 Nm^{-1}$ at $t = 0.3s$ is shown. We denote flow quantities passing through the blue, cyan, red and green walls with subscripts x^-, x^+, y^- and y^+ respectively.

The time-averaged velocities normal to the column walls are shown in Figure 5.13(b). Figures 5.13(b)(i) and (ii) show contours of $\left(\vec{u} \cdot \vec{n}\right)_{x^+}$ and $\left(\vec{u} \cdot \vec{n}\right)_{x^-}$, while Figures 5.13(b)(iii) and (iv) show contours of $\left(\vec{u} \cdot \vec{n}\right)_{y^+}$ and $\left(\vec{u} \cdot \vec{n}\right)_{y^-}$. We observe that contours of $\left(\vec{u} \cdot \vec{n}\right)_{x^-}$ and $\left(\vec{u} \cdot \vec{n}\right)_{x^+}$ are highly similar, and contours of $\left(\vec{u} \cdot \vec{n}\right)_{y^-}$ and $\left(\vec{u} \cdot \vec{n}\right)_{y^+}$ are likewise highly similar.

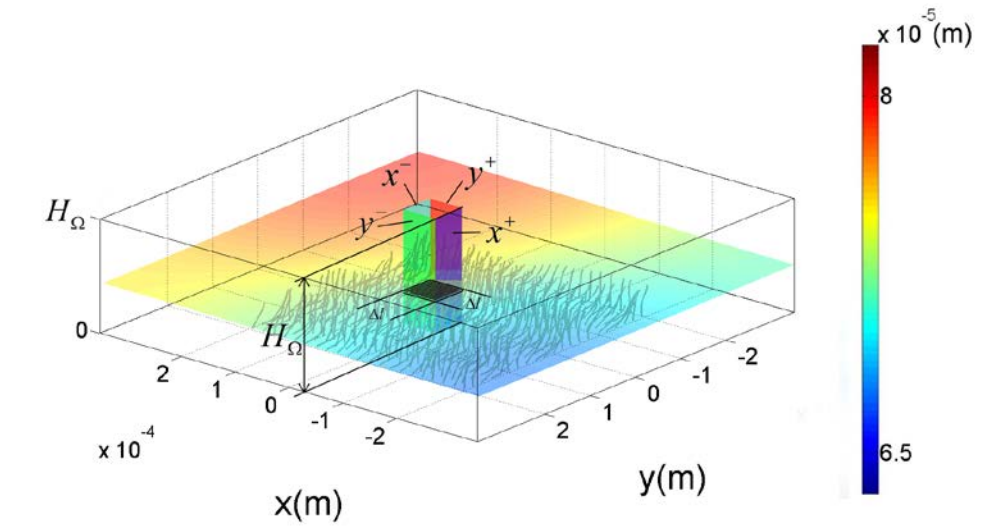

(a)

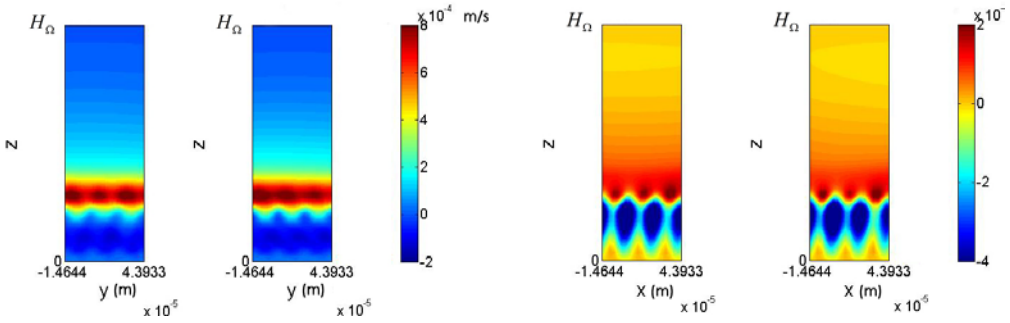

(i) (ii) (iii) (iv)

(b)

Figure 5.13 (a) A schematic of a two-fluid configuration is shown. The fluids are separated by a horizontal interface colour-coded by interface height above the substrate. H_Ω is the height of the channel. We isolate a square column in the center of our cilia array. The fluxes through the walls of the centre column are used to calculate the average bulk flow velocities, and the cross-sectional area of the column at the height of cilia tips (grey square of side Δl) is used to calculate average slip velocities. (b) Velocity contours of (i) $\vec{u}\cdot\vec{n}_{x^-}$ and (ii) $\vec{u}\cdot\vec{n}_{x^+}$ are shown. The contours are similar, indicating that flow profiles through the faces denoted x^- and x^+ are highly similar. Likewise, velocity contours of (iii) $\vec{u}\cdot\vec{n}_{y^-}$ and (iv) $\vec{u}\cdot\vec{n}_{y^+}$ are highly similar.

To quantify how similar these contours are, we calculate the root mean square differences between $(\vec{u}\cdot\vec{n})_{x^+}$ and $(\vec{u}\cdot\vec{n})_{x^-}$, rms_{x^-,x^+}, as

$$rms_{x^-,x^+} = \sqrt{\frac{1}{A}\int\left[\left(\vec{u}\cdot\vec{n}\right)_{x^+} - \left(\vec{u}\cdot\vec{n}\right)_{x^-}\right]^2 dA}\,. \tag{5.5}$$

Similarly, we calculate the root mean square differences between $\left(\vec{u}\cdot\vec{n}\right)_{y^+}$ and $\left(\vec{u}\cdot\vec{n}\right)_{y^-}$, rms_{y^-,y^+}, as

$$rms_{y^-,y^+} = \sqrt{\frac{1}{A}\int\left[\left(\vec{u}\cdot\vec{n}\right)_{y^+} - \left(\vec{u}\cdot\vec{n}\right)_{y^-}\right]^2 dA}\,. \tag{5.6}$$

We normalize the root mean square differences by the maximum velocities through the faces, namely

$$\left\langle rms_{x^-,x^+}\right\rangle = \frac{rms_{x^-,x^+}}{\max\left[\left|\left(\vec{u}\cdot\vec{n}\right)_{x^+}\right|,\left|\left(\vec{u}\cdot\vec{n}\right)_{x^-}\right|\right]}, \tag{5.7}$$

and

$$\left\langle rms_{y^-,y^+}\right\rangle = \frac{rms_{y^-,y^+}}{\max\left[\left|\left(\vec{u}\cdot\vec{n}\right)_{y^+}\right|,\left|\left(\vec{u}\cdot\vec{n}\right)_{y^-}\right|\right]}\,. \tag{5.8}$$

We consider these quantities a relative measure of difference in flux over opposite walls. We find that $\left\langle rms_{x^-,x^+}\right\rangle = 0.0214$ and $\left\langle rms_{y^-,y^+}\right\rangle = 0.0244$. We consider these quantities to be adequately small, and thus conclude that the fluxes across opposite walls of the column to be similar.

For the case where only a single fluid is present, we report values of $\left\langle rms_{x^-,x^+}\right\rangle = 0.0311$ and $\left\langle rms_{y^-,y^+}\right\rangle = 0.0219$.

The similarity in fluxes across the column is an indication that this column can be approximated as a repeatable unit. We therefore conclude in this section that when flow quantities in our simulations are taken across the central

column indicated in Figure 5.13(a), the flow quantities are a reasonably good approximation of the flow quantities over an infinite cilia array.

6 Parametric study of fluid transport in cilia model

6.1 Effect of cilia model parameters on metachronal wave propagation and fluid transport

In this chapter, we shall systematically study the effects of parameters in our cilia model on metachronal wave formation and fluid transport.

In Section 6.2, we investigate the effects of cilia bending stiffness and cilia number density on metachronal wave propagation. We find that in the regime where cilia possess low bending stiffness, active forces in the cilia are balanced mainly by fluid viscous forces; hence bending stiffness does not play a significant role in affecting metachronal wave propagation. We find that this regime corresponds closely to the bending stiffness of natural cilia.

In Section 6.3, we show the existence of an optimal cilia number density which gives a maximum fluid slip velocity at the cilia tips. We find that this cilia density matches the cilia densities observed in nature to give optimized bulk fluid transport efficiencies. This cilia density matches that observed in *Paramecium*, but is lower than that observed in the human respiratory system.

In Section 6.4, we briefly present a special case where the normalized cilia spacing is $d / L = 1.44$. We qualitatively compare the observed features in our simulated velocity field with that presented by Ding et al. [127]. We show that our simulated flow field has similar features and characteristics with that presented by Ding et al.

In Section 6.5, we examine the trajectories of particles suspended in the fluid. These particles are passively advected with the fluid. We find that when particles are embedded within the cilia array, their trajectories resemble that of

particles undergoing diffusion, and when particles are embedded above the cilia array, their trajectories resemble that of particles undergoing advection.

6.2 Effect of cilia bending stiffness and number density on metachronal wave properties

In this section, to study the factors that govern the speed of the metachronal waves, we systematically vary several parameters in our simulations: the bending stiffness of cilia from $EI = 6.90 \times 10^{-23} Nm^2$ to $EI = 1.38 \times 10^{-18} Nm^2$ and the cilia number density from $d^{-2} = 1.15 \times 10^9 m^{-2}$ to $d^{-2} = 4.06 \times 10^9 m^{-2}$. Here, d is the distance between adjacent cilia. We observe that for bending stiffness below $EI = 6.90 \times 10^{-21} Nm^2$, bending stiffness has little effect on cilia motion as both the viscous effects and the active force effects acting on the cilia are much greater than the bending stiffness.

By following the steps mentioned in Section 5.2 and performing discrete fast Fourier transforms on the kymographs, we are able to extract the magnitude of wave vector in the direction of wave travel, $|k|$, and the frequency, $\hat{f}$, of the waves. Incidentally, we also find that $\hat{f}$ matches the frequency of the individual cilium as it cycles through its motion.

These results are summarized in Figure 6.1. From panel Figure 6.1(a), we see that, as cilia number density increases from $d^{-2} = 1.15 \times 10^9 m^{-2}$ to $d^{-2} = 4.06 \times 10^9 m^{-2}$, the metachronal wave frequency $\hat{f}$ is reduced. We attribute this behavior to the fact that as cilia number density increases, the gaps between adjacent cilia are narrowed. The fluid between the increasingly narrow gaps experiences high shear stresses as the cilia deform. The fluid is then a source of resistance to the motion of the cilia. This resistance opposes the active force, $\vec{f}_{active}$, hence reducing the net active force on the cilia. The reduction in net active force results in slower cilia motion, therefore causing a

reduction in the frequency of the cilia. Consequently, a lower frequency of the metachronal wave is observed.

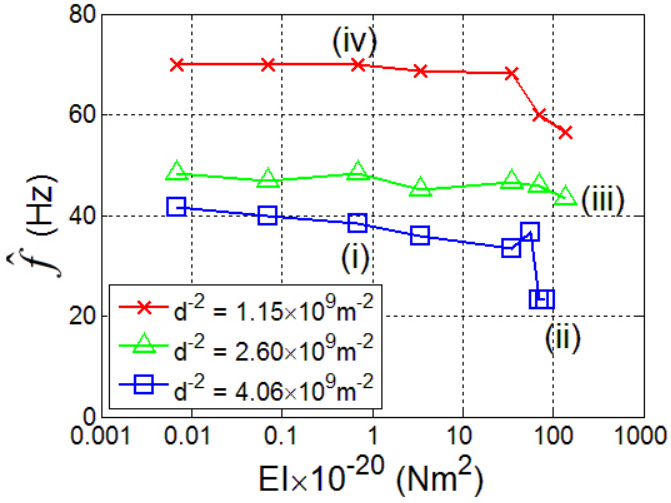

(a)

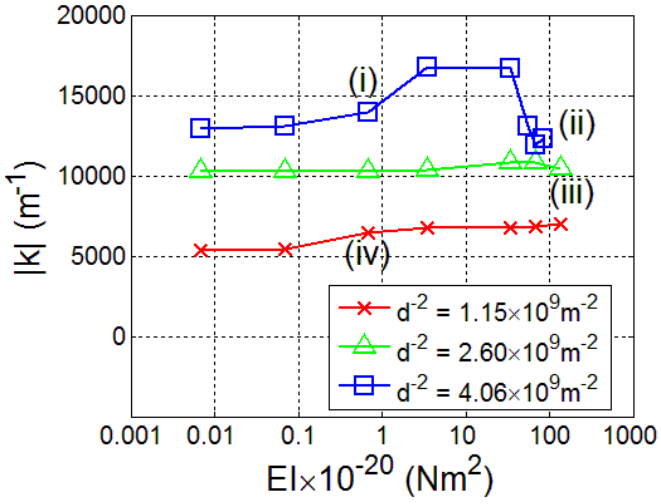

(b)

Figure 6.1 (a) Variation of metachronal wave frequency $\hat{f}$ with cilia bending stiffness EI is shown. (b) Variation of metachronal wave vector magnitude $|k|$ with cilia bending stiffness EI is shown.

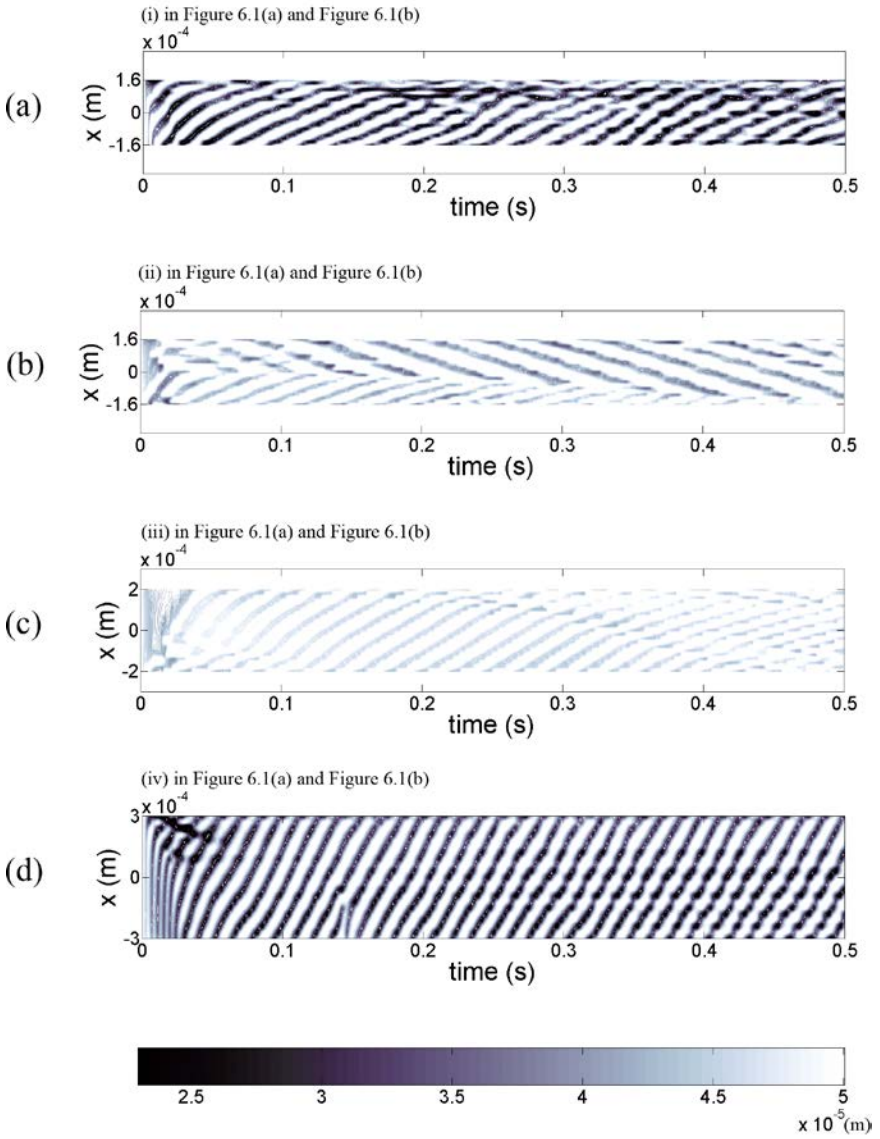

Figure 6.2 This figure shows variations of cilia tip heights in time for the following scenarios: (a) $EI = 6.90\times10^{-21}\,Nm^2$ and $d^{-2} = 4.06\times10^{9}\,m^{-2}$, (b) $EI = 8.27\times10^{-19}\,Nm^2$ and $d^{-2} = 4.06\times10^{9}\,m^{-2}$, (c) $EI = 1.38\times10^{-18}\,Nm^2$ and $d^{-2} = 2.60\times10^{9}\,m^{-2}$ and (d) $EI = 6.90\times10^{-21}\,Nm^2$ and $d^{-2} = 1.15\times10^{9}\,m^{-2}$. (a), (b), (c) and (d) are correspondingly marked as (i), (ii). (iii) and (iv) in Figures 6.1(a) and (b). In all four scenarios, slices at mid plane $y = 0$ are shown.

Next, we observe that the bending stiffness of the cilia, EI, does not significantly affect the metachronal wave frequency $\hat{f}$ when $EI < 10^{-19}\,Nm^2$. However, for large bending stiffness where $EI > 10^{-19}\,Nm^2$, increasing EI results in a decrease in $\hat{f}$. This is attributed to the increasing resistance to cilia motion from increased stiffness. In our model, increased stiffness will

similarly reduce the net active force on the cilia, hence reducing the wave and cilia frequencies. This is evident from the contour plots in Figures. 6.2(b) and (c), where the light contours indicate only slight deformations of stiff cilia. However, in the regime where bending stiffness of the cilia is small, the active force on the cilia is mainly balanced by the viscous drag from the fluid, resulting in a situation where bending stiffness does not affect the cilia motion. We believe this is also the regime where natural cilia operates, as measurements by Gittes et al. [128] have shown that the bending stiffness of singular microtubules are in the range of $EI \sim 10^{-24} - 10^{-23} Nm^2$.

Figure 6.1(b) shows the variations of the magnitude of wave vector in the direction of wave travel, $|k|$, vs. EI. It can be seen that as cilia number density increases, there is a corresponding increase in $|k|$. Increase in bending stiffness does not have a significant change in $|k|$ for cilia number densities of $d^{-2} = 1.15 \times 10^9 m^{-2}$ and $d^{-2} = 2.60 \times 10^9 m^{-2}$. However we observe that for a cilia number density of $d^{-2} = 4.06 \times 10^9 m^{-2}$ at high stiffness, symplectic metachronal waves become unstable and antiplectic waves momentarily form (Figure 6.2(b)). At $EI \sim 10^{-18} Nm^2$, metachronal waves of low amplitudes are formed. These waves eventually display discontinuous crests and troughs and are unable to transverse the entire cilia bed (Figure 6.2(c)).

By comparing Figures 6.2(a) and (d), we observe that wave fronts in Figure 6.2(a) display lower gradients than wave fronts in Figure 6.2(d). This suggests that as cilia number density decreases, metachronal wave velocity increases. This observation is reinforced by Figure 6.1(a) and (b). We observe that as d^{-2} is decreased, $\hat{f}$ is increased. This is accompanied by a decrease in $|k|$ and hence an increase in wavelength λ. Since metachronal wave speed $c = \hat{f}\lambda$, we can conclude that as cilia number density d^{-2} decreases, metachronal wave speed increases.

It is evident in our simulations that cilia spacing and stiffness play a role in the metachronal wave characteristics. Our results show large values of the cilia

stiffness, EI, reduce the frequency and amplitude of metachronal waves. Antiplectic metachronal waves are abundant in nature. It happens, for example, over the cilia of *Paramecium*. We find that antiplectic metachronal waves can be produced when cilia stiffness is taken into account. However, our results show that antiplectic waves occur when cilia bending stiffness is several orders of magnitude larger than those found in nature. It is therefore likely another mechanism besides cilia stiffness is responsible for the production of antiplectic waves in natural biological systems.

In this section, we conclude that the metachronal wave characteristics of wave vector magnitude $|k|$, frequency $\hat{f}$, and wave speed are functions of cilia stiffness EI and cilia number density d^{-2}. Also, we show that cilia that are too stiff cannot support the propagation of metachronal waves.

6.3 There exists an optimal cilia number density for maximum slip velocity

The flow field around a large cilia bed is often complex and difficult to resolve. One simple way to treat the flow field around a cilia bed is to assume that the cilia tips form a rigid wall but with a non-zero slip velocity boundary condition. We hereby attempt to quantify the slip velocities at the cilia tips in our simulations.

Figure 6.3(a) shows the average forward-stroke component of the velocity profiles in the chamber with a cilia number density of $d^{-2} = 2.60 \times 10^{9} m^{-2}$. The average velocity profile for each value of cilia stiffness is obtained by averaging the velocities across a chosen area A at various heights z above the chamber floor. The average velocity at a particular z is calculated as

$$\langle u \rangle = \frac{1}{T\left(\Delta l^2\right)} \iint u_z dt d\left(\Delta l^2\right), \tag{6.1}$$

where Δl^2 is an area parallel to the *x*-*y* plane centered on the area occupied by the cilia bed (shaded grey in Figure 5.13(a)), u_z is the $x-$component of velocity at a particular height z above the chamber floor, and T is a time interval large enough such that $\langle u \rangle$ does not vary with T. Here, $T = 0.6s$.

We observe that the velocity profiles display qualitatively the same features as described experimentally by Shields et al. [28]. These features consist of a parabolic profile above the cilia tips which included a recirculation region near the chamber ceiling, and a maximum velocity magnitude at the cilia tips which resembles a sliding plane boundary condition in Poiseuille-Couette flow. In other words, the cilia bed can be replaced by a boundary with a non-zero slip velocity. We now proceed to quantify this slip velocity.

We note that the average velocity profiles become less pronounced for higher cilia stiffness. This is because as the stiffness of each cilium is increased, the deformations of the cilium are reduced. This causes a reduction in cilium oscillation amplitude and hence a reduction in the amount of fluid the cilium pumps with each cycle. Collectively, lesser fluid is pumped by the cilia bed and therefore average velocity profiles become less pronounced.

Figure 6.3(b) shows the magnitude of slip velocities for different cilia densities. Slip velocities are given as

$$U_{slip} = \langle u \rangle_{z=L} \ . \tag{6.2}$$

We observe that for small values of cilia stiffness where $EI < 6.90 \times 10^{-21} Nm^2$, EI does not affect the slip velocity. However as EI increases, the slip velocity decreases. This is because cilia with high bending stiffness are resistant to deformation and do not pump fluid effectively.

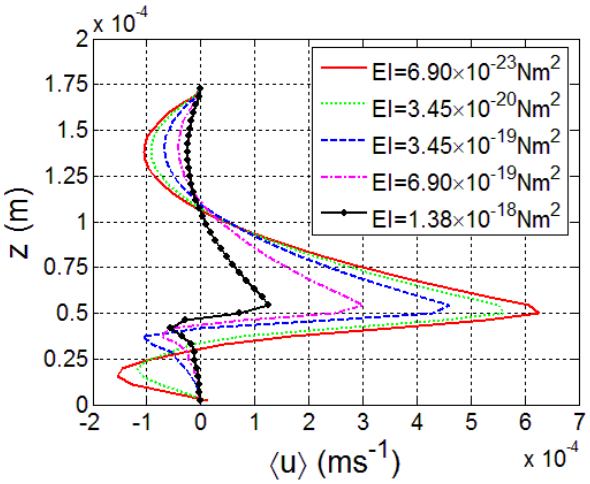

(a)

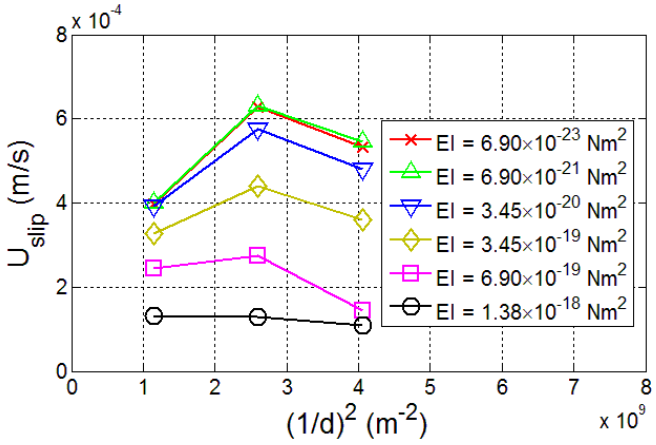

(b)

Figure 6.3 (a) Profile of $\langle u \rangle$, the component of velocity in the forward stroke as defined in equation 6.1, for different cilia stiffness at fixed number density $d^{-2} = 2.60 \times 10^{9} m^{-2}$. (b) Slip velocity at cilia tip, as defined in equation 6.2, vs. cilia number density for various EI.

We observe that a cilia number density of $d^{-2} = 2.60 \times 10^{9} m^{-2}$ generally gives the highest slip velocity. This shows the existence of an optimum cilia number density which gives the highest slip velocity.

We suggest a mechanism that accounts for the existence of this optimum. As cilia number density increases over the optimum, the narrower fluid gaps in

between cilia impose higher shear drag on the cilia during cilia motion, thus reducing the pumping efficiency of the cilia bed. Also, as cilia number density decreases, the larger fluid gaps between cilia form regions where fluid is not actively propelled by cilia, hence reducing the average slip velocity.

In our simulations, a reduction in U_{slip} occurs at a cilia spacing of $d = 0.3L$. Osterman and Vilfan [61] reported a reduction in cilia pumping efficiency for $d < 0.25L$. Excellent electron microscopy images of *Paramecium* by Allen [129] show the distance of cilia on the surface are separated by $d \sim 1\mu m$. Assuming a cilia length of $L = 5\mu m$, we obtain $d \sim 0.2L$. However, Carson et al. [130] studied the formation of cilia in the human nasal epithelium and report an average inter-cilia spacing of $0.41\mu m$. Again assuming $L = 5\mu m$, we obtain $d \sim 0.1L$. This suggests cilia spacing in the nasal epithelium is too small to be optimized. However, we note that cilia in the respiratory tract are surrounded by a complex arrangement of fluids. These fluids consist of a Newtonian-like periciliary layer below a viscoelastic mucus layer. The dynamics of cilia in this environment is therefore highly complex and more work is required to understand the dynamics of such a system.

The existence of an optimum cilia spacing was also reported by Elgeti and Gompper [88]. However, this optimum was not observed by Lee et al. [50] or by Khaderi and Onck [46]. Jayathilake et al. [52] simulated conditions where a 2D cilia array was made less dense due to the presence of immotile cilia. Likewise, no optimum cilia density was observed. We note here that Elgeti and Gompper used a model where metachronal waves were spontaneously generated, while the latter authors used models where metachronal waves were imposed.

It is well known that cilia in the respiratory tract may be damaged by the presence of inhaled pollutants. For example, research on mouse models showed prolonged exposure to cigarette smoke reduces cilia beat frequency and results in shedding of cilia and loss of ciliated epithelial cells [131]. Our results in this section indicate that as cilia number density decreases beyond

the optimum, there is a drop in slip velocity. This indicates that advection velocities of particles above the cilia tips are reduced, thereby having a negative impact on the functioning of the respiratory system.

Primary cilia dyskinesia (PCD), formerly known as immotile cilia syndrome, is a disorder where cilia become immotile or possess abnormal beat patterns. These conditions and effects have been simulated in [52]. A reduction in the number of active cilia, or a reduction in the number of properly functioning cilia, will result in a cilia array that is less dense, thereby leading to airway infections, coughs, respiratory distress and failure. In addition, PCD associated with cilia in the embryo node may result in congenital heart diseases in individuals [132].

In this section, we conclude that we have investigated the effects of cilia stiffness EI and cilia number density d^{-2} on cilia slip velocity. We have shown the existence of an optimal cilia number density and suggested a reason for the optimum. Cilia in high densities are subjected to large shear stresses from narrow fluid gaps between cilia, thus lowering the slip velocity. Cilia in low densities have large regions of undriven fluid between them, thus lowering the slip velocity.

6.4 Salient features in flow field are consistent with that observed in literature

We next qualitatively compare the flow field generated by our model with that observed in literature. For this, we choose the flow field obtained by Ding et al. [126] as a basis for comparison. In this single-fluid simulation, we set $d/L = 1.44$ as per [126], otherwise the simulation parameters are as listed in Table 3.1.

It should be noted that Ding et al. simulated an infinite cilia array by imposing periodic boundary conditions on the fluid domain, while our fluid domain is bounded by no-slip walls. In addition, Ding et al. used a different model where

realistic, planar beat motions are imposed on the cilia. However, we shall show that, in spite of our simplified forcing function, the salient features in the flow field generated by our model is similar to that by Ding et al.

The time-average flow field from our simulation is shown in Figure 6.4. Here, the average velocity field is given by

$$\langle \vec{u} \rangle = \frac{1}{T} \int_0^T \vec{u} dt \tag{6.3}$$

We note the presence of 3 major flow features; the first is a strong vortex to the left of each cilium, the second is a region of maximum flow above the cilia tips, and the third is a vortex above and between cilia. These features are shown in Figure 6.4.

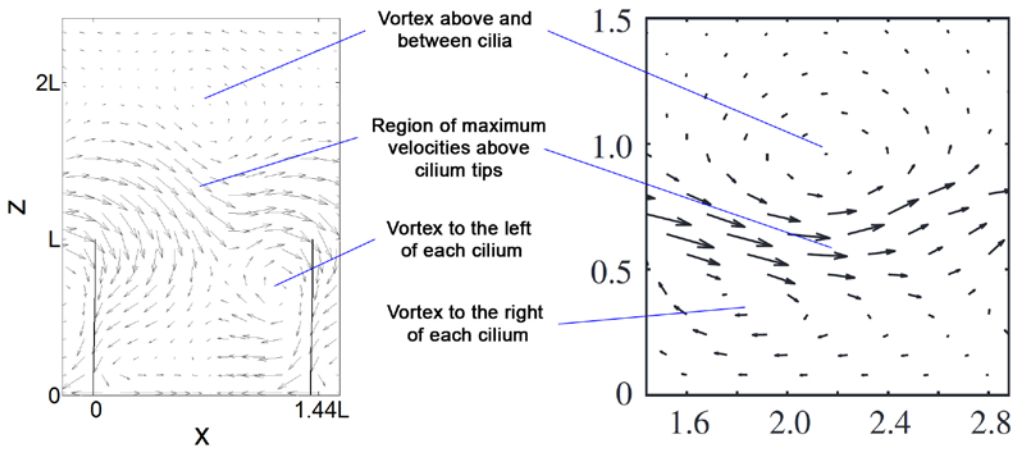

(a) (b)

Figure 6.4 (a) A vector plot of the averaged fluid velocity field from our simulation is shown. (b) The velocity displacement field of the fluid generated by cilia undergoing symplectic metachrony is shown. (b) is reproduced from Ding et al. [127].

Simulations of symplectic metachronal waves by Ding et al. similarly show a vortex in the vicinity of each cilium. However, the location of the vortex is to the right of each cilium. This difference can be attributed to the differences in

forcing functions. While Ding et al. imposed an asymmetry between the forward and reverse strokes, our simulations imposed a symmetric forcing function in the direction parallel to metachronal wave propagation. This can be seen in equations 3.33 and 3.34, where the force components in the $x-$ direction for both the forward and reverse strokes are identical.

Simulations by Ding et al. show a region of maximum flow above and around the cilia tips. This region displays a "wavy" structure; the velocity vectors dip downward in between cilia and turn upward as they approach cilia tips. Our simulations similarly show such a region. Our region of maximum fluid velocity is thicker than that shown by Ding et al.

Simulations by Ding et al. also show vortices in between cilia. These vortices are located at the heights of cilia tips, i.e. $h \approx L$. In our simulations, we similarly observe vortices in between cilia; however our vortices are located above the cilia tips and are located at approximately $h \approx 2L$.

We therefore conclude in this section that although our cilia model is simple, it can reproduce, albeit with differences, the salient flow features commonly observed in cilia simulations.

6.5 Transport of particles about the cilia bed displays both diffusive and advective behaviors

To study the transport properties of fluid around a cilia bed, we place massless, passive tracer particles in the chamber and track their motion with time. These particles exert no forces and therefore do not have any effect on fluid motion. These particles are advected in a manner identical to the cilia control points. Their velocities are interpolated from the fluid grid using equations 3.38 and 3.39. Figure 6.5(a) shows typical particle trajectories projected onto the x-z plane for a simulation with cilia number density of $d^{-2} = 2.60 \times 10^{9} m^{-2}$ and $EI = 3.45 \times 10^{-20} Nm^{2}$. It is observed that particles

below and around the cilia tips display spiral trajectories while particles far above the cilia tips display linear trajectories.

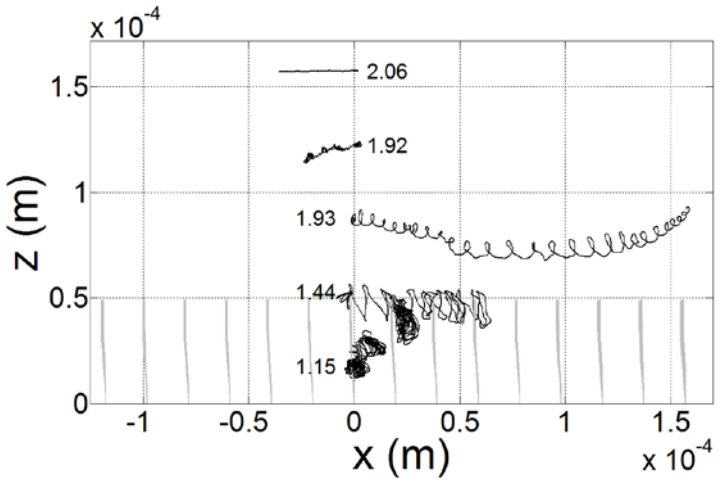

(a)

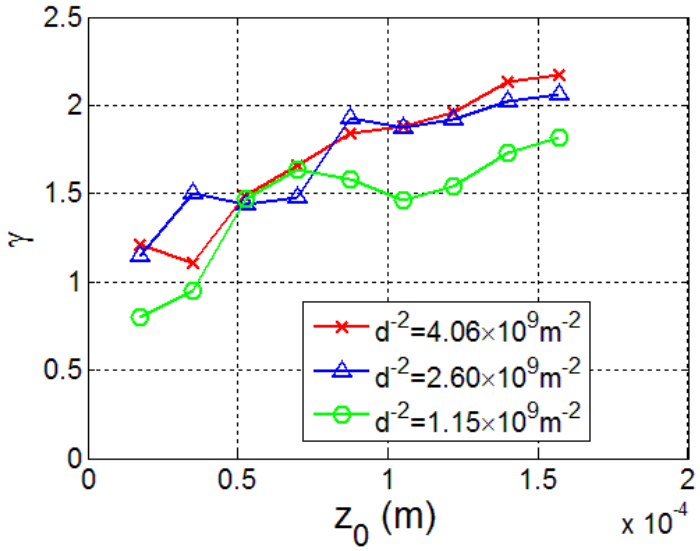

(b)

Figure 6.5 (a) Particle trajectories projected onto the *x*-*z* plane for particles seeded at different initial heights are shown. Here, the cilia number density is $d^{-2} = 2.60\times10^{9}\,m^{-2}$ and the cilia stiffness is $EI = 3.45\times10^{-20}\,Nm^{2}$. The numbers next to the trajectories indicate γ as defined in equation 6.4. (b) The exponent γ vs. initial height of tracer particle for various cilia number densities is shown.

We calculate the least squares linear fit for the mean square displacement of the tracer particles, $\log\left|\vec{X}\right|^2$ vs $\log\tau$, to obtain the gradient γ:

$$\log\left|\vec{X}\right|^2 \propto \gamma \log\tau \,. \tag{6.4}$$

Here, τ is the time taken for the average particle to travel a displacement $\left|\vec{X}\right|$. A value of $\gamma = 1$ indicates diffusive behavior of the particles and a value of $\gamma = 2$ indicates advective, or ballistic, behavior of the particles.

It should be emphasized that diffusion here refers to the scalar diffusion of a secondary phase within the bulk fluid. The continuum form of the diffusion-advection equation is

$$\frac{\partial\Phi}{\partial t} + \left(\vec{u}\cdot\vec{\nabla}\right)\Phi = \vec{\nabla}\cdot\left(D\vec{\nabla}\Phi\right) \,, \tag{6.5}$$

where Φ represents the concentration of the secondary phase. The term $\left(\vec{u}\cdot\vec{\nabla}\right)\Phi$ is the convection term, where viscous effects are included in the solution of $\vec{u}$. The second term $\vec{\nabla}\cdot\left(D\vec{\nabla}\Phi\right)$ is the diffusion term.

In our implementation, the continuum secondary phase is instead represented by a set of discrete tracer particles. Should the effects of the diffusion term be included, we could include a Brownian motion model, where the particles are advected by an imposing an additional velocity above that by the fluid. However, we emphasize here that our model does not include any form of diffusion. Therefore in our simulations, a value of $\gamma = 1$ indicates that the particles are undergoing advection that mimics diffusion.

Figure 6.5(b) shows the variation of γ as a function of the initial height z_0 at which the particles are seeded. We observe that for cilia densities of

$d^{-2} = 1.15 \times 10^9 m^{-2}$ to $d^{-2} = 4.06 \times 10^9 m^{-2}$, there is no significant difference in transport behavior. Particles close to the chamber floor generally have $\gamma \sim 1$ while particles close to the chamber ceiling generally have $\gamma \sim 2$.

In addition, for the case where $d^{-2} = 2.60 \times 10^9 m^{-2}$, we report a normalized average transport velocity of $\frac{\langle u \rangle / L}{\hat{f}} = 0.04$. Here, $\langle u \rangle$ is the average velocity in the chamber in the $x-$direction. It is given as

$$\langle u \rangle = \frac{1}{2A} \int \left[\left(\vec{u} \cdot \vec{n} \right)_{x^+} + \left(\vec{u} \cdot \vec{n} \right)_{x^-} \right] dA \tag{6.6}$$

This value is comparable to the value of 0.063 calculated from data obtained from [51]. Here, the authors performed simulations with a similar setup, albeit with a chamber ceiling that is at $z = 4L/3$ and with a realistic cilia beat pattern.

We again note the complex fluid arrangements found in actual respiratory tracts. Particles above the cilia tips embedded in the mucus layer are actively pushed along while particles below the cilia tips are embedded in the periciliary layer and are advected less. Our results show that particles below the cilia tips have a tendency to be slowly advected upwards toward the cilia tips. This can be seen in Figure 6.5(a), where the particle closest to the chamber floor seeded at height of $1.74 \times 10^{-5} m$ displays a net upward spiraling motion. The flow conditions ensure particles close to the chamber floor eventually become embedded in the upper layers and are swept from the respiratory system. This phenomenon happens despite the net negative velocities close to the chamber floor (Figure 6.3(a)).

In this section, we observed the transport of passive tracer particles embedded in the fluid chamber. We show that particles close to the chamber floor exhibit diffusive behavior while particles close to the chamber ceiling display advective behavior. However, our model does not account for diffusive

effects. The trajectories displayed by tracer particles close to the chamber floor are therefore advective in nature; they are merely mimicking diffusive trajectories.

7 Simulations of a stratified two-fluid arrangement

7.1 Description of cilia model in stratified two-fluid arrangement

In this chapter, we investigate the effects of cilia in a stratified, two-fluid arrangement. This arrangement mimics the conditions in our respiratory system, where the cilia reside on a substrate and is immersed in a periciliary layer (PCL). The PCL is of thickness approximately that of the cilia length L. A mucus layer of thickness $\sim 30L$ sits atop the PCL. Our model seeks to model this arrangement. Our model is shown in Figure 7.1(a). Here, the cilia reside on a substrate and are immersed in a lower fluid corresponding to the PCL. An upper fluid layer corresponding to the mucus sits atop the lower fluid.

In our model, we make a major simplification by modeling the mucus as a Newtonian fluid. Also, we keep the viscosity of the lower fluid constant at $\mu_1 = 1.0 \times 10^{-3} kgm^{-1}s^{-1}$.

In Section 7.2, we investigate the bulk flow of the fluid as it is propelled by the cilia. The fluid bulk flow is represented by $U_{\parallel}$ and $U_{\perp}$, which are respectively the cross-sectional average fluid velocity components parallel ($\parallel$) and perpendicular ($\perp$) to the cilia forward stroke in the flow chamber (Figure 7.1(b)). In our model, there exists a surface tension σ between the upper and lower fluids. We investigate the fluid bulk flow as a function of this surface tension. We also investigate the fluid bulk flow as a function of viscosity ratio between the upper and lower fluids μ_2 / μ_1. In our model, we show that increasing the surface tension has the effect of increasing the fluid bulk flow while increasing the viscosity of the upper fluid has the effect of decreasing the fluid bulk flow.

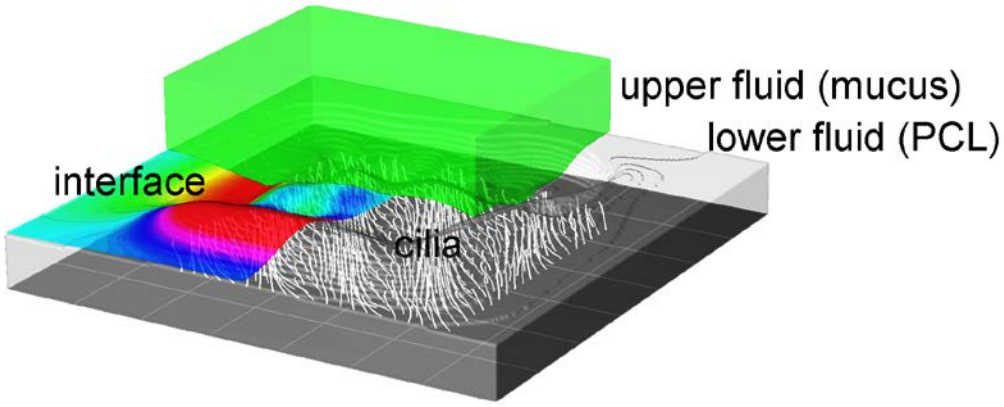

(a)

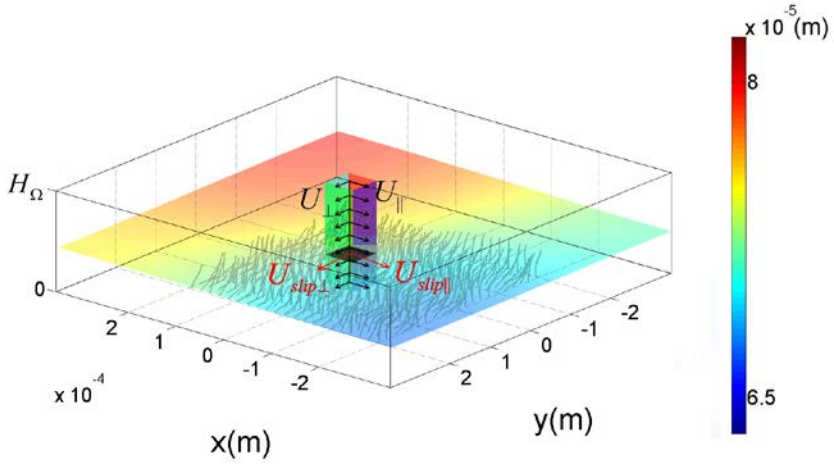

(b)

Figure 7.1 (a) This figure shows our cilia model in a stratified two-fluid arrangement. The model consists of an upper fluid which corresponds to the mucus layer and a lower fluid which corresponds to the periciliary layer (PCL). The cilia reside on a substrate and are immersed in the lower fluid. (b) This figure shows velocity components used in our study. $U_{\parallel}$ and $U_{\perp}$ are the averaged bulk flow velocities parallel and perpendicular to the cilia forward stroke. $U_{slip\parallel}$ and $U_{slip\perp}$ are the averaged velocities at the cilia tips parallel and perpendicular to the cilia forward stroke. The color bar indicates the height of the interface above the substrate.

In Section 7.3, we show that the presence of surface tension severely modifies the velocity profiles in the flow chamber. In particular, we show that the presence of surface tension eliminates a circulation region in the flow chamber, hence increasing fluid bulk flow.

In Section 7.4, we show that surface tension prevents vortices generated by the cilia from extending to the upper fluid. The upper fluid is thus able to flow smoothly in the direction of cilia forward stroke, hence eliminating the recirculation region.

In Section 7.5, we examine the effects of surface tension and viscosity ratios on fluid transport. We show that when surface tension is absent, particles near the fluid interface adopt a corkscrew trajectory, but when surface tension is present, particles near the fluid interface adopt a linear trajectory. We also show that the absence of surface tension causes severe deformations of the fluid interface, hence enabling mixing of the fluids, while presence of surface tension suppresses the deformations, hence preventing mixing of the fluids.

7.2 Effect of surface tension and viscosity on bulk flows

In this section, we simulate the case of a cilia array in a two-fluid configuration for different fluid viscosity ratios μ_2 / μ_1 and interfacial surface tension σ. We limit our simulations to fluids that are immiscible. We also limit our simulations to the case where the interface height is set to be $h / H_\Omega = 0.43$ and cilia lengths set to be $L / H_\Omega = 0.33$. In all our simulations, the cilia tips do not penetrate the fluid interface..

Figure 7.2 shows (a) $U_{\parallel} / U_{\parallel 0}$ and (b) $U_{\perp} / U_{\perp 0}$ as functions of μ_2 / μ_1 and σ. The cross-sectional average velocity components $U_{\parallel}$ and $U_{\perp}$ are normal to the walls of the column as discussed in Section 5.7. $U_{\parallel}$ and $U_{\perp}$ are calculated as

$$U_{\parallel} = \frac{1}{TA} \int\int \frac{1}{2} \left[\left(\vec{u} \cdot \vec{n} \right)_{x^+} + \left(\vec{u} \cdot \vec{n} \right)_{x^-} \right] dA dt \,, \tag{7.1}$$

and

$$U_{\perp} = \frac{1}{TA}\int\int \frac{1}{2}\left[\left(\vec{u}\cdot\vec{n}\right)_{y^+} + \left(\vec{u}\cdot\vec{n}\right)_{y^-}\right] dAadt\,. \qquad (7.2)$$

Here, $A = H_{\Omega}\Delta l$ represents the area of each face of the column (Figure 5.13(a)) and T represents a simulated time long enough such that $U_{||}$ and $U_{\perp}$ have achieved steady values. In our simulations, we set $T = 0.3s$. $U_{||}$ and $U_{\perp}$ are then normalized to $U_{||0}$ and $U_{\perp 0}$ respectively, where $U_{||0}$ and $U_{\perp 0}$ represent the velocity components for the case of a single fluid, i.e. $\sigma = 0Nm^{-1}$ and $\mu_2/\mu_1 = 1$. $U_{||0}$ and $U_{\perp 0}$ are similarly calculated using equations 7.1 and 7.2.

From Figures 7.2(a) and (b), we observe that as the viscosity ratio μ_2/μ_1 between the upper and lower fluids increases, both $U_{||}/U_{||0}$ and $U_{\perp}/U_{\perp 0}$ decrease. This observation can be attributed to the fact that at a high value of μ_2/μ_1, there is high viscosity and increased damping in the upper fluid, consequently causing the upper fluid to attain lower time-averaged velocities.

We also note from Figure 7.2(a) that at low values of, μ_2/μ_1, the presence of surface tension dramatically increases $U_{||}/U_{||0}$. For example, in cases where $\mu_2/\mu_1 = 1$ and $\sigma > 0.0025Nm^{-1}$, $U_{||}$ is approximately twice that of $U_{||0}$. This observation shows that the presence of surface tension can effectively double the time-averaged flow rate over the case of a single fluid. We observe, however, that at high values of μ_2/μ_1, this effect is less pronounced. As before, this observation can be attributed to the damping effects of higher viscosities in the upper fluid. In addition, we observe that when $\sigma > 0.0025Nm^{-1}$, further increase in σ does little to increase $U_{||}/U_{||0}$. We observe that when $\sigma > 0.0025Nm^{-1}$, the surface tension is always large enough such that the interface is perpetually undeformed. Further increase in σ therefore does little to alter the dynamics of the system; hence average fluid

bulk flow velocity is no longer affected by increase in σ. This observation will be further elaborated upon in Sections 7.3 and 7.4.

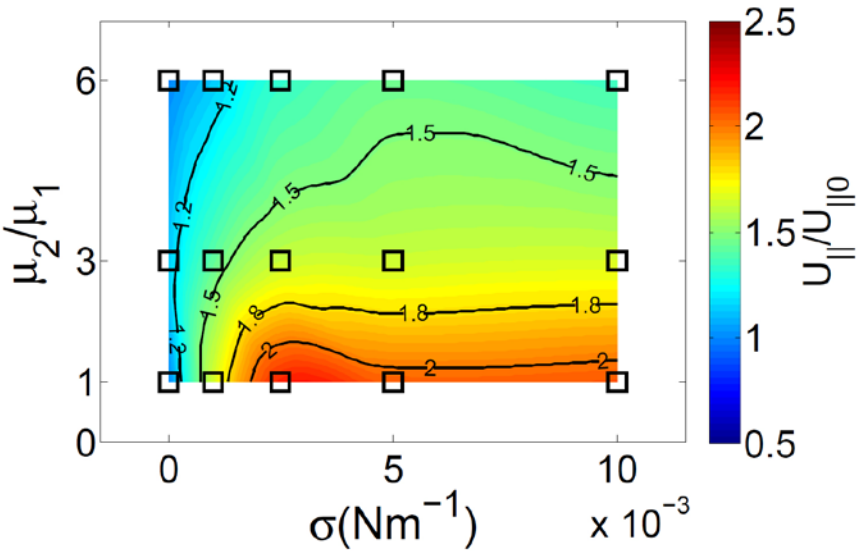

(a)

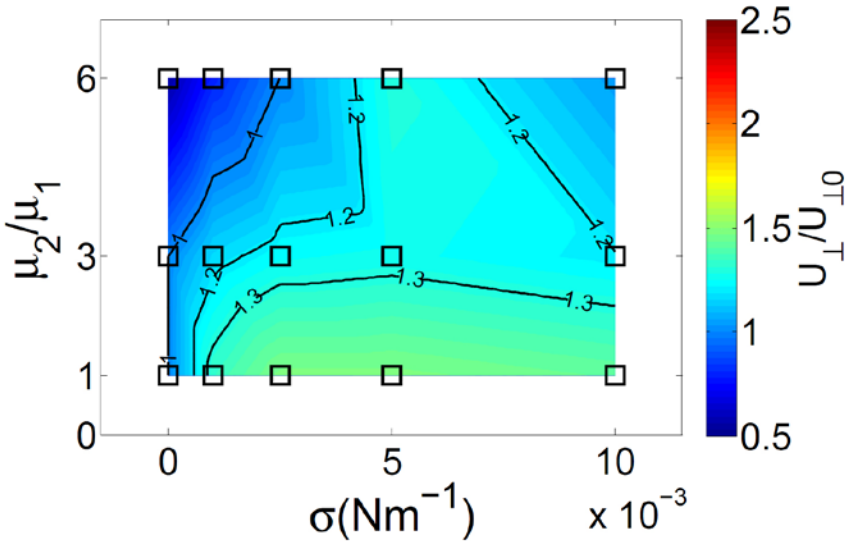

(b)

Figure 7.2 This figure shows contours of time-averaged cross-sectional velocities (a) parallel and (b) perpendicular to the cilia forward stroke. □ denotes values of μ_2 / μ_1 and σ at which simulations were performed.

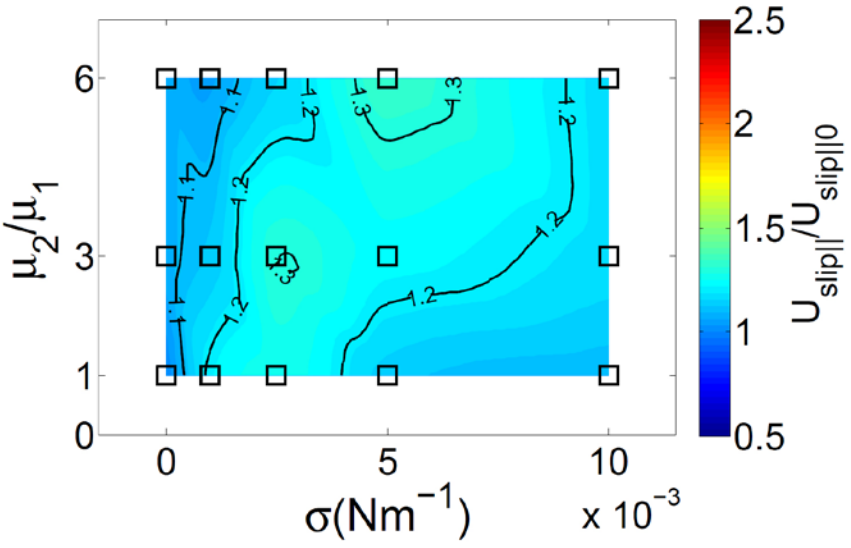

(a)

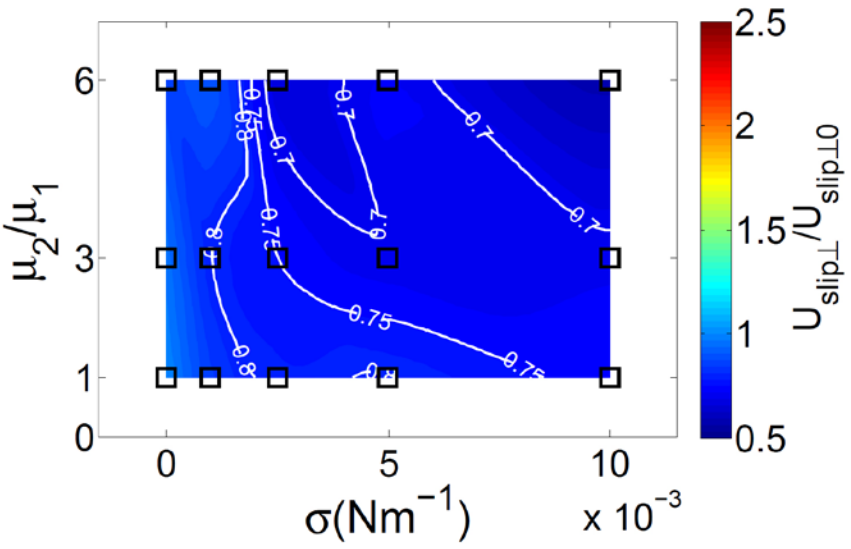

(b)

Figure 7.3 This figure shows contours of averaged cilia tip velocities (a) parallel and (b) perpendicular to cilia forward stroke. □ denotes values of μ_2 / μ_1 and σ at which simulations were performed.

Figure 7.3 shows the variation of (a) $U_{slip\|} / U_{slip\|0}$ and (b) $U_{slip\perp} / U_{slip\perp 0}$ with μ_2 / μ_1 and σ. $U_{slip\|}$ and $U_{slip\perp}$ are the time-averaged slip velocities at the cilia tips in the directions parallel ($\|$) and perpendicular ($\perp$) to the cilia forward stroke (Figure 7.1(b)). They are given as

$$U_{slip\parallel} = \frac{1}{T\Delta l^2}\int u_L d\left(\Delta l^2\right)dt, \tag{7.3}$$

and

$$U_{slip\perp} = \frac{1}{T\Delta l^2}\int v_L d\left(\Delta l^2\right)dt. \tag{7.4}$$

Here, Δl^2 is the horizontal cross-sectional area of the column (as shown by the shaded gray square in Figure 5.13(a)) at cilia height L. u_L and v_L are the fluid velocity components parallel and perpendicular to the forward stroke at cilia height L. In the case of a single fluid, $U_{slip\parallel 0}$ and $U_{slip\perp 0}$ are similarly calculated using equations 7.3 and 7.4.

In all cases of μ_2/μ_1, the cilia reside only in the lower fluid where $\mu = \mu_1$. The cilia are therefore subjected to conditions that are highly similar; hence we generally observe little differences in $U_{slip\parallel}/U_{slip\parallel 0}$ and $U_{slip\perp}/U_{slip\perp 0}$ over the ranges of μ_2/μ_1 and σ investigated by our model.

In our model, we observe that $U_\perp/U_{\perp 0}$ is not as significantly affected by inclusion of surface tension or by changes in viscosity ratio as $U_\parallel/U_{\parallel 0}$. Also, the slip velocities $U_{slip\parallel}/U_{slip\parallel 0}$ and $U_{slip\perp}/U_{slip\perp 0}$ are lower than $U_\perp/U_{\perp 0}$. Henceforth, we shall therefore focus our discussion on $U_\parallel$ and on flow quantities parallel to the cilia forward stroke.

In this section, we conclude that inclusion of surface tension significantly increases the fluid bulk flow in the direction parallel to the cilia forward stroke. This is true especially at low viscosity ratios. We also observe changes in surface tension or viscosity ratios do little to affect the fluid slip velocities in either the directions parallel or perpendicular to the cilia forward stroke. We next seek to understand the mechanism at which μ_2/μ_1 and σ modifies the

cross-sectional average velocity $U_{||}/U_{||0}$ by examining their effects on the fluid velocity profiles within the flow chamber.

7.3 Modification of velocity profiles by surface tension and fluid viscosity

We now seek to understand the effects of μ_2/μ_1 and σ on $U_{||}$ by examining the velocity profiles in the chamber. The time-averaged velocity profiles in the chamber are shown in Figure 7.4. The time-averaged velocity profiles are constructed by plotting the time-averaged velocity $\langle u \rangle$ at each height z. $\langle u \rangle$ is calculated as

$$\langle u \rangle = \frac{1}{T(\Delta l)^2} \iint u d(\Delta l)^2 \, dt . \tag{7.5}$$

From Figure 7.4(a), we observe that when $\sigma = 0.01 Nm^{-1}$, as μ_2/μ_1 is increased, the fluid velocities in the upper fluid above the interface is reduced while fluid velocities in the lower fluid below the interface remain mostly unchanged. This observation indicates that high viscous damping is present in the upper fluid at high values of μ_2/μ_1, thus accounting for the low values of $U_{||}/U_{||0}$ as observed in Figure 7.2(a)(i).

From Figure 7.4(b), we observe that when surface tension is absent (i.e. $\sigma = 0 Nm^{-1}$), increase in μ_2/μ_1 affects the velocity profile $\langle u \rangle$ minimally and hence does not translate to a significant change in $U_{||}/U_{||0}$. In addition, from Figure 7.4(c), we observe that when $\mu_2/\mu_1 = 1$, changes in surface tension causes a drastic change in the velocity profile $\langle u \rangle$ and hence in the cross-sectional average flow velocity $U_{||}/U_{||0}$. In particular, we note that the presence of surface tension eliminates the recirculation zone present below the

chamber ceiling when $\sigma = 0 Nm^{-1}$. The elimination of this recirculation zone increases $U_{\|} / U_{\|0}$ substantially.

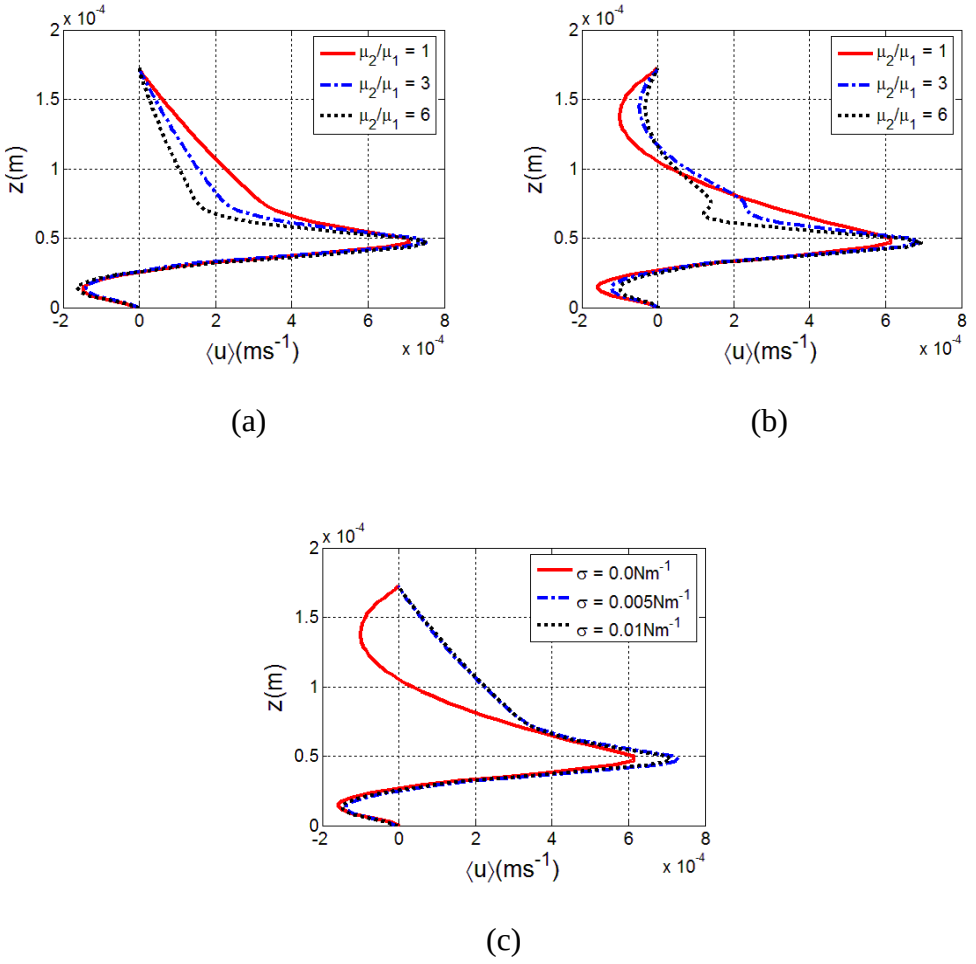

Figure 7.4. This figure shows velocity profiles in flow chamber. **(a)** Velocity profiles for surface tension $\sigma = 0.01 Nm^{-1}$ at various values of viscosity ratio μ_2 / μ_1 are shown. **(b)** Velocity profiles for surface tension $\sigma = 0 Nm^{-1}$ at various values of viscosity ratio μ_2 / μ_1 are shown. **(c)** Velocity profiles for viscosity ratio $\mu_2 / \mu_1 = 1$ at various values of surface tension σ are shown. Recirculation zones where $\langle u \rangle < 0 ms^{-1}$ are present when $\sigma = 0 Nm^{-1}$.

In this section, we explain the mechanism at which μ_2 / μ_1 and σ modifies the cross-sectional average velocity $U_{\|} / U_{\|0}$ by examining their effects on the fluid velocity profiles within the flow chamber. We establish that when

surface tension is present, the recirculation zone below the chamber ceiling is eliminated, thus increasing $U_{||}/U_{||0}$. We also show that when surface tension is present at the fluid interface, a reduction in viscosity ratio μ_2/μ_1 increases $U_{||}/U_{||0}$ by modifying the velocity profile in the upper fluid. These observations account for the increase in $U_{||}/U_{||0}$ when μ_2/μ_1 is reduced or when σ is increased (Figure 7.2(a)). However, when surface tension is absent, changes in μ_2/μ_1 has minimal effect on the velocity profile; consequently there is little change in $U_{||}/U_{||0}$. This observation is shown in Figure 7.2(a) when $\sigma = 0 Nm^{-1}$. Next, we shall seek to explain the mechanisms at which μ_2/μ_1 and σ modifies the velocity profiles.

7.4 Confinement of vortices by surface tension

We now seek to understand the mechanism where μ_2/μ_1 and σ affects the velocity profiles through observation of the fluid flow field. In particular, we seek to understand the mechanism by which the recirculation region is eliminated by surface tension. Figure 7.5 shows streamlines generated by cilia for the cases of (a) $\sigma = 0 Nm^{-1}$ and $\mu_2/\mu_1 = 1$, (b) $\sigma = 0.01 Nm^{-1}$ and $\mu_2/\mu_1 = 1$, (c) $\sigma = 0 Nm^{-1}$ and $\mu_2/\mu_1 = 6$, and (d) $\sigma = 0.01 Nm^{-1}$ and $\mu_2/\mu_1 = 6$. The streamlines are presented for the (i) forward (ii) and reverse strokes of the cilia. The streamlines are taken at the plane $y = 0$ for $-5\times10^{-5} m \le x \le 5\times10^{-5} m$.

We observe that when surface tension is absent, i.e. $\sigma = 0 Nm^{-1}$, large counter-clockwise vortices are generated by the cilia during the forward stroke. This observation is valid for both cases of μ_2/μ_1 presented (Figures 7.5(a)(i) and (c)(i)). These vortices extend to the chamber ceiling, causing the fluid below the chamber ceiling to travel opposite to the direction of cilia forward stroke, giving rise to the recirculation region.

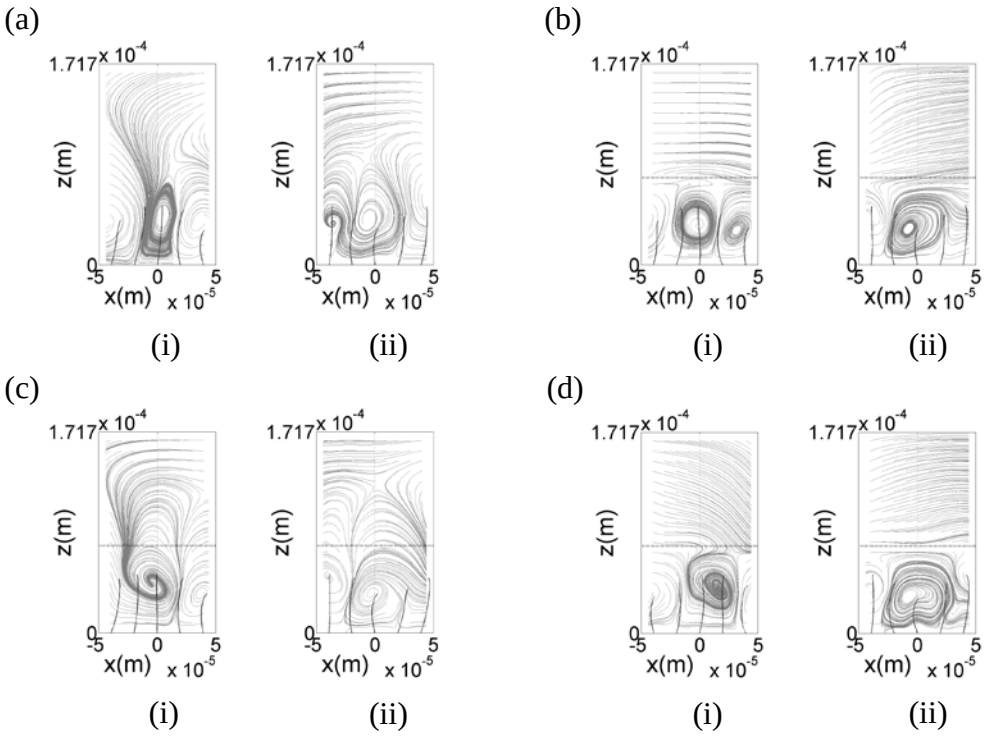

Figure 7.5 Streamlines in the fluid flow field generated by cilia are shown for the cases of of (a) $\sigma = 0 Nm^{-1}$ and $\mu_2 / \mu_1 = 1$, (b) $\sigma = 0.01 Nm^{-1}$ and $\mu_2 / \mu_1 = 1$, (c) $\sigma = 0 Nm^{-1}$ and $\mu_2 / \mu_1 = 6$, and (d) $\sigma = 0.01 Nm^{-1}$ and $\mu_2 / \mu_1 = 6$. In each case, the streamlines are presented for (i) cilia forward stroke and (ii) for cilia reverse stroke. In cases where two fluids are present, the fluid interface is indicated by a horizontal dashed line.

Similarly, we observe that clockwise vortices are generated by the cilia during the reverse stroke (Figures 7.5(a)(ii) and (c)(ii)). However, these vortices are smaller than the counter-clockwise vortices and do not extend to the chamber ceiling. We suggest that the clockwise vortices are smaller than the counter-clockwise vortices because the clockwise vortices are generated when the cilia tips are generally at lower heights during the reverse stroke. The dominant counter-clockwise vortices thus establish the region of recirculation observed in the time-averaged parabolic flow profile (Figure 7.4(b)).

We observe that with the inclusion of surface tension, i.e. $\sigma = 0.01 Nm^{-1}$, vortices are confined to the region below the interface. This confinement of vortices is observed for both cases of μ_2 / μ_1 presented (Figures 7.5(b) and (d)). We suggest that the presence of surface tension suppresses velocity components perpendicular to the fluid interface, hence preventing vortices from forming within the upper fluid layer. The fluid in the upper layer is observed to flow smoothly in the direction of the cilia forward stroke and is without a recirculation region (Figure 7.4(c)), thus attaining higher values of $U_{||} / U_{||0}$ (Figure 7.2(a)).

We observe that these vortices are generated by the presence of metachronal wave fronts. When metachronal waves are generated, rows of cilia in the forward stroke are flanked by rows of cilia in the reverse stroke (Figure 7.6). At the interface between metachronal wave fronts, cilia are either pushing fluid toward the interface or away from it. This action sets up opposing vortex pairs above the cilia tips.

We thus conclude from our simulations that the surface tension σ has the ability to eliminate the vortices in the upper fluid, hence modifying the velocity profiles observed in the flow chamber. This modification of the velocity profile leads to an elimination of the recirculation region in the fluid, thus increasing the cross-sectional average flow velocity $U_{||}$. However, we note that this increase in $U_{||}$ is limited by the viscosity ratio μ_2 / μ_1, where a high viscosity ratio impedes the maximum $U_{||}$ attainable.

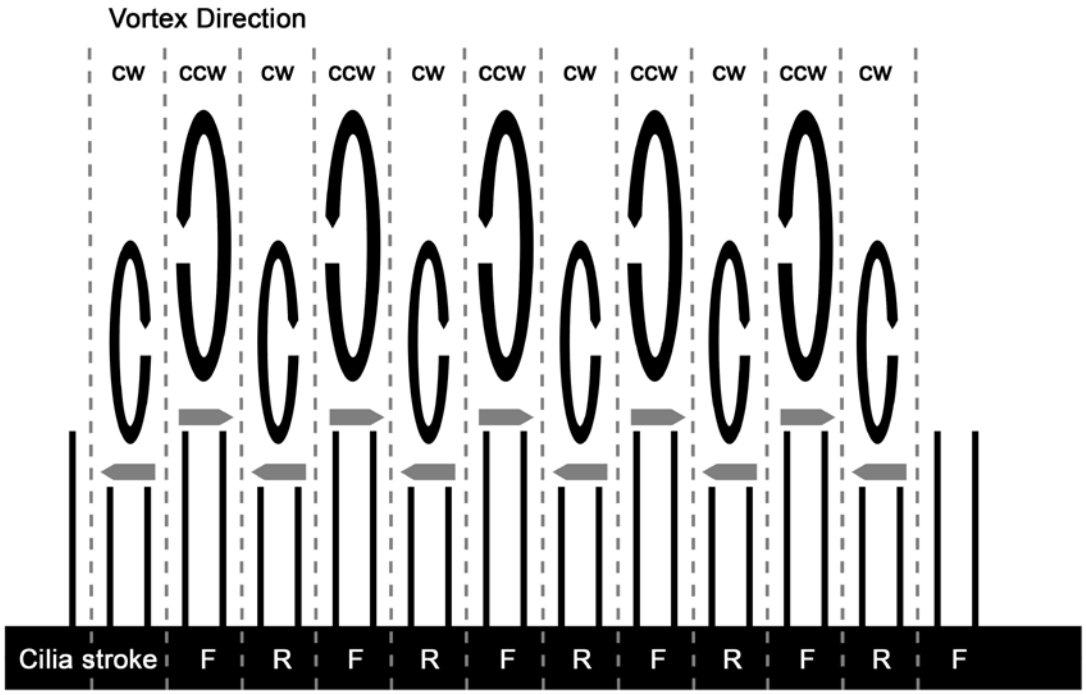

Figure 7.6 A schematic of the interaction between the fluid and cilia is shown. Metachronal wave fronts are formed by rows of cilia alternating between forward and reverse strokes (horizontal gray arrows). The metachronal wave front interfaces are indicated by vertical gray dotted lines. As cilia movement push fluid toward or away from the interfaces, opposing vortex pairs are set up in the fluid. Vortex directions are indicated counter-clockwise (ccw) or clockwise (cw).

7.5 Particle trajectories and fluid mixing

In this section, we examine the mixing aspects of the fluid by observing passive particles suspended in the fluid. We observe that these particles have their trajectories altered by the presence of surface tension. In the case where $\sigma = 0 Nm^{-1}$, we note that particles generally adopt a corkscrew trajectory. This is shown in Figure 7.7(a) for $\mu_2 / \mu_1 = 1$, and in Figure 7.7(c) for $\mu_2 / \mu_1 = 6$. In addition, in both of these cases, we observe severe deformations of the interface (Figures 7.8(a) and (c)).

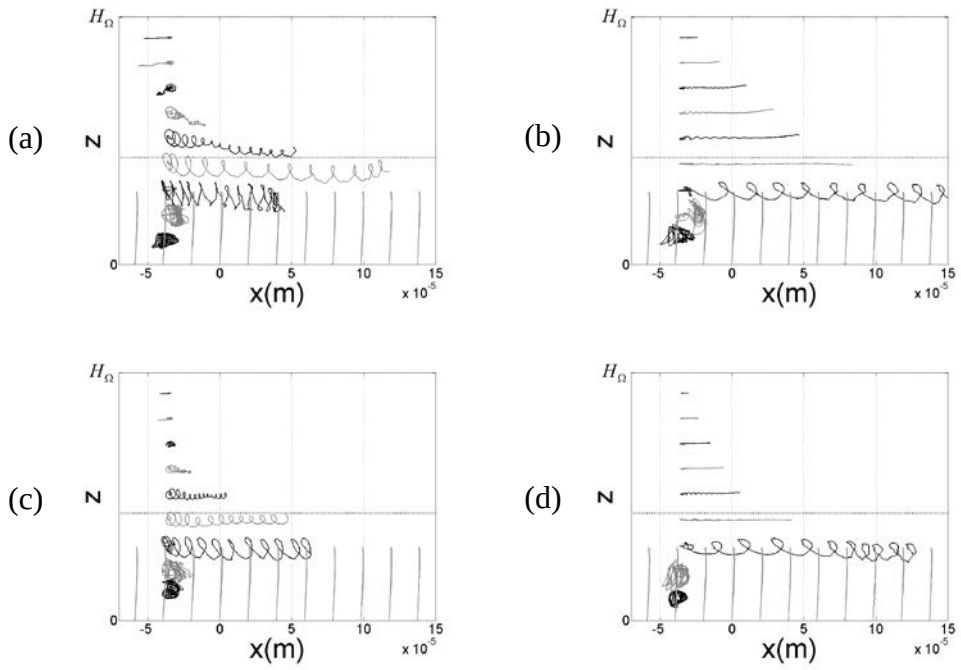

Figure 7.7 This figure shows particle trajectories seeded at various heights for (a) $\sigma = 0 Nm^{-1}$ and $\mu_2 / \mu_1 = 1$, (b) $\sigma = 0.01 Nm^{-1}$ and $\mu_2 / \mu_1 = 1$, (c) $\sigma = 0 Nm^{-1}$ and $\mu_2 / \mu_1 = 6$, and (d) $\sigma = 0.01 Nm^{-1}$ and $\mu_2 / \mu_1 = 6$. The particle traces for all cases are shown up to $t = 0.3s$.

When surface tension is increased to $\sigma = 0.01 Nm^{-1}$, we observe that particles above the fluid interface travel in linear trajectories. This is shown in Figure 7.7(b) for $\mu_2 / \mu_1 = 1$, and in Figure 7.7(d) for $\mu_2 / \mu_1 = 6$. We observe that the presence of surface tension prevents traction forces perpendicular to the surface to be transmitted to the upper fluid. This causes the particles embedded in the upper fluid to adopt a linear trajectories. In both of these cases, we observe little deformations of the interface (Figures 7.8(b) and (d)).

Below the interface, however, while the particle seeded at $h / H_\Omega = 0.31$ (located at cilia tips) retains a corkscrew trajectory, the particle at $h / H_\Omega = 0.41$ (located directly below the interface) adopts a linear trajectory. This again indicates that close to the interface, fluid velocity components perpendicular to the interface are suppressed by surface tension.

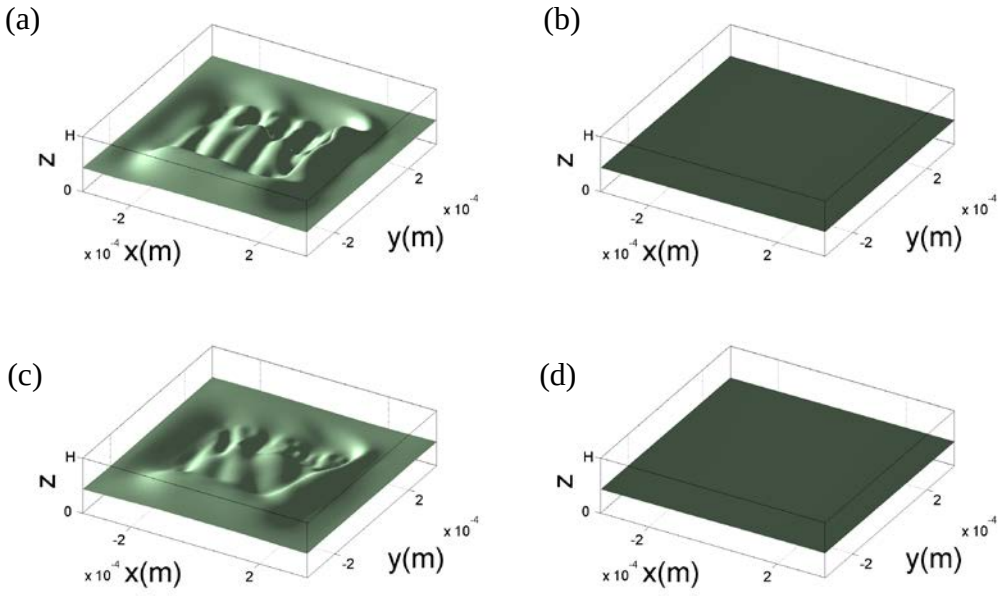

Figure 7.8 The interface deformation is shown in the cases of (a) $\sigma = 0 Nm^{-1}$ and $\mu_2 / \mu_1 = 1$, (b) $\sigma = 0.01 Nm^{-1}$ and $\mu_2 / \mu_1 = 1$, (c) $\sigma = 0 Nm^{-1}$ and $\mu_2 / \mu_1 = 6$, and (d) $\sigma = 0.01 Nm^{-1}$ and $\mu_2 / \mu_1 = 6$. Significant interface deformation is observed for all cases of μ_2 / μ_1 where $\sigma = 0 Nm^{-1}$ while negligible interface deformation is observed for all cases of μ_2 / μ_1 where $\sigma = 0.01 Nm^{-1}$. In all cases the interface deformations are shown at $t = 0.3s$.

In addition, we observe that when $\sigma = 0 Nm^{-1}$, significant mixing of the fluid is achieved through deformations of the interface (Figures 7.8(a) and (c)). This is true for all values of μ_2 / μ_1. However in the case where $\sigma = 0.01 Nm^{-1}$, interface deformation is negligible (Figures 7.8(b) and (d)). These observations are similar to those obtained by Dillon et al. [133].

Figure 7.9 quantifies the surface deformations at $t = 0.3s$. The surface deformation is quantified by the root mean square (RMS) value of the interface heights. The RMS interface height is calculated as

$$\text{RMS Interface Height} = \sqrt{\left\langle \left(h - \bar{h} \right)^2 \right\rangle} , \tag{7.6}$$

where h is the height of the interface and $\bar{h}$ is the average height of the interface. The RMS interface height is calculated for $-1.5\times10^{-4}m \le x \le 1.5\times10^{-4}m$ and $-1.5\times10^{-4}m \le y \le 1.5\times10^{-4}m$.

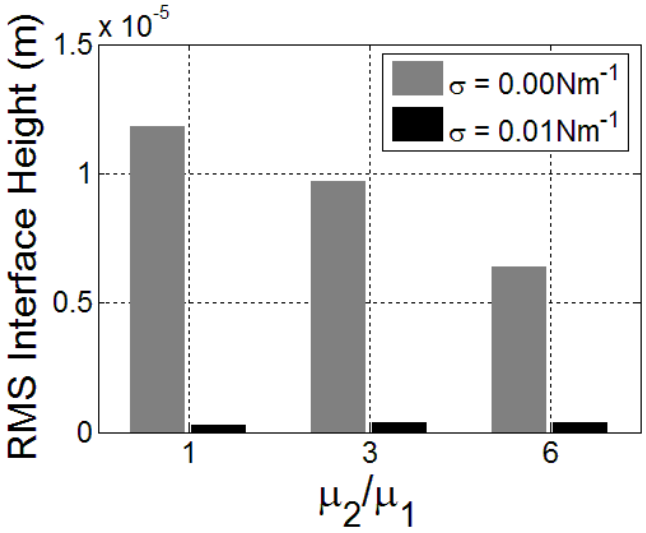

Figure 7.9 This figure shows the root mean square (RMS) interface heights of the interface between the upper and lower fluids at $t = 0.3s$.

We observe that at $\sigma = 0Nm^{-1}$, the RMS interface height values are high, indicating severe deformations of the interfaces. However, when μ_2 / μ_1 is increased, the RMS interface height is reduced. We attribute this observation to the damping effects of the upper fluid at high values of μ_2 / μ_1. We also observe that when $\sigma = 0.01Nm^{-1}$, at all values of μ_2 / μ_1, the RMS interface height values are low, indicating little deformations of the fluid interface. Mixing of the fluids is therefore possible only at low values of σ.

We emphasize that the fluid interface is solved using the level set equations. We are thus solving the convection equation without diffusive terms, hence the fluids do not mix through diffusion.

We propose that our simulated findings can be summarized by the phase space diagram shown in Figure 7.10. Here, contours of $\left(\text{RMS interface height}\right)/L$ are shown in blue while contours of $U_{\|}/U_{\|0}$ are shown in red. We first note a region of enhanced mixing, where, due to low surface tension σ, the interface is able to severely deform. This severe deformation causes a large interface area, thus aiding mixing. Second, we note a region of enhanced transport, where, due to high surface tension σ, the interface remains undeformed. Here, we find smooth flow in the upper fluid due to confinement of vortices to the lower fluid. Third, we note a region where there are no significant enhancements in mixing due to high surface tension σ, and no significant enhancement to fluid transport due to high viscosity ratio μ_2/μ_1.

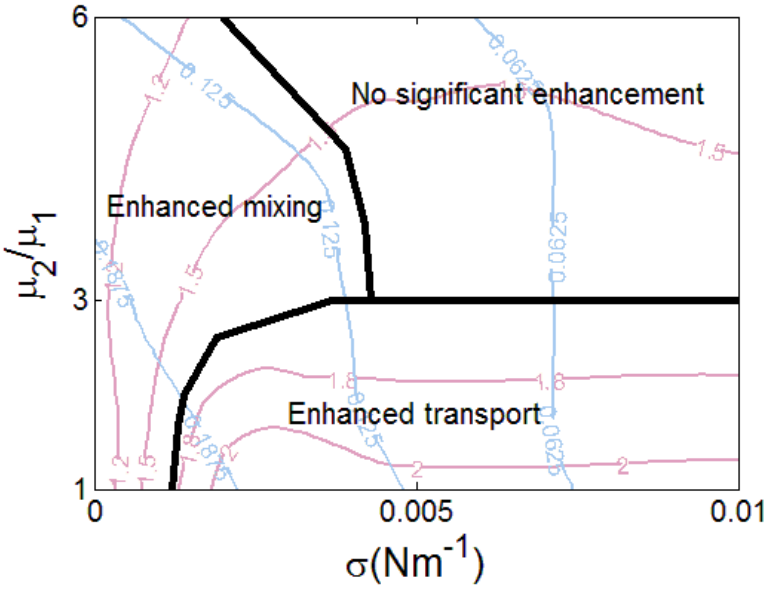

Figure 7.10 This figure shows a phase space diagram depicting our simulated findings. We note a region of enhanced mixing, a region of enhanced transport, and a region where no significant enhancement to either mixing or transport was observed. The blue contours are contours of $\left(\text{RMS Interface Height}\right)/L$ while the red contours are contours of $U_{\|}/U_{\|0}$.

In this section, we therefore conclude that particles close to the two-fluid interface have their trajectories affected by the presence of surface tension. In cases where surface tension is absent or negligible, particles close to the fluid

interface adopt a corkscrew trajectory. This is true for the entire range of viscosity ratios investigated by our model. In cases where surface tension is high, the velocity component of particles perpendicular to the interface is suppressed, hence particles close to the fluid interface adopt a linear trajectory. Again, this is true for all values of viscosity ratios investigated by our model.

By examining the trajectories of particles in the fluid, we also observe that velocity components perpendicular to the interface are prevented from being transmitted to the upper fluid, hence preventing vortices from forming in the upper fluid. The recirculation region is eliminated. Consequently, flow in the upper fluid is mostly smooth and free of vortices, resulting in an increase in the cross-sectional average fluid velocity in the chamber.

We also show that at low values of σ, there are significant deformations of the interface. These deformations are suppressed by the surface tension at high values of σ. We find that for $\sigma = 0.01 Nm^{-1}$, the interfaces are essentially undeformed, and consequently for $\sigma > 0.01 Nm^{-1}$, there is little change in $U_{\parallel}$. In the case of the PCL-mucus configuration in our respiratory system, the surface tension is shown to be $> 0.02 Nm^{-1}$. We can thus conclude that in most practical situations the interface would not be significantly deformed.

In this chapter, the choice of a Newtonian fluid was made for convenience. We acknowledge the choice of a non-Newtonian fluid may cause differences to the results. However implementation of a non-Newtonian fluid may be significantly more difficult. For example, solving the stress tensors in the Oldroyd-B model involves solving a dynamical equation, and its numerical solving process should be implemented such that it does not compromise the performance of the existing solving process. Implementation of a non-Newtonian solver may thus require a substantial amount of work.

8 Conclusions and future work

8.1 Conclusions

In this thesis, we presented numerical methods to study the dynamics of actively beating cilia. We modelled the cilia as simple beams that consisted of linear and torsional elastic springs. The model included an active forcing mechanism capable of spontaneously forming metachronal waves. The model was then implemented in a fluid solver based on the immersed boundary method. The fluid solver was then validated using the case of a lid-driven cavity and the cilia model was then validated by comparison with the Euler-Bernoulli beam equation. Next, using [44] as a benchmark, we showed that by varying the non-dimensional number Sp through variation of cilia length, beat frequency, bending stiffness and fluid viscosity, the direction of net fluid propulsion can be reversed.

We next investigated the formation, robustness and effects of metachronal waves on a 21×21 cilia array. This array was made to mimic the cilia on micro-swimmers such as *Paramecium* and *Opalina*, or the flagella on multi-flagellated micro-swimmers such as *Volvox*. We observed the spontaneous formation of metachronal waves. Following, we imposed perturbations in the forms of local cilia stroke reversal and substrate stretching. In both instances of perturbations, we observed that metachronal waves were mostly intact; however when stretching amplitudes were large, metachronal waves were disrupted. We then simulated a cilia array with an unstructured arrangement and again showed the formation of metachronal waves. In addition, we showed that the side-ways sweep motion imposed in our model was essential in forming of metachronal wave fronts. We therefore concluded that the metachronal waves in our model were robust to various forms of perturbations and disturbances.

We next proceeded to study effects on fluid transport in our model. We showed an increase in cilia number density caused a decrease in cilia beat frequency and an increase in metachronal wave number. We also found that there exists a maximum fluid slip velocity at the cilia tips when $d / L \sim 0.3$. This value of d / L agrees with those reported in literature corresponding to optimum fluid flow rates. Also, by observing the trajectories of particles embedded in the fluid, we found that particles embedded within the cilia array demonstrate diffusion-like behavior while particles embedded in the fluid above the cilia demonstrate advective behavior.

Finally, we modelled cilia in a stratified, two-fluid arrangement. This arrangement was designed to model the conditions in our respiratory system, where the cilia is embedded in a Newtonian periciliary layer (PCL), with a layer of non-Newtonian mucus on top. We showed that higher viscosities in the upper fluid and the presence of surface tension at the fluid interface reduce interface deformations. We found that the presence of surface tension between the upper and lower fluids prevents velocity components perpendicular to the interface from being transmitted across the interface. This has the effect of confining vortices generated by the cilia to the lower fluid, hence modifying the fluid velocity profiles in the flow chamber and leading to increased bulk fluid flow rates.

8.2 Future work

In future work, we would like to incorporate a more realistic model for our cilia. At present, our model generates mostly symplectic metachronal waves. However in nature, it is the antiplectic metachronal wave that is more common. We would like to investigate the mechanisms behind metachronal wave direction.

In the case of cilia in a stratified, two-fluid arrangement, we would like to include a non-Newtonian model for the upper fluid. There are several methods to model a non-Newtonian fluid, examples of which are the Oldroyd-B model

and the Maxwell model. A clear, concise description of the Oldroyd-B fluid model is given in [134], while an excellent example of cilia modeling with the Maxwell fluid model can be seen in [135].

In addition, it is well-known that cilia tips penetrate the mucus-PCL interface during the forward stroke. In our present model, should our cilia penetrate the interface, the strong surface tension forces present at the interface would prevent the withdrawal of the cilia tips into the PCL during the reverse stroke. Our cilia model would essentially ‘seize’. This is a current limitation of our model that we would like to remedy.

9 References

1. Marshall, W. F. and Nonaka, S., “Cilia: tuning in to the cell’s antenna (2006)”, Current Biology, Vol. 16, Issue 15, R604-614
2. Gilliam, J. C., Chang, J. T., Sandoval, I. M., Zhang, Y., Li, T., Pittler, S. J., Chiu, W. and Wensel, T. G., “Three-dimensional architecture of the rod sensory cilium and its disruption in retinal neurodegeneration (2012)”, Cell, Vol. 151, Issue 5, pp. 1027-1041
3. Letinen, M. K. and Walsh, C. A., “Neurogenesis at the brain-cerebrospinal fluid interface (2011)”, Annual Review of Cell and Developmental Biology, Vol. 27, pp. 653-679
4. Vallee, R. B., Williams, J. C., Varma, D. and Barnhart, L. E., “Dynein: an ancient motor protein involved in multiple modes of transport (2004)”, Developmental Neurobiology, Vol. 58, Issue 2, pp. 189-200
5. Breuning, J., Arellano, J. and Rakic, R., “Cilia in the brain: going with the flow (2010)”, Nature Neuroscience, Vol. 13, No. 6, pp. 654-655
6. Breuning, J. J., Sarkisian, M. R., Arellano, J. I., Morozov, Y. M., Ayoub, A. E., Sojitra, S., Wang, B., Flavell, R. A., Rakic, P. and Town, T., “Primary cilia regulate hippocampal neurogenesis by mediating sonic hedgehog signaling (2008)”, Proceedings of the National Academy of Sciences, Vol 105, pp. 13127-13132
7. Guirao, B., Meunier, A., Mortaud, S., Aguilar, A., Corsi, J. M., Strehl, L., Hirota, Y., Desoeuvre, A., Boutin, C., Han, Y. G., Mirzadeh, Z., Cremer, H., Montcouquiol, M., Sawamoto, K. and Spassky, N., “Coupling between hydrodynamic forces and planar cell polarity orients mammalian motile cilia (2010)”, Nature Cell Biology, Vol. 12, pp. 341-350
8. Chevance, F. F. V. and Hughes, K. T., “Coordinating assembly of a bacterial macromolecular machine (2008)”, Nature Reviews Microbiology, Vol. 6, pp. 455-465
9. Yano, J., Valentine, M. S. and Van Houten, J. L., “Novel insights into the development and function of cilia using the advantages of th*e*

Paramecium cell and its many cilia (2015)", Cells, Vol. 4, Issue 3, pp. 297-314

10. Li, W., Wang, C., Huang, F., Li, M., Nilsen, F., Liu, H. and Xu, J., "Redescription of *Protoopalina* pingi Nie, 1935 inhabiting the recta of *Hylarana* guentheri and *Pelophylax* nigromaculatus in China (2014)", Parasite, Vol. 21, Article 46
11. Sleigh, M. A., "The form of beat in cilia of *Stentor* and *Opalina* (1960)", The Journal of Experimental Biology, Vol. 30, No. 1, pp. 1-10
12. Berg, H., "How bacteria swim (1975)", Scientific American, Issue 233, pp. 36-44
13. Button, B., Cai, L. H., Ehre, C., Kesimer, M., Hill, D. B., Sheehan, J. K., Boucher, R. C., Rubinstein, M., "A periciliary brush promotes the lung health by separating the mucus layer from airway epithelia (2012)", Science, Vol 337, No. 6097, pp. 937-941
14. Fauci, L. and Dillon, R., "Biofluidmechanics of Reproduction (2006)", Annual Review of Fluid Mechanics, Vol. 38, 371-394
15. Sugino, K., Naitoh, Y., "Simulated cross-bridge patterns corresponding to ciliary beating in Paramecium (1982)", Nature, Vol. 295, pp. 609-611
16. Machemer, H., "Properties of polarized ciliary beat in *Paramecium* (1972)", Acta Protozoologica, Vol. 11, Symposium Motile System of Cells, pp. 295-300
17. Brokaw, C., "Simulating the effects of fluid viscosity on the behavior of sperm flagella (2001)", Mathematical Methods in the Applied Sciences, Vol. 24, No. 17-18, pp. 1351-1365
18. Sanchez, T., Welch, D., Nicastro, D. and Dogic, Z., "Cilia-like beating of active microtubule bundles (2011)", Science, Vol. 333, No. 6041, pp. 456-459
19. Rai, A. K., Rai, A., Ramaiya, A. J., Jha, R. and Mallik, R., "Molecular adaptations allow dynein to generate large collective forces inside cells (2013)", Cell, Vol. 152, Issues 1-2, pp. 172-182
20. Sanderson, M. and Sleigh, M., "Ciliary activity of cultured rabbit tracheal epithelium: beat pattern and metachrony (1981)", Journal of Cell Science, Vol. 47, pp. 331-347

21. Okamoto, K.-I. and Nakaoka, Y., “Reconstitution of metachronal waves in ciliated cortical sheets of *Paramecium* (1994)”, Journal of Experimental Biology, Vol. 192, pp. 61-72.
22. Nakaoka, Y. and Ooi, H., “Regulation of ciliary reversal in triton-extracted Paramecium by calcium and cyclic adenosine monophosphate (1985)”, Journal of Cell Science, Vol. 77, pp. 185-195
23. Bonini, N. M. and Nelson, D. L, “Differential regulation of Paramecium ciliary motility by cAMP and cGMP (1988)”, Journal of Cell Biology, Vol. 106, Issue 5, pp. 1615-1623
24. Noguchi, M. et al., Kakamura, Y. and Okamoto, K.-I., “Control of ciliary orientation in ciliated sheets from Paramecium-differential distribution of sensitivity to cyclic nucleotides (1991)”, Cell Motility and the Cytoskeleton, Vol. 20, Issue 1, pp. 38-46
25. Iwadate, Y. and Nakaoka, Y., “Calcium regulates independently ciliary beat and cell contraction in paramecium cells (2008)”, Cell Calcium, Vol. 44, pp. 169-179
26. Drescher, K., Leptos, K. C., Tuval, I., Ishikawa, T., Pedley, T. J. and Goldstein, R. E., “Dancing volvox: hydrodynamic bound states of swimming algae (2009)”, Physical Review Letters, Vol. 102, No. 168101
27. Guasto, J. S., Riffell, J, A., Zimmer, R. K. and Stocker, R., “Chemotactic maneuverability of sperm (2011)”, arXiv:1110.2835V1[physics.flu-dyn]
28. Shields, A. R., Fiser, B. L., Evans, B. A., Falvo, M. R., Washburn, S. and Superfine, R., “Biomimetic cilia arrays generate simultaneous pumping and mixing regimes (2010)”, Proceedings of the National Academy of Sciences, Vol. 107, No. 36, pp. 15670-15675
29. Babataheri, A., Roper, M., Fermigier, M. and Roure, O. D., “Tethered fleximags as artificial cilia (2011)”, Journal of Fluid Mechanics, Vol. 678, pp. 5-13
30. Vilfan, M., Potocnik, A., Kavcic, B., Osterman, N., Poberaj, I., Vilfan, A. and Babic, D., “Self-assembled aritificial cilia (2010)”, Proceedings of the National Academy of Sciences, Vol. 107, No. 5, pp. 1844-1847

31. Kokot, G., Vilfan, M., Osterman, N., Vilfan, A., Kavčič, B., Poberaj, I. and Babič, D., "Measurement of fluid flow generated by artificial cilia (2011)", Biomicrofluidics, Vol. 5, pp.034103-1 to 034103-9
32. Oh, K., Chung, J.-H., Devasia, S. and Riley, J. J., "Bio-mimetic silicone cilia for microfluidic manipulation (2009)", Lab on a Chip, Vol. 9, Issue 11, pp. 1561-1566
33. Oh, K., Smith, B., Devasia, S., Riley, J. J. and Chung, J.-H., "Characterization of mixing performance for bio-mimetic silicone cilia (2010)", Microfluidics and Nanofluidics, Vol. 9, Issue 4, pp. 645-655
34. Purcell, E. M., "Life at low Reynolds number (1977)", American Journal of Physics, Vol. 45, pp. 3-11
35. Kongthon, J., McKay, B., Iamratanakul, D., Oh, K., Chung, J.-H., Riley, J. and Devasia, S., "Added-mass effect in modeling of cilia-based devices for microfluidic systems (2010)", Journal of Vibration and Acoustics, Vol. 132, Issue 2, pp. 024501-1 to 024501-7
36. Kongthon, J., Chung, J.-H., Riley, J. J. and Devasia, S., "Dynamics of cilia-based microfluidic devices (2011)", Journal of Dynamic Systems, Measurement, and Control, Vol. 133, Issue 5, pp. 051012-1 to 051012-11
37. Kongthon, J. and Devasia, S., "Iterative control of piezoactuator for evaluating biomimetic, cilia-based micromixing (2013)", IEEE/ASME Transactions on Mechatronics, Vol. 18, No. 3, pp. 944-953
38. Zetes, D. E. and Steele, C. R., "Fluid-structure interaction of the stereocilia bundle in relation to mechanotransduction (1997)", The Journal of the Acoustical Society of America, Vol. 101, Issue 6, pp. 3593-3601
39. Gao, W., Sattayasamitsathit, S., Manesh, K. M., Weihs, D. and Wang, J., "Magnetically powered flexible metal nanowire motors (2010)", Journal of the Americal Chemical Society, Vol. 132, pp. 14403-14405
40. Lauga, E. and Powers, T. R, "The hydrodynamics of swimming microorganisms (2009)", Reports on Progress in Physics, Vol. 72, No. 9, pp. 1-39
41. Vladimirov, V. A., "On the self-propulsion of an N-sphere micro-robot (2012)", Journal of Fluid Mechanics, Vol. 716, pp. R1-1 to R1-11

42. Vladimirov, V. A., “Dumbbell micro-robot driven by flow oscillations (2012)”, Journal of Fluid Mechanics, Vol. 717, pp. R8-1 to R8-11
43. Vaughan, T. J., Mullen, C. A., Verbruggen, S. W. and McNamara, L. M., “Bone cell mechanosensation of fluid flow stimulation: a fluid–structure interaction model characterising the role integrin attachments and primary cilia (2015)”, Vol. 14, Issue 4, pp. 703-718
44. Alexeev, A., Yeomans, J. M. and Balazs, A. C., “Designing synthetic, pumping cilia that switch the flow direction in microchannels (2008)”, Langmuir, Vol. 24, No. 21, pp. 12102-12106
45. Khaderi, S., den Toonder, J. and Onck, P., “Microfluidic propulsion by the metachronal beating of magnetic artificial cilia: a numerical analysis (2011)”, Journal of Fluid Mechanics, Vol. 688, pp. 44-65
46. Khaderi, S. and Onck, P., “ Fluid-structure interaction of three-dimensional magnetic artificial cilia (2012)”, Journal of Fluid Mechanics, Vol. 708, pp. 303-328
47. Dillon, R., Fauci, L., Fogelson, A. and Gaver, D., “Modeling biofilm processes using the immersed boundary method (1996)”, Journal of Computational Physics, Vol. 129, pp. 57-73
48. Peskin, C., "The immersed boundary method (2002)", Acta Numerica, pp. 1-39
49. Hsu, C. Y. and Dillon, R., “A 3D motile rod-shaped monotrichous bacterial model (2009)”, Bulletin of Mathematical Biology, Vol. 71, No. 5, pp. 1228-1263
50. Lee, W. L., Jayathilake, P. G., Tan Z., Le, D. V., Lee, H. P. and Khoo, B. C., “Muco-ciliary transport: effect of mucus viscosity, cilia beat frequency and cilia density (2011)”, Computers and Fluids, Vol. 49, Issue 1, pp. 214-221
51. Jayathilake, P. G., Tan, Z., Le, D. V., Lee, H. P. and Khoo, B. C., “Three-dimensional numerical simulations of human pulmonary cilia in the periciliary liquid layer by the immersed boundary method (2012)”, Computers and Fluids, Vol. 67, pp. 130-137
52. Jayathilake, P. G., Le, D. V., Tan, Z., Lee, H. P. and Khoo, B. C., “A numerical study of muco-ciliary transport under the condition of

diseased cilia (2015)", Computer Methods in Biomechanics and Biomedical Engineering, Vol. 18, No. 9, pp. 944-951

53. Pozrikidis, C., "Introduction to theoretical and computational fluid mechanics (1997)", Oxford University Press, Oxford, UK, 1997
54. Cortez, R., Fauci, L. and Medovikov, A., "The method of regularized Stokeslets in three dimensions: analysis, validation, and application to helical swimming (2005)", Physics of Fluids, Vol. 17, pp. 031504
55. Cortez, R., "The method of regularized Stokeslets (2001)", SIAM Journal of Scientific Computing, Vol. 23, Issue 4, pp. 1204-1225
56. Smith, D. J., "A boundary element regularized Stokeslet method applied to cilia and flagella-driven flow (2010)", Proceedings of the Royal Society of London Series A, Vol. 471, Issue 2175, pp. 3605-3626
57. Bouzarth, E. and Minion, M. L., "Modeling slender bodies with the method of regularized Stokeslet (2011)", Journal of Computational Physics, Vol. 230, Issue 10, pp. 3929-3947
58. Ainleya, J., Durkin, S., Embid, R., Boindala, P. and Cortez, R, "The method of images for regularized Stokeslets (2008)", Journal of Computational Physics, Vol. 227, Issue 9, pp. 4600-4616
59. Cortez, R. and Varela, D., "A general system of images for regularized Stokeslets and other elements near a plane wall (2015)", Journal of Computational Physics, Vol. 285, pp. 41-54
60. Lighthill, M. J., "On the squriming motion of nearly spherical deformable bodies through liquids at very small Reynolds numbers (1952)", Communications on Pure and Applied Mathematics, Vol. 5, Issue 2, pp. 109-118
61. Osterman, N. and Vilfan, A., "Finding the ciliary beating pattern with optimal efficiency (2011)", Proceedings of the National Academy of Sciences, Vol. 108, no. 38, pp. 15727-15732
62. Avron, J. E., Gat, O. and Kenneth, O., "Optimal swimming at low Reynolds numbers (2004)", Physical Review Letters, Vol. 93, No. 18, pp. 186001
63. Saffman, P. G., "The self-propulsion of a deformable body in a perfect fluid (1967)", Journal of Fluid Mechanics, Vol. 28, Issue 2, pp. 385-389

64. Shapere, A. and Wilczek, F., “Geometry of self-propulsion at low Reynolds number (1989)”, Journal of Fluid Mechanics, Vol. 198, pp. 557-585
65. Spagnolie, S. and Lauga, E., “The optimal elastic flagellum (2010)”, Physics of Fluids, Vol. 22, pp. 031901
66. Lauga, E. and Eloy, C., “Shape of optimal active flagella (2013)”, Journal of Fluid Mechanics, Vol. 730, pp. R1-1 to R1-11
67. Guo, H., Nawroth, J., Ding, Y. and Kanso, E., “Cilia beating patterns are not hydrodynamically optimal (2014)”, Physics of Fluids, Vol. 26, pp. 091901-1 to 091901-12
68. Li, L. and Spagnolie, S. E., “Swimming and pumping of rigid helical bodies in viscous fluids (2014)”, Physics of Fluids, Vol. 26, pp. 041901-1 to 041901-19
69. Khatavkar, V. V., Anderson, P. D., den Toonder, J. M. J. and Meijer, H. E. H., “Active micromixer based on artificial cilia (2007)”, Physics of Fluids, Vol. 19, pp. 083605-1 to 083605-13
70. Aref, H., “Stirring by chaotic advection (1984)”, Journal of Fuid Mechanics, Vol. 143, pp. 1-21
71. Murase, M., "Dynamics of cellular motility (1992)", Wiley-Blackwell
72. Lindemann, C. B. and Lesich, K. A., “Flagellar and ciliary beating: the proven and the possible (2010)”, Journal of Cell Science, Vol. 123, pp. 519-528
73. Brokaw, C. J., “Computer simulation of flagellar movement. I. Demonstration of stable bend propagation and bend initiation by the sliding filament model (1972)”, Biophysical Journal, Vol. 12, Issue. 5, pp. 564-586
74. Brokaw, C. J., “Flagellar movement: a sliding filament model (1972)”, Science, Vol. 178, No. 4060, pp. 455-462
75. Brokaw, C. J., “Computer simulation of flagellar movement. IV. Properties of an oscillatory two-state cross-bridge model (1976)”, Biophysical Journal, Vol. 16, Issue, 9 pp. 1029-1041
76. Brokaw, C. J., “Computer simulation of flagellar movement. VI. Simple curvature controlled models are incompletely specified (1985)”, Biophysical Journal, Vol. 48, Issue 4, pp. 633-642

77. Omoto, C. K. and Kung, C., “The pair of central tubules rotates during ciliary beat in Paramecium (1979)”, Nature, Vol 279, pp. 532-534
78. Omoto, C. K. and Kung, C., “Functionally significant central-pair rotation in a primitive eukaryotic flagellum (1981)”, Nature, Vol. 290, pp. 708-710
79. Sugino, K. and Naitoh, Y., “Simulated cross-bridge patterns corresponding to ciliary beating in Paramecium (1982)”, Nature, Vol. 295, pp. 609-611
80. Murase, M. and Shimizu, H., “A model of flagellar movement based on cooperative dynamics of dynein-tubulin cross-bridges (1986)”, Journal of Theoretical Biology, Vol. 119, Issue 4, pp. 409-433
81. Lindemann, C. B., “A “geometric clutch”, hypothesis to explain oscillations of the axoneme of cilia and flagella (1994)”, Journal of Theoretical Biology, Vol. 168, Issue 2, pp. 175-189
82. Gueron, S. and Liron, N., “Ciliary motion modeling, and dynamic multicilia interactions (1992)”, Biophysical Journal, Vol. 63, Issue 4, pp.1045-1058
83. Gueron, S. and Liron, N., “Simulations of three-dimensional ciliary beats and cilia interactions (1993)”, Biophysical Journal, Vol. 65, Issue 1, pp. 499-507
84. Gueron, S., Levit-Gurevich, K., Liron, N. and Blum, J. J., “Cilia internal mechanism and metachronal coordination as the result of hydrodynamic coupling (1997)”, Proceedings of the National Academy of Sciences, Vol. 94, No. 12, pp. 6001-6006
85. Gueron, S. and Levit-Gurevich, K., “Energetic considerations of ciliary beating and the advantage of metachronal coordination (1999)”, Proceedings of the National Academy of Sciences, Vol. 96, No. 22, pp. 12240-12245
86. Dillon, R., Fauci, L. and Omoto, C., "Mathematical modeling of axoneme mechanics and fluid dynamics in ciliary and sperm motility (2003)", Dynamics of Continuous, Discrete and Impulsive Systems Series A: Mathematical Analysis, Vol 10, No. 5, pp. 745-757

87. Yang, X., Dillon, R. H. and Fauci, L., J., “An integrative computational model of multiciliary beating (2008)”, Bulletin of Mathematical Biology , Vol. 70, Issue 4, pp. 1192-1215
88. Elgeti, J., and Gompper, G., “Emergence of metachronal waves in cilia arrays (2013)”, Proceedings of the National Academy of Sciences, Vol. 110, No. 12, pp. 4470-4475
89. Vilfan, A. and Jülicher, F., “Hydrodynamic flow patterns and synchronization of beating cilia (2006)”, Physical Review Letters, Vol. 96, No. 058102
90. Lagomarsino, M. C., Jona, P. and Bassetti, B., “Metachronal waves for deterministic switching two-state oscillators with hydrodynamic interaction (2003)”, Physical Review E, Vol. 68, No. 021908
91. Wollin, C. and Stark, H., “Metachronal waves in a chain of rowers with hydrodynamic interactions (2011)”, The European Physical Journal E, Vol. 34, pp. 42-52
92. Niedermayer, T., Eckhardt, B., Lenz, P., “Synchronization, phase-locking, and metachronal wave formation in ciliary chains (2008)”, Chaos: An Interdisciplinary Journal of Nonlinear Science, Vol. 18, pp. 037128-1 to 037128-10
93. Peskin, C. S., “Flow patterns around heart valves: a numerical method (1972)”, Journal of Computational Physics, Vol. 10, Issue 2, pp. 252-271
94. Peskin, C. S., “Numerical analysis of blood flow in the heart (1977)”, Journal of Computational Physics, Vol. 25, Issue 3, pp. 220-252
95. Peskin, C. S. and McQueen, D. M., “Modeling prosthetic heart valves for numerical analysis of blood flow in the heart (1980)”, Journal of Computational Physics, Vol. 37, Issue 1, pp. 113-132
96. Peskin, C. S. and McQueen. D. M., “A three-dimensional computational method for blood flow in the heart I. Immersed elastic fibers in a viscous incompressible fluid (1989)”, Journal of Computational Physics, Vol. 81, Issue 2, pp. 372-405
97. Peskin, C. S. and McQueen, D. M., “A three-dimensional computational method for blood flow in the heart II. Contractile fibers

(1989)", Journal of Computational Physics, Vol. 82, , Issue 2, pp. 289-297

98. McQueen, D. M. and Peskin, C. S., "Heart simulation by an immersed boundaary method with formal second order accuracy and reduced numerical viscosity (2001)", Mechanics for a New Millennium, Proceedings of the International Conference on Theoretical and Applied Mechanics 2000, Kluwer Academic Publishers, 2001
99. N'Dri, N. A., Shyy, W. and Tran-Son-Tay, R., "Computational modeling of cell adhesion and movement using a continuum-kinetics approach (2003)", Biophysical Journal, Vol. 85, Issue 4, pp. 2273-2286
100. Jadhav, S., Eggleton, C. D. and Konstantopoulos, K., "A 3-D computational model predicts that cell deformation affects selectin-mediated leukocyte rolling (2005)", Biophysical Journal, Vol. 88, Issue 1, pp. 96-104
101. Skorczewski, T., Erickson, L. C., Fogelson, A. L., "Platelet motion near a vessel wall or thrombus surface in two-dimensional whole blood simulations (2013)", Biophysical Journal, Vol. 104, Issue 8, pp. 1764-1772
102. Vahidkhah, K., Diamond, S. L. and Bagchi, P., "Platelet dynamics in three-dimensional simulation of whole blood (2014)" Biophysical Journal, Vol. 106, Issue 11, pp. 2529-2540
103. Kim, Y and Peskin, C. S., "Penalty Immersed Boundary Method for an Elastic Boundary with Mass (2007)", Physics of Fluids, Vol. **19**, pp. 053103
104. Li, Z. and Ito, K., "The Immersed Interface Method -- Numerical Solutions of PDEs Involving Interfaces and Irregular Domains (2006)", SIAM Frontiers in Applied mathematics, 33, Philadelphia, 2006, ISBN: 0-89871-609-8.
105. Peraire, J. and Persson, P. -O., "A High Order Discontinuous Galerkin Method for Fluid-Structure Interaction (2007)", 18th AIAA Computational Fluid Dynamics Conference, 10.2514/6.2007-4327
106. Chorin, A. J., "The numerical solution of the Navier-Stokes equations for an incompressible fluid (1967)", Bulletin of the American Mathematical Society, Vol. 73, pp. 928-931

107. Chorin, A. J., “Numerical solutions of the Navier-Stokes equations (1968)”, Mathematics of Computation, Vol. 22, pp. 745-762
108. Tannehill, J, Anderson, D. and Pletcher, R., "Computational fluid mechanics and heat transfer, second edition (1997)", Taylor and Francis
109. Center for Applied Scientific Computing, Lawrence Livermore National Laboratory, "Hypre high performance preconditioners (2006)"
110. Olsson, K. and Kreiss, G., “A conservative level set method for two-phase flow (2005)”, Journal of Computational Physics, Vol. 210, pp. 225-246
111. Sussman, M., Smereka, P. and Osher, S., “A level set approach for computing solutions to incompressible two-phase flow (1994)”, Journal of Computational Physics, Vol. 114, Issue 1, pp. 146-159
112. Sethian, J. A., “A fast marching level set method for monotonically advancing fronts (1996)”, Proceedings of the National Academy of Sciences of the United States of America, Vol. 93, No. 4, pp. 1591-1595
113. Sethian, J. A., “Evolution, Implementation, and Application of Level Set and Fast Marching Methods for Advancing Fronts (2001)”, Journal of Computational Physics, Volume 169, Issue 2, pp. 503–555
114. Mukundan, V., Sartori, P, Geyer, V. F., Julicher, F. and Howard, J., “Motor regulation results in distal forces that bend partially disintegrated Chlamydomonas axonemes into circular arcs (2014)”, Biophysical Journal, Vol. 106, Issue 11, pp. 2434-2442
115. Lee, N. K., Kim, S., Kim, H. S., Jeon, T. Y., Kim, G. H., Kim, D. U., Park, D. Y.,Kim, T. U., Kang, D. H., “Spectrum of mucin-producing neoplastic conditions of the abdomen and pelvis: cross-sectional imaging evaluation (2011)”, World Journal of Gastroenterology, Vol. 17, Issue 43, pp.4757-4771
116. Rubin, B. K., “The Role of Mucus in Cough Research (2010)”, Lung, Volume 188, Issue 1, pp 69-72
117. Okuno, M. and Hiramoto, Y., “Direct measurement of the stiffness of Echinoderm sperm flagella (1979)”, Journal of Experimental Biology, Vol. 79, pp. 235-243

118. Deng, Q., Anilkumar, A. V. and Wang, T. G., “The role of viscosity and surface tension in bubble entrapment during drop impact onto a deep liquid pool (2007)”, Journal of Fluid Mechanics, Vol. 578, pp. 119-138
119. Sahin, M., "A preconditioned semi-staggered dilation-free finite volume method for the incompressible Navier-Stokes equations on all hexahedral elements (2005)", International Journal for Numerical Methods in Fluids, Vol. 49, pp. 959-974
120. Jiang B., Lin, T. L. and Povinelli, L. A., "Large-scale computation of incompressible viscous flow by least-squares finite-element method (1994)", Computer Methods in Applied Mechanics and Engineering, Vol. 114, pp. 213-231, Springer
121. Quek, R., Lim, K. M. and Chiam, K.-H., “Three-dimensional simulations of ciliary flow (2013)”, Visualization and Simlation of Complex Flows in Biomedical Engineering, Vol. 12 of the series Lecture Notes in Computational Vision and Biomechanics, pp. 197-218
122. Iftode, F., Cohen, J., Ruiz, F., Rueda, A. T., Chen-Shan, L., Adoutte, A. and Beisson, J., “Development of surface pattern during division in *Paramecium* I. Mapping of duplication and reorganization of cortical cytoskeletal structures in the wild type (1989)”, Development, Vol. 105, pp. 191-211
123. Satir, P. and Christensen, S. T., “Structure and function of mammalian cilia (2008)”, Histochemistry and Cell Biology, Vol. 129, Issue 6, pp. 687-693
124. Narematsu, N., Quek, R., Chiam, K.-H. and Iwadate, Y., “Ciliary metachronal wave propagation on the compliant surface of *Parameciun* cells”, Cytoskeleton, Accepted
125. Gheber, L. and Priel, Z., “Metachronal activity of cultured mucociliary epithelium under normal and stimulated conditions (1994)”, Cell Motility and the Cytoskeleton, Vol. 24, pp. Issue 4, 333-345
126. Yi, W. J., Park, K. S., Rhee, C. S. and Lee, C. H., “Determination of metachronal wave direction and wavelength of beating ciliary cells from correlation map using digitized images (2000)”, Engineering in Medicine and Biology Society, Proceedings of the 22nd Annual International Conference of the IEEE, Vol. 3, pp. 1783-1786

127. Ding, Y., Nawroth, J., McFall-Ngai, M. and Kanso, E., “Mixing and transport by ciliary carpets: a numerical study (2014)”, Journal of Fluid Mechanics, Vol. 743, pp. 124-140
128. Gittes, F., Mickey, B., Nettleton, J. and Howard, J., “Flexural rigidity of microtubules and actin filaments measured from thermal fluctuations in shape (2003)”, Journal of Cell Biology, Vol. 120, No. 4, pp. 932-934
129. Allen, R. D., “Fine structure of membranous and microfibrillar systems in the cortex of Paramecium caudatum (1971)”, The Journal of Cell Biology, Vol. 49, No. 1, pp.1-20
130. Carson, J. L., Collier, A. M., Knowles, M. R., Boucher, R. C. and Rose, J.G., “Morphometric aspects of ciliary distribution and ciliogenesis in human nasal epithelium (1981)”, Proceedings of the National Academy of Sciences, Vol. 78, No. 11, pp. 6996-6999
131. Simet, S. M., Sisson, J. H., Pavlik, J. A., Devasure, J. M., Boyer, C., Liu, X., Kawasaki, S., Sharp, J. G., Rennard, S. I. and Wyatt, T. A., “Long-term cigarette smoke exposure in a mouse model of ciliated epithelial cell function (2010)”, American Journal of Respiratory Cell and Molecular Biology, Vol. 43, No. 7, pp. 635-640
132. Werner, C., Onnebrink, J. G. and Omran, H., “Diagnosis and management of primary cilia dyskinesia (2015)”, Cilia, Vol. 4, doi: 10.1186/s13630-014-0011-8
133. Dillon, R. H., Fauci, L. J., Omoto, C. and Yang, X., “Fluid dynamic models of flagellar and ciliary beating (2007)”, Annals of the New York Academy of Sciences, Vol. 1101, pp. 494-505
134. Craven, T. J., Rees, J. M. and Zimmerman, W. B., “Stabilized finite element modeling of Oldroyd-B viscoelastic flows (2006)”, Proceedings of the COMSOL Users Conference, Birmingham
135. Smith, D. J., “A viscoelastic traction layer model of muco-ciliary transport (2007)”, Bulletin of Mathematical Biology, Vol. 69, Issue 1, pp. 289-327